



University of Kentucky
UKnowledge

Theses and Dissertations--Electrical and
Computer Engineering

Electrical and Computer Engineering


2021

TOWARD INTELLIGENT WELDING BY BUILDING ITS DIGITAL TWIN

Qiyue Wang

University of Kentucky, qiyue.wang@hotmail.com

Author ORCID Identifier:

 <https://orcid.org/0000-0002-2519-7837>

Digital Object Identifier: <https://doi.org/10.13023/etd.2021.033>

[Right click to open a feedback form in a new tab to let us know how this document benefits you.](#)

Recommended Citation

Wang, Qiyue, "TOWARD INTELLIGENT WELDING BY BUILDING ITS DIGITAL TWIN" (2021). *Theses and Dissertations--Electrical and Computer Engineering*. 161.
https://uknowledge.uky.edu/ece_etds/161

This Doctoral Dissertation is brought to you for free and open access by the Electrical and Computer Engineering at UKnowledge. It has been accepted for inclusion in Theses and Dissertations--Electrical and Computer Engineering by an authorized administrator of UKnowledge. For more information, please contact UKnowledge@lsv.uky.edu.

STUDENT AGREEMENT:

I represent that my thesis or dissertation and abstract are my original work. Proper attribution has been given to all outside sources. I understand that I am solely responsible for obtaining any needed copyright permissions. I have obtained needed written permission statement(s) from the owner(s) of each third-party copyrighted matter to be included in my work, allowing electronic distribution (if such use is not permitted by the fair use doctrine) which will be submitted to UKnowledge as Additional File.

I hereby grant to The University of Kentucky and its agents the irrevocable, non-exclusive, and royalty-free license to archive and make accessible my work in whole or in part in all forms of media, now or hereafter known. I agree that the document mentioned above may be made available immediately for worldwide access unless an embargo applies.

I retain all other ownership rights to the copyright of my work. I also retain the right to use in future works (such as articles or books) all or part of my work. I understand that I am free to register the copyright to my work.

REVIEW, APPROVAL AND ACCEPTANCE

The document mentioned above has been reviewed and accepted by the student's advisor, on behalf of the advisory committee, and by the Director of Graduate Studies (DGS), on behalf of the program; we verify that this is the final, approved version of the student's thesis including all changes required by the advisory committee. The undersigned agree to abide by the statements above.

Qiyue Wang, Student

Dr. YuMing Zhang, Major Professor

Dr. Daniel Lau, Director of Graduate Studies

TOWARD INTELLIGENT WELDING BY BUILDING ITS DIGITAL TWIN

DISSERTATION

A dissertation submitted in partial fulfillment of the
requirements for the degree of Doctor of Philosophy in the
College of Engineering
at the University of Kentucky

By

Qiyue Wang

Lexington, Kentucky

Director: Dr. YuMing Zhang, Professor of Electrical and Computer Engineering

Lexington, Kentucky

2020

Copyright © Qiyue Wang 2020
<https://orcid.org/0000-0002-2519-7837>

ABSTRACT OF DISSERTATION

TOWARD INTELLIGENT WELDING BY BUILDING ITS DIGITAL TWIN

To meet the increasing requirements for production on individualization, efficiency and quality, traditional manufacturing processes are evolving to smart manufacturing with the support from the information technology advancements including cyber-physical systems (CPS), Internet of Things (IoT), big industrial data, and artificial intelligence (AI). The pre-requirement for integrating with these advanced information technologies is to digitalize manufacturing processes such that they can be analyzed, controlled, and interacted with other digitalized components. Digital twin is developed as a general framework to do that by building the digital replicas for the physical entities. This work takes welding manufacturing as the case study to accelerate its transition to intelligent welding by building its digital twin and contributes to digital twin in the following two aspects (1) increasing the information analysis and reasoning ability by integrating deep learning; (2) enhancing the human user operative ability to physical welding manufacturing via digital twins by integrating human-robot interaction (HRI).

Firstly, a digital twin of pulsed gas tungsten arc welding (GTAW-P) is developed by integrating deep learning to offer the strong feature extraction and analysis ability. In such a system, the direct information including weld pool images, arc images, welding current and arc voltage is collected by cameras and arc sensors. The undirect information determining the welding quality, i.e., weld joint top-side bead width (TSBW) and back-side bead width (BSBW), is computed by a traditional image processing method and a deep convolutional neural network (CNN) respectively. Based on that, the weld joint geometrical size is controlled to meet the quality requirement in various welding conditions. In the meantime, this developed digital twin is visualized to offer a graphical user interface (GUI) to human users for their effective and intuitive perception to physical welding processes.

Secondly, in order to enhance the human operative ability to the physical welding processes via digital twins, HRI is integrated taking virtual reality (VR) as the interface which could transmit the information bidirectionally i.e., transmitting the human commands to welding robots and visualizing the digital twin to human users. Six welders, skilled and unskilled, tested this system by completing the same welding job but demonstrate different patterns and resulted welding qualities. To differentiate their skill levels (skilled or unskilled) from their demonstrated operations, a data-driven approach,

FFT-PCA-SVM as a combination of fast Fourier transform (FFT), principal component analysis (PCA), and support vector machine (SVM) is developed and demonstrates the 94.44% classification accuracy. The robots can also work as an assistant to help the human welders to complete the welding tasks by recognizing and executing the intended welding operations. This is done by a developed human intention recognition algorithm based on hidden Markov model (HMM) and the welding experiments show that developed robot-assisted welding can help to improve welding quality. To further take the advantages of the robots i.e., movement accuracy and stability, the role of the robot upgrades to be a collaborator from an assistant to complete a subtask independently i.e., torch weaving and automatic seam tracking in weaving GTAW. The other subtask i.e., welding torch moving along the weld seam is completed by the human users who can adjust the travel speed to control the heat input and ensure the good welding quality. By doing that, the advantages of humans (intelligence) and robots (accuracy and stability) are combined together under this human-robot collaboration framework.

The developed digital twin for welding manufacturing helps to promote the next-generation intelligent welding and can be applied in other similar manufacturing processes easily after small modifications including painting, spraying and additive manufacturing.

KEYWORDS: Smart Manufacturing, Digital Twin, Machine/deep Learning, Human-robot Interaction, Virtual Reality, Welding

Qiyue Wang

11/18/2020

Date

TOWARD INTELLIGENT WELDING BY BUILDING ITS DIGITAL TWIN

By
Qiyue Wang

Dr. YuMing Zhang

Director of Dissertation

Dr. Daniel Lau

Director of Graduate Studies

11/18/2020

Date

ACKNOWLEDGMENTS

The following dissertation, while an individual work, benefited from the insights and direction of several people. Firstly, I thank my advisor Dr. YuMing Zhang sincerely, for his invaluable guidance, encouragement, and constructive suggestions. In addition, I am grateful to other committee members and faculties including Dr. Michael T. Johnson, Dr. Kevin Donohue, Dr. Qiang Ye, Dr. Fazleena Badurdeen, and Dr. Peng Wang for their timely and instructive support for my research. In the meantime, I would like to give my thanks to all my colleagues in the Welding Research Lab: Dr. Chao Li, Dr. Wenhua Jiao, Dr. Shaojie Wu, Mr. Rui Yu, Mr. Yongchao Cheng and Mr. Joseph Kershaw for their helps and suggestions for my work.

In addition to the technical and instrumental assistance above, I received equally important assistance from family and friends. My girlfriend, Dandan Ren, provided on-going support throughout the dissertation process.

TABLE OF CONTENTS

ACKNOWLEDGMENTS	iii
TABLE OF CONTENTS.....	iv
LIST OF TABLES.....	vii
LIST OF FIGURES	viii
CHAPTER 1. INTRODUCTION	1
1.1 Background.....	1
1.2 Objectives and Outline.....	2
CHAPTER 2. LITERATURE REVIEW	4
2.1 Digital Twin.....	4
2.2 Intelligent Welding	6
2.3 Deep Learning.....	10
2.3.1 Convolution Neural Networks	11
2.3.2 Recurrent Neural Networks	14
2.4 Human-robot Interaction.....	15
CHAPTER 3. DEEP LEARNING-ENPOWERED DIGITAL TWINS.....	19
3.1 Introduction.....	19
3.2 System Configuration and Principles.....	19
3.3 Information Processing	23
3.3.1 TSBW Computation.....	23
3.3.2 BSBW Estimation.....	26
3.3.2.1 Data Collection and Pre-processing.....	26
3.3.2.2 Model Training and Validating.....	29
3.4 Welding Quality Control.....	35
3.5 Visualization in Digital Twin.....	38
3.6 Summary	41
CHAPTER 4. DIGITAL TWIN FOR HUMAN-ROBOT INTERACTIVE WELDING. 43	
4.1 Introduction.....	43
4.2 System Configuration	44

4.3 Working Principles	46
4.4 Summary	51
CHAPTER 5. WELDER BEHAVIOR ANALYSIS	52
5.1 Introduction.....	52
5.2 Principles.....	52
5.3 Experimental Verification.....	57
5.4 Results and Discussions.....	60
5.5 Summary	64
CHAPTER 6. ROBOT-ASSISTED WELDING	65
6.1 Introduction.....	65
6.2 Principles of HMMs.....	66
6.3 Model Identification.....	67
6.3.1 Principles of Baum-Welch Algorithm	67
6.3.2 Data Collection	70
6.3.3 Identification of Hidden State Number.....	71
6.3.4 Model Training	73
6.4 Human Intention Recognition.....	73
6.4.1 Principles.....	73
6.4.2 Testing Verification	74
6.5 Robot-Assisted Welding Experiment	77
6.6 Summary	81
CHAPTER 7. HUMAN-ROBOT COLLABORATIVE WELDING	82
7.1 Introduction.....	82
7.2 Principles.....	83
7.2.1 Cyber-Physical Model	83
7.2.2 Manual Speed Adjustment.....	84
7.2.3 Robotic Weaving and Seam tracking.....	85
7.3 Welding Experiments and Analysis.....	89
7.3.1 Manual Welding.....	89
7.3.2 Robotic Welding	91
7.3.3 Human-robot Collaborative Welding	92
7.3.4 Result Analysis	93
7.4 Summary	94

CHAPTER 8. CONCLUSIONS AND FUTURE WORKS.....	96
8.1 Conclusions.....	96
8.2 Future Works	97
BIBLIOGRAPHY	99
VITA.....	108

LIST OF TABLES

Table 3.1	Applied Welding Parameters and Camera parameters	22
Table 3.2	The MSE in Validation Dataset and Testing Dataset from Different Input Source	33
Table 3.3	BSBW Prediction Performance Comparation	34
Table 5.1	Welding and Workpieces Parameters	58
Table 5.2	5-Folder Cross Validation Performance with Different Kernels	62
Table 5.3	Testing Confusion Matrix.....	63
Table 6.1	Welding Parameters Applied	70
Table 6.2	Statistical Information for Testing Experiments.....	75
Table 7.1	Welding and Camera Parameters Applied.....	82
Table 7.2	Fitting Result of $U = U(L, I)$	87

LIST OF FIGURES

Figure 2.1 Principles of Welding Processes.	8
Figure 2.2 Architecture and principles of LeNet-5 [56].	11
Figure 2.3 Architecture and principles of a RNN [68].	15
Figure 3.1 System Configuration and Principles (a) Working Principles; (b) Configuration.	21
Figure 3.2 The Overall Technical Roadmap.	21
Figure 3.3 Vision Sensing in P-GTAW (a) Image Captured in Base Current Phase; (b) Pulsed Welding Current; (c) Image Captured in Peak Current Phase.	23
Figure 3.4 Principles for Computing w_t From the Weld Pool Image. (a)-(g) Image Preprocessing for Weld Pool Localization; (g)-(k): Identifying Boundary Candidates; (l)-(n) Weld Pool Boundary Identification Using Watershed; (o)-(p): w_t Computation.	24
Figure 3.5 Automatic Data Collection and Labeling. (a) System Configuration; (b) Captured Back-side Image; (c) Region of Interest (ROI) Selection; (d) Image Binarization with 80 as Threshold; (e) Computing Back-side Area a_b in Pixel; (f) Mapping Model Between BSBW w_b and the Back-side Area a_b	27
Figure 3.6 Dataset for Deep Learning Model Development (a) Construction; (b) Training Dataset Distribution; (c) Validating Dataset Distribution; (d) Testing Dataset Distribution.	29
Figure 3.7 Architecture of Developed CNN for BSBW Estimation.	30
Figure 3.8 CNN Model Training and Validating from Different Information Source. ...	33
Figure 3.9 BSBW Growth Prediction from Trained CNN and Composite Images in Different Welding Conditions.	35
Figure 3.10 Controlled Weld Joint in Various Welding Conditions Based on CNN.	38
Figure 3.11 GUI for Digital Twin Visualization (I) Weld Joint Dynamic Evolution; (II) Weld Joint Geometry; (III) Weld Images; (IV) Arc Information.	39
Figure 3.12 Weld Joint Cross Section Contour Modeled as an Ellipse (a) Principles; (b) Ellipse Parameter k Identification.	40
Figure 4.1 Developed Digital Twin for HRI in Welding Manufacturing (a) Schematic Diagram (b) Real Diagram.	45
Figure 4.2 The Human User Demonstrates the Welding Operations Via a Composite Torch Which is Composed of a Manual Torch and a Motion-tracking Handle.	46
Figure 4.3 System Working Principles. Physical HRI Covers Human Space, Robot Space and Welding Space and Its Digital Twin Exists in Digital Space.	47
Figure 4.4 The Human User Controls the Welding Current by Sliding the Thumb Position on Touchpad.	48
Figure 5.1 The Overflow of Proposed Welding Skill Level Classification Model from Demonstrated Operation Data.	53
Figure 5.2 The Principles of SVM.	56

Figure 5.3 The Welded Workpieces from the Welders with Different Professional Levels. (a) and (b) Are the Front and Back Side from Skilled Welders and the Quality Is Satisfied; (c) and (d) Are the Front and Back Side from Unskilled Ones and the Quality is Unsatisfied.	58
Figure 5.4 Facing the Same Welding Task, the Human Users with Different Professional Levels Demonstrate Different Welding Operations. X is the Welding Direction; Y is the Lateral Direction and Z is Vertical Direction; (a) from a Skilled Welder; (b) from an Unskilled Welder.	59
Figure 5.5 The Demonstrated Speed Sequences Computed from Position Sequences (a) from a Skilled Welder; (b) from an Unskilled Welder.	60
Figure 5.6 The Histogram of the Computed Criterion $(W \cdot \Phi(F^R) + b)$ for Classification in 5-folder Cross Validation. (a) Liner; (b) Poly-2; (c) Poly-3; (4) Poly-4; (5) Rbf; (6) Tanh.	62
Figure 5.7 The Histogram of the Computed Criterion $(W \cdot \Phi(F^R) + b)$ for Classification in Testing Data.	63
Figure 6.1 Schematic Diagram for HMM.	67
Figure 6.2 Model Evaluation with Different Number of States.	72
Figure 6.3 Convergence in Model Training.	73
Figure 6.4 Human Intention Recognition Result (a) x-direction Which the Welding Torch Moves Along; (b) y-direction Where Welding Torch Deviates from Weld Seam; (c) z-direction Which is Vertical.	76
Figure 6.5 Robot Trajectory (a) x-direction; (b) y-direction; (c) z-direction.	78
Figure 6.6 Welded Workpieces (a) Front Side without Human Intention Recognition; (b) Back Side without Human Intention Recognition; (c) Front Side with Human Intention Recognition; (d) Back Side with Human Intention Recognition.	79
Figure 6.7 Schematic Diagram of Arc Shape with the Vertical Movement of Welding Torch. Red Dash: Original Shape. Black Solid: Arc Diverges with Arc Lengthening. ...	80
Figure 6.8 Principle of Robot-assisted Manual Welding (a) Without Human Intention Recognition; (2) With Human Intention Recognition.	80
Figure 7.1 Geometrical Cross Profile of Welded Workpiece.	83
Figure 7.2 Cyber-physical Model of Virtual Reality Human-robot Collaborative Welding. A Local Close-loop Circuit Is Built for Automatic Weaving and Seam Tracking.	84
Figure 7.3 A typical Working Scene Shown to Human by HMD.	85
Figure 7.4 Arc Length Determines Arc Voltage Linearly.	86
Figure 7.5 Welding Current Determines Arc Voltage Linearly.	87
Figure 7.6 Fitting Curve of $U = U(L, I)$	87
Figure 7.7 Swing Center Deviation from Weld Seam Results in Asymmetric Arc Length Distribution.	88
Figure 7.8 Working Flowchart of Proposed Automatic Seam Tracking Algorithm.	89
Figure 7.9 Swing Trajectory of Manual Welding.	90
Figure 7.10 Manual Travel Speed Adjustment Facing Variable Welding Current.	90
Figure 7.11 Welded Workpiece from Manual Welding.	91

Figure 7.12 Welding Torch Travel Direction Deviates the Weld Seam with Degree θ .	91
Figure 7.13 Welding Torch Weaving Trajectory with Automatic Seam Tracking.	91
Figure 7.14 Welded Workpiece from Robotic Weaving Welding with Automatic Seam Tracking.	92
Figure 7.15 Robotic Weaving Trajectory in Human-robot Collaborative Welding.	92
Figure 7.16 Travel Speed Applied from Human in Human-robot Collaborative Welding.	93
Figure 7.17 Welded Workpiece from Human-robot Collaborative Welding.	93
Figure 7.18 Solid Red Line Draws the Outline of Weld Bead (a) from Manual Welding (b) from Human-robot Collaborative Welding.	94

CHAPTER 1. INTRODUCTION

1.1 Background

Manufacturing, as the executive stage from the raw materials to applicable products, is the foundation of the economy. With the increasing demands for manufacturing on efficiency, quality, individualization, and flexibility, many countries have issued strategic plans to accelerate the rapid transition from current mechanized/automatic manufacturing to the next-generation smart manufacturing [1], such as the Industry 4.0 in Germany, Advanced Manufacturing Partnership in America, and Made in China 2025 in China. Though “smart manufacturing” has not been rigorously and consistently defined, its core ideas have been accepted widely as monitoring, controlling, integrating and optimizing the manufacturing processes with the support from the information technology advancements including cyber-physical systems (CPS) [2], Internet of Things (IoT) [3], big industrial data [4], and artificial intelligence (AI) [5]. The pre-requirement for integrating these advanced information technologies is to digitalize manufacturing processes themselves such that they can be analyzed, controlled, and interacted with other digitalized components. Digital twin is developed as a general framework to do that [6]. In physical manufacturing systems, the raw materials are processed in a designed sequence by machines, conveyors, robots, and humans to be the final products. If the data characterizing the system running status can be collected from the sensors, a digital replica can be built in the digital/virtual world. This digital replica owns not only the same physical elements but also the same dynamics and running status as the physical entity. By receiving the running information streams from the physical

entity, its digital replica can update itself like its twin and that is where its name is derived [7].

Welding, as one of the most important material joining methods, has been playing a critical role in industrial manufacturing including automotive, shipbuilding, electronics etc. Humans, robots and hard automation are the three main performers in practical welding processes [8]. In the traditional manual welding, the skilled welders are able to adaptively adjust welding parameters to ensure the product quality according to the perceived process information even when the unpredicted disturbance happens. Therefore, the manual welding is preferable for the high-quality and precise welding tasks. However, it is urgent to accelerate the transition from manual welding to intelligent robotic/automatic welding due to the following several reasons: (1) a great human welder shortage is faced globally [9]; (2) the health of human welders are harmed due to being exposed to the toxic fumes and gases in welding environment [10]; and (3) the productivity of the human welders cannot meet the ever-increasing demand for manufacturing efficiency. Accelerating the development of intelligent robotic/automatic welding is a promising solution to address this problem. One challenge to realize robotic/automatic welding is the time-varying working environment in practical welding applications. Therefore, it is necessary to monitor, model and control the welding processes to minimize the negative effect from unpredicted welding environment and digital twin is a perfect tool toward intelligent welding to digitalize the welding processes.

1.2 Objectives and Outline

This work aims to promote traditional welding toward intelligent welding by building its digital twin and contributes to digital twin in the following two aspects (1)

increasing the information analysis and reasoning ability by integrating deep learning; (2) enhancing the human user operative ability to physical welding manufacturing by integrating human-robot interaction (HRI).

In this dissertation, the intelligent welding systems are developed based on digital twin and the dissertation is organized as follows. The related literature is reviewed in Chapter 2 involved the state-of-art of digital twin, intelligent welding, deep learning, and human-robot interaction. A digital twin for visualized welding monitoring and control is developed in Chapter 3 by integrating deep learning to increase the analysis and reasoning ability. A digital twin for human-robot interactive welding system is developed in Chapter 4 to enhance then operative ability of the human users. Chapter 5 develops a data-driven method for welding skill classification from demonstrated welding operations. Chapter 6 develops a robot-assisted welding method based on human intention recognition and Chapter 7 demonstrates human-robot collaborative welding. The Chapter 8 draws the conclusions and presents the future works.

CHAPTER 2. LITERATURE REVIEW

This work is related with following four academic fields i.e., digital twin, intelligent welding, deep learning and human-robot interaction and their corresponding literature reviews are following.

2.1 Digital Twin

Digital twin aims to build the digital replicas of the physical systems in the digital/virtual space. Such a digital replica simulates not only the same elements (as contained in a physical system) but also the same dynamics (equipment running) such that it can run as the physical counterpart does in real time like a twin. As such, its building cost is much lower in time and finance especially during the product design stage and prototyping stage where lots of modifications need to be done. Therefore, the digital twin is a perfect platform to conduct the optimization and validation experiments. As such, the large-volume heuristic experiments need to be done previously can be avoided with development time and cost reduced greatly. In industry, assembling aims to integrate the separated parts together and is needed in almost all product fabrication. Some studies have been done to optimize the assembling path [11], sequence [12], needed force [13] and task distribution in human–robot collaboration [14] in digital twin environments such that the part deformation is minimized and production efficiency is increased. The similar optimizations based on digital twins have also been done for supply chain to reduce resource utilization [15] and production cost [16]. In additive manufacturing, DebRoy et al. developed the numerical simulation-based digital twins to study the temperature, metal flow, solidified microstructure and deposit geometry evolution [17]–[19]. Including the

specific manufacturing processes, digital twin is also used in production-line level and factory level for their design and optimization. In the designing stage of production-lines or factories, digital twins are built firstly to simulate their running states without installing the high-value, large-size and complex equipment physically. Furthermore, it is much easier to improve continuously due to the flexible and highly modular components in digital twins. Some general blocks in manufacturing including raw material supply, job scheduling, equipment maintenance and product transportation have been digitalized and used in the manufacturing of electronic devices [20], hollow glass [21] and 5G mobile edge computing [22] for their architecture optimization. To respond to the unpredicted disturbance in practical cases, the digital twin is also used as a virtual experiment platform for control algorithm development and verification [23] [24] or a final verification platform before the remedial actions takes into effect in physical systems [25]. In such applications, the physical systems are protected by their digital twins as an additional shield, such that the robustness is increased, and shut-down risk is reduced.

To build a digital twin, the information about the corresponding physical system is collected from installed sensors, which makes it possible to extract/analyze the information of interest to monitor the physical systems in real time. Since all the information has been digitalized in digital twins in preferable formats for storage, communication, and processing, the digital twin-based monitoring methods have following favorable characteristics: (1) high availability regarding large-volume data, especially with the enhancement from cloud storage technology; (2) easy fault detection without personal check; (3) high scalability and customizability because of its modularization; and (4) low complexity for performing multi-tasks. As such, the percentage of digital twin-driven

monitoring systems is increasing in various manufacturing processes. In computer numerical control (CNC) machine tooling systems, the time-variant dynamics due to part wear and aging will harm the machining accuracy which need to be monitored in real time. Erkorkmaz et al. developed a digital twin to monitor the force, torque and motion for multi-axis machine tools to identify the system dynamics and update the control strategy in real time to decrease the machining errors [26]. The collected information can be also processed/analyzed further to offer the machine health assessment [27] and predictive maintenance plans [28]. In additive manufacturing, the motion of 3D printer nozzle determines the formation of printed material thus is monitored in its digital twin to obtain the satisfied printed workpiece geometry [29]. In addition, the environment information including the temperature, humidity and smoke etc. is also monitored to offer an ideal working environment [30]. Fault diagnosis is another important aspect for digital twins in process monitoring. In photovoltaic systems, the solar irradiance and temperature are monitored as the indicator of panes and converters running status [31]. The experiments show that the digital twin-based monitoring methods own higher sensitivity and lower detecting time compared with traditional ones. In personal healthcare field, the digital twins are built by collecting the human physiological parameters via the smart wearable sensors to characterize their physical health status. After the digital twins are shared with the medical organizations, the humans can receive faster and more accurate medical instructions and services [32] which help to reduce the risk of illness greatly.

2.2 Intelligent Welding

The principles of an arc welding process are shown in Figure 2.1. An electrical arc is ignited between the welding torch and the workpieces as the heat source to melt the base

metal forming the weld pool. The fill metal could be added for mechanical and metallurgical enhancement depending on the application cases. After the weld pool solidifies, the weld bead forms such that the separated workpieces previously are jointed together. Depending on the size of the weld pool, the quality of solidified weld joints evolves experiencing three stages, (I) incomplete fusion; (II) good; and (III) burn through. In the stage I, top-side bead width (TSBW) w_t is not large enough and the weld pool depth d is smaller than the workpiece thickness T . This results to the incomplete fusion in the back side which will harm joint mechanical properties. With the heat input increasing, the weld pool grows with joint quality improved. When its back-side bead width (BSBW) w_b reaches a specific width w_0 which is dependent on T , the joint quality is optimal, as shown in stage II. With the heat increasing further, weld pool is too large to be supported by surface tension. The workpieces are burn through leaving holes under the arc as shown in stage III which is a welding failure and cannot be accepted. Therefore, it is necessary to monitor BSBW in real time and control it to be minimum to decrease the burn through risk with a pre-requirement that $w_b \geq w_0$. However, it is usually difficult to install back-side sensors to collect the back-side information directly due to the limited physical accessibility. Under this restriction and consideration, some indirect sensing approaches have been developed to monitor the weld pool through sensors in top side and then estimate the back-side weld width from the sensed data.

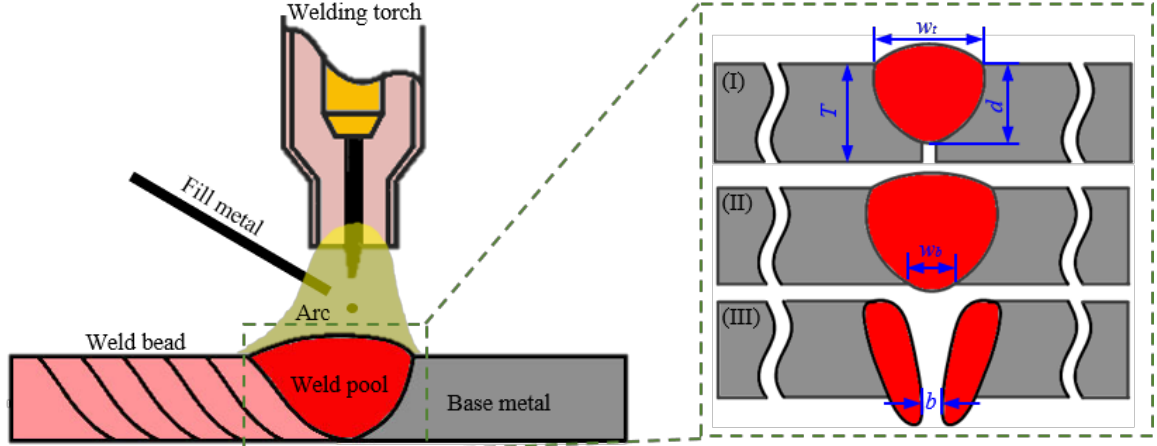


Figure 2.1 Principles of Welding Processes.

As discussed before, welding is a heat-induced metal fabrication process where the temperature plays a critical role in metal melting and solidifying. Some studies have proposed to monitor the temperature distribution of weld pool through infrared sensors for process analysis [33][34], defect detection [35] and process control [36].

The weld penetration status is dependent on the geometrical profile of the weld pool. Therefore, some researchers proposed to sense the weld pool geometry and use it to predict the weld penetration status including ultrasonic sensing [37] [38] and vision sensing [39] [40]. Beyond identifying weld penetration from current weld pool geometry, some studies proposed to identify the penetration state from the sequence of weld pool surface geometry variation i.e., weld pool oscillation. The weld pool surface oscillation due to the force from heat source can be sensed via arc voltage fluctuation [41] and weld pool video [42].

Given available sensor data, proper data pre-processing and analysis are needed to gain the target information of interest. For a series of infrared images over a certain time period, the cooling curve can be extracted, from which welding defects can be identified [35][43]. Because of the difference in thermodynamics between defective welding (such

as large porosity, incomplete fusion) and good welding, their cooling rates are different and can be regarded as a characteristic feature for defect detecting. Through appropriate clustering algorithms, the defective weld workpieces and good ones can be clearly classified. The infrared sensing has also been used as an approach for prediction of welding penetration. In these applications, some features have been defined and extracted from the infrared images, such as the weld pool width and length, peak temperature, mean value and variance of the temperature, weld pool area under certain temperature, etc. from the reconstructed temperature distribution field [44][45]. Then, some non-linear models through data-driven techniques, such as neural networks and adaptive neuro fuzzy inference system (ANFIS), are established to correlate extracted features to penetration states.

Geometry sensing data is processed and analyzed in a similar way. From the captured images, the two dimension (2D) information about the weld pool surface is defined by quantifying its length, width, area, rear angle etc. [46][47], which are obtained through some image processing methods such as noise reduction, edge detection, curve fitting etc. Then, the relationship between penetration status and the 2D information are identified through data-driven regression techniques. Upon the basis of 2D sensing, three dimension (3D) sensing that provides additional information about weld pool convexity, complements the available information from 2D sensing and can improve the prediction accuracy of penetration status [40][48]. Ultrasonic-based geometry sensing used another idea, i.e., measuring the time of flight (TOF) of the ultrasonic wave from the generator to the receiver. As the TOF directly depends on the depth of weld pool under workpieces, the weld penetration status can be identified by differentiating the TOF. [37][38]. If the

geometry sensing data are concatenated as temporal sequential data, some information specific to sequential data (e.g., reflect weld pool surface fluctuation) can be extracted. In weld pool surface fluctuation sensing, the fluctuation frequency (also called weld pool oscillation frequency) is found to be related to the weld pool dimensions and penetration state which can be extracted by Fourier transform easily [41][49]. After this, control algorithms are developed and applied to make sure that the weld joints are in full penetration status which is a critical factor determining the mechanical properties of weld joints such as strength, anti-corrosion ability and service life.

2.3 Deep Learning

Deep learning is developed upon conventional shallow neural network, with the biggest difference in the number of hidden layers. Hidden layers project the input data to multiple dimensional spaces, where input data can be analyzed from a different angle. The more hidden layers, the more likelihood patterns underlying the data can be discovered. However, adding more layers also introduces some issues to the network training and performance: (1) the vanishing gradient problem that refers to the network prediction error cannot be well received by the first few network layers becomes more severe; (2) the overfitting risk increases greatly with the complexity of network architecture, as more parameters in the network needs to be trained; (3) the computation power needed increase with the amount of network complexity and volume of training data. Fortunately, these problems are addressed somehow in the recent development of deep learning, which is featured by: (1) new network structures developed to better keep the memory throughout the information flow in the network, with representative structure including ResNet [50]; (2) robust network training using large-scale dataset together with new activation

functions, to reduce the overfitting problem; and (3) high-performance computation resources, such as GPU [51]. As a result, deep learning has become the state-of-the-art method in computer vision (CV) [52], audio processing [53] and natural language processing (NLP) [54]. In deep learning, convolutional neural networks (CNNs) and recurrent neural networks (RNNs) are two representative models for processing grid-shape data and sequential data. Therefore, they are briefly introduced in following parts.

2.3.1 Convolution Neural Networks

The first CNN was proposed by Fukushima in 1980 and inspired from animal visual cortexes architectures for visual perception [55]. LeCun et al. completed the first modern CNN, LeNet-5 in 1998 and applied it successfully for handwritten digit recognition [56]. Then, some breakthrough works have been achieved, including AlexNet [57], VGGNet [58], GoogLeNet [59], GAN [60] and ResNet [50] which have been the benchmarks for computer vision studies. The fundamental network architecture and principles are shown in Figure 2.2, taking LeNet-5 as an example. The other architectures are quite similar to this but contains more numbers of hidden layers and a few new elements (such as normalization, by-pass flow, activation) to gain the better capabilities for feature extraction and reasoning.

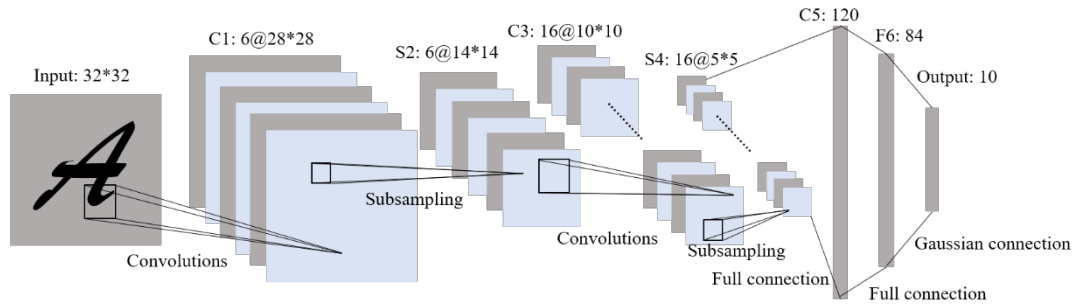


Figure 2.2 Architecture and principles of LeNet-5 [56].

As shown in Figure 2.2, CNNs are consisted with three types of layers: convolutional layers, pooling layers and fully connected layers. Taking the images or any grid-like data as the input, the convolution operations are applied to extract feature maps through convolving the feature maps at the previous layer with shifting small-size kernels:

$$C(k, i, j) = \sum_{l=0}^{L-1} \sum_{m=0}^{M-1} \sum_{n=0}^{N-1} I(l, i + m, j + n) \times K_k(l, m, n) + b_k \quad (1)$$

where C denotes the extracted feature maps, I is the feature map at the previous layer, K_k is the k th kernel applied, b_k is the bias, (L, M, N) is the size of the kernel. M and N are usually rather small ($M, N < 10$) and L is the third-dimension size of the previous layer (representing the number of feature maps). In lower-level convolutional layers, these convolution operations are similar as some basic image processing operations (such as edge detection, image blurring etc.). The difference is that the kernels applied, which are fixed/designed artificially in traditional image processing but are learnable and trained from training data in CNNs. With the convolutional layers going deeper, the features are more and more abstract and related to the final target. Then, a non-linear activation function is applied to endow nonlinearity to the network:

$$O(k, i, j) = a(C(k, i, j)) \quad (2)$$

where O is the activation output and a is the activation function. Common activation functions include ReLU, Sigmoid, Tanh, Tanhshrink etc. Pooling layers are added to reduce the data dimension and assure the local invariance:

$$O(k, i, j) = \text{pooling}(C(k, m, n)), \forall (m, n) \in R_{ij} \quad (3)$$

where R_{ij} is the local neighborhood around location (i, j) . The common pooling functions are max pooling, average pooling, etc. The existence of pooling layers greatly decreases the number of training parameters and corresponding computational volume, while

increases the robustness of the algorithms it reduces the effect of local information (or disturbance) on final decision making.

Upon the features extracted from convolutional and pooling layers, the fully connected layers serve the reasoning ability to relate the features to the targets of interest. The outputs of the fully connected layers are calculated by a matrix product:

$$O_{i+1} = W_i \cdot O_i + b_i \quad (4)$$

where O_i is the i th fully connected layer, W_i is the weight matrix and b_i is the bias. These convolutional layers, pooling layers and fully connected layers are connected in a sequence designed by users. Given a certain network structure and inputs, the targets (classification labels or regression values) can be predicted through forward propagation. In order to achieve an accurate prediction performance, the unknown parameters including kernels, weights, and biases denoted as θ in CNNs models need to be trained by minimizing the average loss:

$$\theta_{optimal} = \operatorname{argmin}(L) \quad (5)$$

where L is the average loss:

$$L = \frac{1}{N} \sum_{i=0}^{N-1} l(y^{(i)}, o^{(i)}) \quad (6)$$

where $y^{(i)}$ is the true target label/value, $o^{(i)}$ is predicted label/value, N is the training data size, and l is the loss functions (squared error, Hinge loss, cross-entropy etc.) that vary with the applications from instant to instant. Usually, the Eq. (5) do not have the explicit solution and parameters are identified by iterative gradient-descent method called back-propagation:

$$\theta_{n+1} = \theta_n - lr_n \cdot \nabla_{\theta} L \quad (7)$$

where lr is the learning rate. Some variant optimizers have also been developed to accelerate the training processing such as Adagrad [61], Adadelata [62], and Adam [63]. In the practical applications, the memory required increases linearly with the sample number. Therefore, only a portion of data is used for one iteration which is called minibatch optimization and the size of the data portion for gradient computation M is called minibatch size:

$$\begin{aligned}
\theta_{n+1}^1 &= \theta_n - lr_n^1 \cdot \nabla_{\theta} \left(\frac{1}{M} \sum_{i=0}^{M-1} (\hat{w}_b^i - w_b^i)^2 \right) \\
\theta_{n+1}^2 &= \theta_{n+1}^1 - lr_n^2 \cdot \nabla_{\theta} \left(\frac{1}{M} \sum_{i=M}^{2M-1} (\hat{w}_b^i - w_b^i)^2 \right) \\
&\vdots \\
\theta_{n+1}^{N/M} &= \theta_{n+1}^{N/M-1} - lr_n^{N/M} \cdot \nabla_{\theta} \left(\frac{1}{M} \sum_{i=N-M}^{N-1} (\hat{w}_b^i - w_b^i)^2 \right)
\end{aligned} \tag{8}$$

2.3.2 Recurrent Neural Networks

RNNs are proposed in 1980s [64] to process and analyze sequential data $[I_1, I_2, \dots, I_t]$. Then, some variants have been developed with more complex architectures, such as bidirectional associative memory (BAM) [65], echo state networks (ESNs) [66], Long short-term memory (LSTM) [67] etc. Now, the RNNs have been the state-of-the-art models for audio processing and text processing [53][54].

The general architecture and principles of RNNs are shown in Figure 2.3. Compared with other neural networks, the biggest significance is the explicit connection of the hidden states:

$$H_i = a(W_{IH} \cdot I_i + W_{HH} \cdot H_{i-1} + b_i) \tag{9}$$

where H is hidden state, I is the input, W is the weight matrix, b is bias and a the non-linear activation function. The current state H_t is not only dependent on the current input, but also the previous inputs $[I_1, I_2, \dots, I_{t-1}]$ indirectly via the previous state H_{t-1} , following a

Markovian chain. This approach reduced the computation greatly since all previous information are abstracted as one state propagates forward without missing key information.

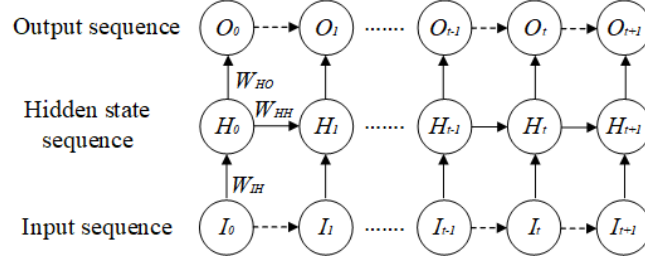


Figure 2.3 Architecture and principles of a RNN [68].

By connecting the hidden state, the previous input can also take effect on current output prediction such that the sequential reasoning can be identified. In training RNNs, the backpropagation is also applied in learning hidden state connection parameters (W_{HH} in Figure 2.3), which is called back-propagation through time (BPTT).

2.4 Human-robot Interaction

According to the International Federation of Robotics (IFR), over 50% of industrial robots are used for welding operations in the US and globally, including spot welding, arc welding, and laser welding [69][70]. However, due to the difficulty of developing artificial intelligence (AI) based controls, currently most welding robots are pre-programmed through on-line teaching, off-line programming or a combination of the two [71]. That is also why welding robots can be only applied to repeated welding tasks in a production line with strict requirements regarding a consistent working environment.

In comparison, welding technicians especially the skilled ones can perform well in spite of working disturbance by adjusting welding torch movement adaptively after

perceiving, analyzing and integrating information from welding processes [72]. This is the reason why the skilled technicians are usually the performers for some critical welding applications. Moreover, welding technicians have higher flexibility therefore are preferred in small-volume and unstructured welding applications considering the cost both in time and finance. However, welding technicians are exposed to hazardous fume, gas and arc radiation when undertaking welding tasks on site [73]. They also have worse performance in accurate, repeated, and long-time control of welding torch movement than welding robots. In addition, an urgent combat of welder shortage, especially for qualified ones is faced by the whole world according to American welding society (AWS) [9]. From the analysis above, it can be found that both human and robots have their own advantages and disadvantages, and human-robot interaction (HRI) is a possible solution to do that.

By taking advantage of the skills of welding technicians, three-level of applications have been proposed: (1) telerobotic welding [74][75]: in which robots who have fewer physical limitations (temperature, pressure, vacuum, radiation) are used remotely as physical extensions of the human welders. This extends the human welders' working activity space significantly, such that unstructured welding tasks can be easily done in extreme environments (space, ocean, nuclear environment). (2) manual welding with robots assisting [72][76]: human welders act together in the same welding process. With robotic assistance, tedious and strenuous manipulations for humans are lessened and sudden and abrupt motions which should be avoided in the welding process can be suppressed. This approach takes advantage of both human (high intelligence) and robots (high stability) to increase production efficiency and effectiveness. (3) welding robots demonstration-based imitation learning [77][78]: in this approach, human welders work as

masters to demonstrate their skills to robots as their apprentices. By recording state-action pairs, control policy characterizing human skills can be developed for the welding robots. After robots learn from human welders' demonstration, they can finish welding tasks independently. For all three above applications, information communication between human welders and robots plays a critical role. Many interfaces such as joysticks [79], haptic gloves [80], gestures [81], and speech [82] have been proposed to transfer manipulation information from humans to robots. Onsite information (usually as visual information) are shown to the operators directly or via video stream in 2D or 3D display [83][84]. With the recent rapid development of computer graphics, some customer-grade VR systems have been commercialized successfully such as Oculus Rift, HTC Vive, and PlayStation VR. By offering immersive and interactive ability, VR has been applied in prototyping designing and skill training [85][86][87][88]. Compared with traditional computer aided design (CAD) methods, VR offers the immersive visualization and flexible evaluation for each designing component in product prototyping stage and have been applied in the field of airplane [89], automotive [90] assembly tools [91] and house building [92][93]. Skill training is another application of VR in industry to increase operation safety and reduce financial cost. Some VR-based training system have been developed in some common manufacture processes including welding [94][95], painting [96] and mining [97]. In these training systems, a virtual environment is generated where the trainees can take actions and receive feedback about their operations. By interacting with virtual environments, the trainees learn the skills needed for real manufacture processes. Offering an intuitive and natural manipulation style is another advantage of VR system which is preferred to work as an interface between human and robots [98][99]. In

such VR-based HRI systems, humans teleoperate the robots via the control handles and receive the onsite scenes from the head-mount display (HMD) as the visual feedback. By doing that, VR benefits HRI greatly.

CHAPTER 3. DEEP LEARNING-ENPOWERED DIGITAL TWINS

3.1 Introduction

As talked before, BSBW plays a very import role determining welding quality but it is difficult to be monitored by installing back-side sensors directly due to the limited physical accessibility. Therefore, we need the ability to estimate BSBW indirectly from the available information collected by top-side sensors.

Some studies been done for BSBW estimation by analyzing various information including reflected laser patterns by weld pool [48], temperature distribution [44], arc sound [100], weld pool images [101], arc voltage [102] and the fusion of above [103]. In these research works, features are defined and extracted firstly from the collected raw data. Then, a traditional machine learning model is developed between the extracted features and BSBW. This method is labor-intensive in artificial feature extraction and the prediction performance is highly dependent on personal experience. Furthermore, some other key features may be missed due to the limited personal perception. To solve this problem, we propose to apply convolutional neural networks (CNNs) to extract the features from the sensed weld images automatically and conduct the deep reasoning to predict BSBW. Based on the accurate prediction of BSBW, we can monitor and control the joint growth and weld quality in the developed digital twin better.

3.2 System Configuration and Principles

The system configuration and its working principles are shown in Figure 3.1 which is composed of the physical welding module and digital twin module and the overall technical roadmap is shown in Figure 3.2. In the physical welding module, an automatic welding platform is built by a motor-driven conveyor for workpiece movement and a

Miller Maxstar 210 welder for power supply which are both controlled by a computer. In detail, the conveyor is controlled by moving time t and moving speed v and the welding current is controlled to be pulsed to conduct pulsed gas tungsten arc welding (GTAW-P). Other welding parameters applied are shown in Table 3.1. In order to monitor the welding running status, two kinds of sensors are applied, i.e., the arc sensors for monitoring real arc voltage U and welding current I and the industrial camera (Point Grey FL3FW03S1C) for capturing weld images whose configuration parameters are shown in Table 3.1. During the imaging process, a bandpass optical filter centered at 685 nm is installed on the camera to decrease the negative effect from the intensive arc radiation. The image capturing frequency matches the welding pulse frequency such that the camera can capture the one weld image in each base current phase and peak current phase as shown in Figure 3.3. The base current $I_b = 20$ A is rather small resulting in low arc intensity such that the weld pool can be observed clearly. In contrast, the peak welding current $I_p \geq 100$ A causes strong arc illumination which overwhelms other information. The matched imaging frequency can make sure that both the weld pool images captured in base current phase and arc images captured in peak current phase can be recorded to offer the comprehensive information for monitoring purpose.

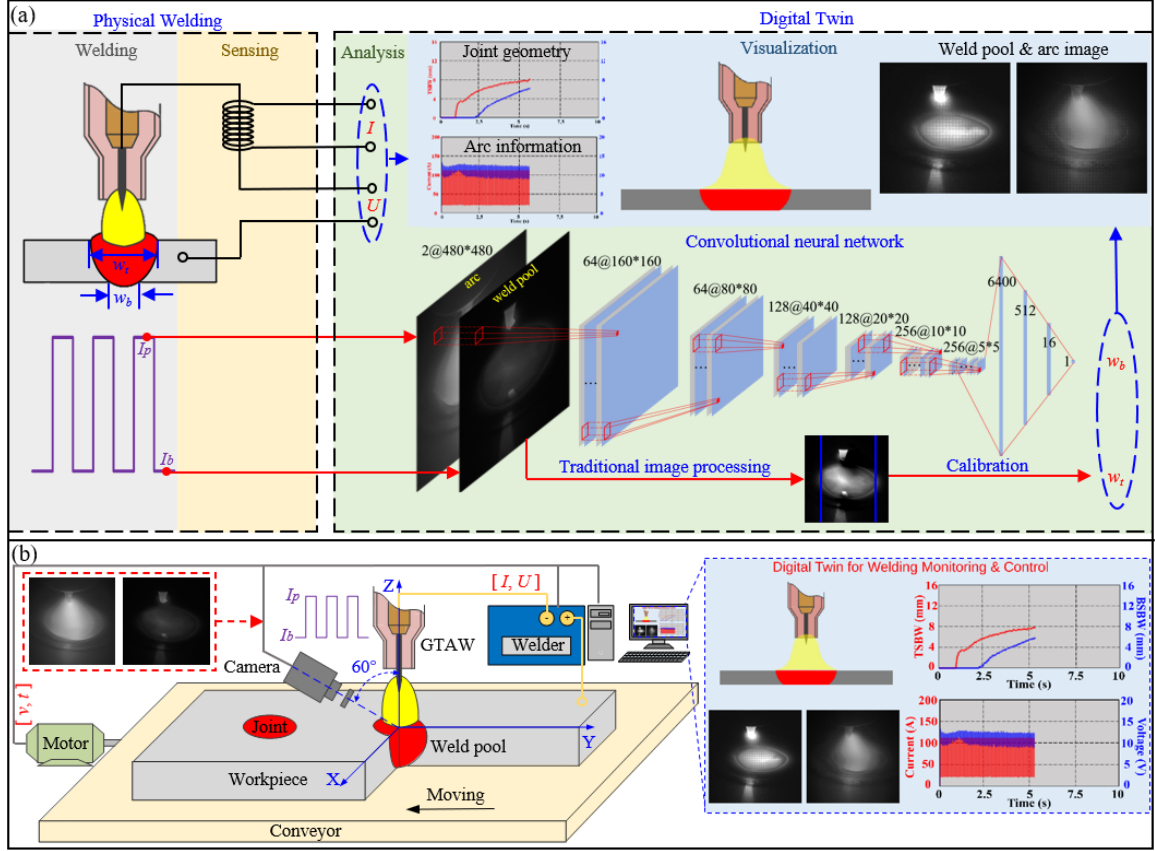


Figure 3.1 System Configuration and Principles (a) Working Principles; (b) Configuration.

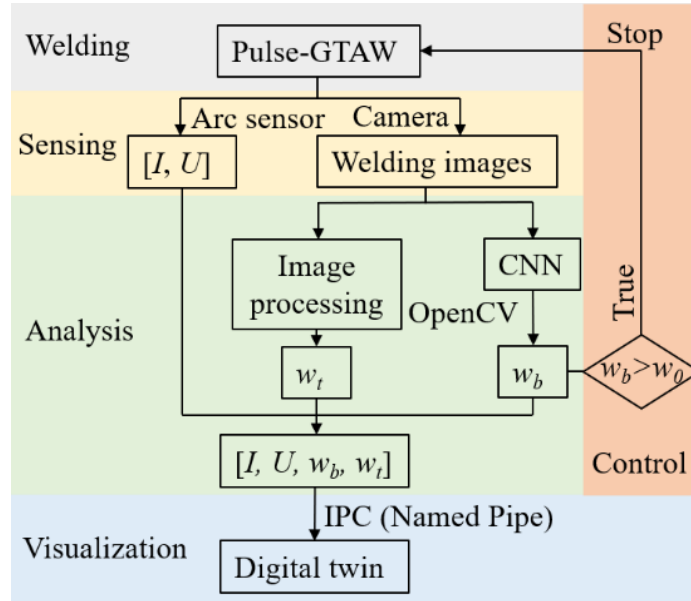


Figure 3.2 The Overall Technical Roadmap.

In the digital twin module, the collected raw data is analyzed/processed to obtain the information of interest firstly. Specifically, the TSBW w_t is computed from the weld pool image by a developed image processing algorithm and the BSBW w_b is predicted from the composite image combined by a weld pool image and an arc image by a trained CNN. Both the image processing and CNN model running are completed in OpenCV environment and programmed with C++ to meet the real-time requirement. Once the predicted BSBW meets the weld quality requirement i.e., $w_b > w_0$, this welding task is considered completed and the next weld joint position is conveyed under the welding torch to conduct the next welding task. In the visualization model, a digital environment is built with Unity engine and C# programming. In order to transmit the information characterizing the running status of the physical welding i.e. $[I, U, w_b, w_t]$ to this digital environment, the named pipes are used to complete the inter-process communication (IPC). As such, a graphical user interface (GUI) is offered for the digital twin visualization.

Table 3.1 Applied Welding Parameters and Camera parameters

parameters	Values	Parameters	Value
Type	GTAW-P	Image size	480*480
Polarity	DCEN	Format	Mono8
Frequency	30 Hz	Frame rate	60 FPS
Duty cycle	50%	Shutter time	0.2 ms
Base current	20 A	Brightness	0.5%
Peak current	100-190 A	Hue	0°
Welding time	10.75-4 s	Saturation	200%
Shielding gas	Argon	Sharpness	3000
Gas flow	7000 SCCM	Gain	0 dB
Material	304L	Gamma	2.5
Thickness	2 mm	-	-

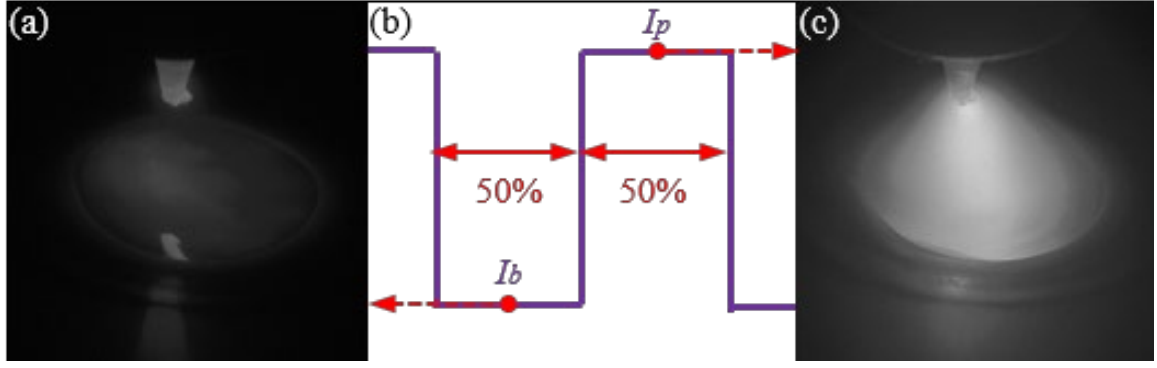


Figure 3.3 Vision Sensing in P-GTAW (a) Image Captured in Base Current Phase; (b) Pulsed Welding Current; (c) Image Captured in Peak Current Phase.

3.3 Information Processing

The information processing aims to extract the undirect information of interest from the collected raw data to make it possible to characterize the physical process more accurately and completely. In our application, the TSBW and BSBW are two indirect parameters characterizing the weld pool geometry and determining the weld quality. We developed a traditional image processing method and a CNN for TSBW and BSBW computation, respectively.

3.3.1 TSBW Computation

As mentioned in Figure 2.1, the TSBW w_t is the width of weld pool which has been contained in the weld pool images and can be obtained by applying an image processing algorithm. To achieve this goal, a watershed segmentation-based algorithm is developed to detect the weld pool boundary. In the watershed segmentation, the image is considered as the land surface where the pixel value stands for the height. In the boundary candidate area, the water begins to be filled in separate local basins. To prevent the continuously rising water in different basins from being merged, the barriers are needed to be built in merged area. Once all the peaks are submerged, all the built barriers are connected as the

boundary for the segmented object. Therefore, the task to find the weld pool boundary can be completed by two steps: 1) identifying the boundary candidates; 2) applying watershed algorithm. The detailed procedures for TSBW computation from weld pool images are shown in Figure 3.4.

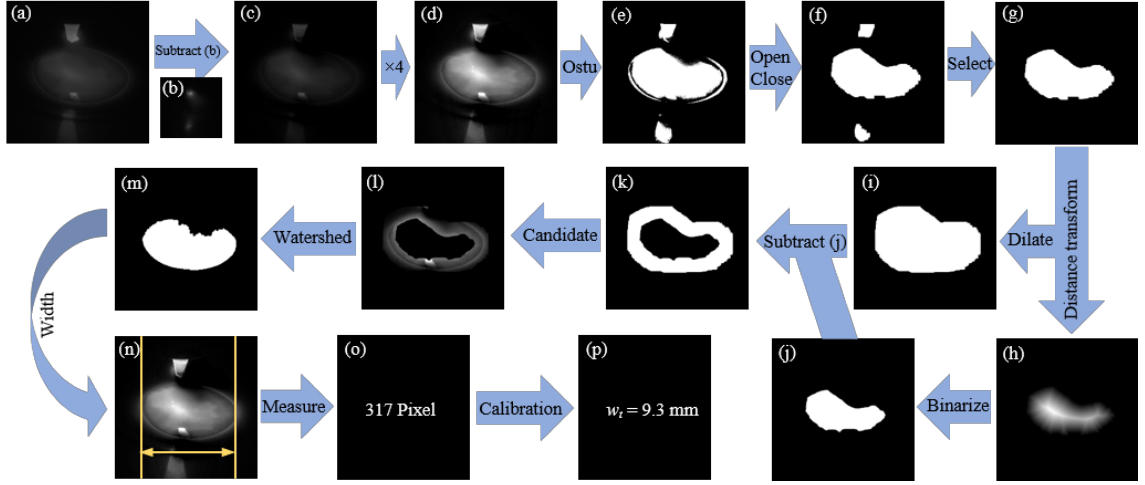


Figure 3.4 Principles for Computing w_t From the Weld Pool Image. (a)-(g) Image Preprocessing for Weld Pool Localization; (g)-(k): Identifying Boundary Candidates; (l)-(n) Weld Pool Boundary Identification Using Watershed; (o)-(p): w_t Computation.

Given a weld pool image I_a as shown in Figure 3.4(a), the background noise is eliminated firstly:

$$I_c = I_a - I_b \quad (10)$$

where I_b is the background pattern and gotten as the firstly-captured image in each welding. The obtained image I_c is rather dark, therefore, it is brightened by 4 times and then binarized by Ostu thresholding:

$$I_d = I_c \times 4 \quad (11)$$

$$I_e = \begin{cases} 255 & \text{(if } I_d \geq T_{Ostu} \text{)} \\ 0 & \text{(if } I_d < T_{Ostu} \text{)} \end{cases} \quad (12)$$

where T_{Ostu} is the thresholding value identified by Ostu's method. To eliminate the small

holes in I_e , the morphology opening and closing are applied twice by a kernel k_0 with size of 7×7 :

$$I_f = I_e \circ k_0 \circ k_0 \bullet k_0 \bullet k_0, \quad k_0 = \begin{bmatrix} 1 & \cdots & 1 \\ \vdots & \ddots & \vdots \\ 1 & \cdots & 1 \end{bmatrix}_{7 \times 7} \quad (13)$$

Then, the image I_f is segmented as three parts corresponding tungsten, weld pool and reflected tungsten, respectively. Image I_g is the selected weld pool part, and this step indicates the completion of image preprocessing.

In the image I_g , the rough area of weld pool has been extracted and then is processed in two parallel routes to identify boundary candidates. The boundary candidates are the difference between the area which is a part of weld pool surely and the area containing the whole weld pool. To identify the former, the distance transformation is firstly done in I_g such that the distance map I_h is computed characterizing the distance to the nearest zero-pixel. After binarization, I_j is the part which can be considered as the weld pool surely:

$$I_j = \begin{cases} 1 & (if I_h > T_{DT}) \\ 0 & (if I_h < T_{DT}) \end{cases}, T_{DT} = 0.2 * \max(I_h) \quad (14)$$

In the meantime, the image I_g is dilated to make sure that weld pool is contained in the processed image I_i :

$$I_i = I_g \oplus k_1, k_1 = \begin{bmatrix} 1 & \cdots & 1 \\ \vdots & \ddots & \vdots \\ 1 & \cdots & 1 \end{bmatrix}_{N \times N}, N = \max(19, 0.1 * \max(I_h)) \quad (15)$$

Therefore, the difference between I_i and I_j contains the weld pool boundary candidates:

$$I_k = I_i - I_j \quad (16)$$

$$I_l = I_k * I_d \quad (17)$$

Once the weld pool candidates are identified, the watershed algorithm is applied in image I_l to extract the weld pool boundary accurately as shown in Figure 3.4(m). Finally, TSBW w_t is computed from the weld pool width as shown in Figure 3.4(n) after the calibration.

3.3.2 BSBW Estimation

As mentioned in before, the BSBW w_b cannot be sensed directly but needs to be estimated from available sensed data. We apply deep learning to estimate it from top-side welding images and this task can be done by two steps: (1) collecting sufficient labeled data and (2) training and validating the CNN models.

3.3.2.1 Data Collection and Pre-processing

The basic pre-requirement to train a deep learning model is to collect sufficient labeled data. Therefore, we install one more camera in the back side for data labeling purpose as shown in Figure 3.5(a). By installing this temporary camera 2, the back-side images are captured whose brightness reflects the weld joint BSBW as shown in Figure 3.5(b). The region of interest (ROI) is firstly selected from the original image and binarized with a threshold. This binarization aims to segment out penetrated area and the threshold value is 80 which is determined after trial-and-error. Then, the penetrated area a_b is computed in pixel. In order to find the mapping relation between w_b and a_b , the calibration experiments are conducted to collect (a_b, w_b) data pairs. Using the welding parameters shown in Table 3.1, the welding experiments are conducted in different peak welding currents (100 A, 130 A, 160 A and 190 A). With each welding current, eight welding experiments are conducted with different welding time to ensure that the collected (a_b, w_b)

data pairs can cover the whole range in general welding manufacturing. Since a_b characterizes the penetrated area, it is proportional to the square of w_b :

$$a_b = k_0 * w_b^2 \quad (18)$$

as such:

$$w_b = k_1 * \sqrt{a_b}, k_1 = \sqrt{k_0} \quad (19)$$

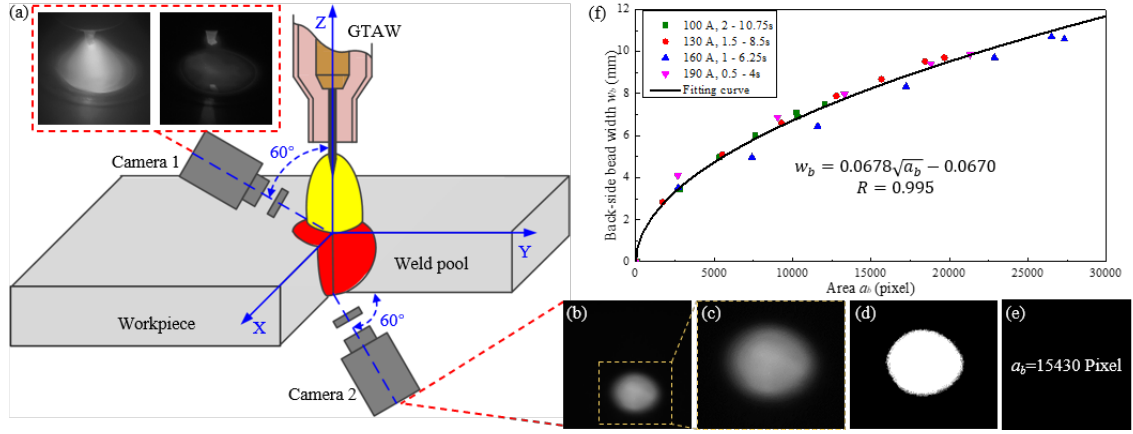


Figure 3.5 Automatic Data Collection and Labeling. (a) System Configuration; (b) Captured Back-side Image; (c) Region of Interest (ROI) Selection; (d) Image Binarization with 80 as Threshold; (e) Computing Back-side Area a_b in Pixel; (f) Mapping Model Between BSBW w_b and the Back-side Area a_b .

To eliminate the error due to the imperfect selection in image thresholding, a correction term b_0 is added in Eq. (19) as the intercept:

$$w_b = k_1 * \sqrt{a_b} + b_0 \quad (20)$$

By computing a_b and measuring corresponding w_b physically in each calibration experiment, 32 data pairs of (a_b, w_b) are obtained (4 welding current levels * 8 welding time levels). The two unknown parameters k_1 and b_0 in Eq. (11) are estimated by least squares (LS) as:

$$w_b = 0.0678 * \sqrt{a_b} - 0.0670 \quad (21)$$

The fitting results are shown in Figure 3.5(f) where the Pearson correlation coefficient (PCC) $R = 0.995$, verifying the effectiveness of the proposed mapping model.

By using the automatic data collection and labeling system in Figure 3.5, welding experiments are conducted for dataset construction. Keeping the base current constant, $I_b = 20$ A, and varying the peak current at $I_p = 100$ A, 110 A, to 190 A, the welding time changes from $T = 10.75$ s, 10 s, to 4 s respectively to ensure that the similar weld joints can be obtained in different welding conditions. Under each welding condition, the welding experiments are repeated 12 times to collect the weld image – BSBW data pairs. Among the 12 repeated welding experiments in the same welding condition, one is selected randomly for validating, another is selected for testing and the remaining ten are for training as shown in Figure 3.6(a). After the dataset construction is completed, the sizes of training dataset, validating dataset and testing dataset are 21950, 2195 and 2195 respectively and their label/BSBW distributions are shown in Figure 3.6(b)-(d). The three datasets have the similar distribution and the data labeled as zero account with largest portion representing the incomplete fusion state appearing in the beginning of welding. The BSBW distributions cover the whole possible range appearing in practical welding manufacturing such that the models trained from training data will be effective in practical welding applications. The validating dataset can help to optimize the model structure and hyper parameters. The testing performance can be used for comparison with other methods as the evaluation criterion.

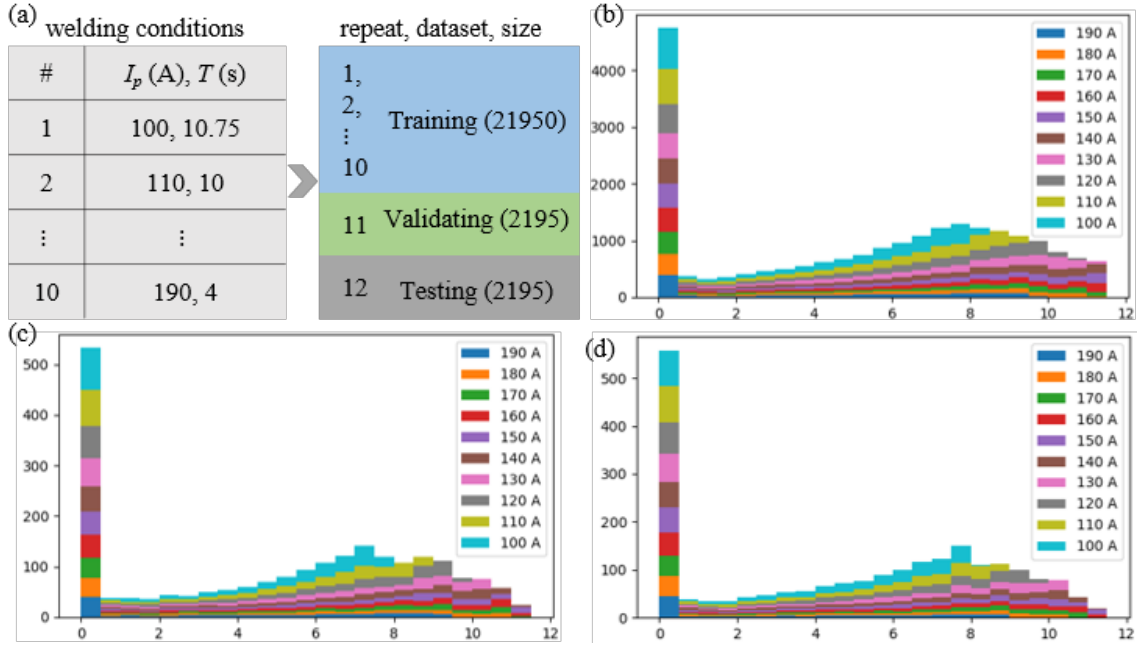


Figure 3.6 Dataset for Deep Learning Model Development (a) Construction; (b) Training Dataset Distribution; (c) Validating Dataset Distribution; (d) Testing Dataset Distribution.

3.3.2.2 Model Training and Validating

The structure of developed convolutional neural network is shown in Figure 3.7 which is inspired from VGG-net [58] which has been proved to own strong ability in feature extraction and reasoning but fewer convolutional layers due to the following two reasons: (1) the data in our task is not complex as theirs such that the features need to be extracted are simpler; (2) the size of available data for model training is $\sim 22K$ which is much smaller than their training dataset, $\sim 1.2M$. The risk of overfitting will increase greatly if the complex models are applied in our applications.

The weld images captured in base current phase and peak current phase characterize the weld pool geometry and arc geometry, respectively. In order to identify the most accurate information for BSBW estimation, we tried three kinds of source images as the

input for the CNN model. Source 1 is the arc image, source 2 is weld pool image and the source 3 is the 2-channel composite image combined by both. In the developed CNN model, the input image is operated by the convolution operations:

$$C_1(k, i, j) = \sum_{l=0}^{L-1} \sum_{m=0}^{M-1} \sum_{n=0}^{N-1} I_0(l, i + m, j + n) \times K_k(l, m, n) + b_k \quad (22)$$

where C_l is the output feature maps, I_0 is the input weld image. K_k is the k th convolution kernel with a size of (L, M, N) and b_k is the bias. Usually, M and N are rather small and $M=N=3$ in our application. L is the channel number of the input feature map. By using the convolution operation with 64 small-size kernels, the local features of previous layers can be extracted and transmitted to the next layer and the shape of the output C_l changes to 64-channel 480*480. In order to endow the non-linear analysis ability, the rectified linear unit (ReLU) activation function is applied:

$$A_1(k, i, j) = \text{ReLU}(C_1(k, i, j)) = \max(0, C_1(k, i, j)) \quad (23)$$

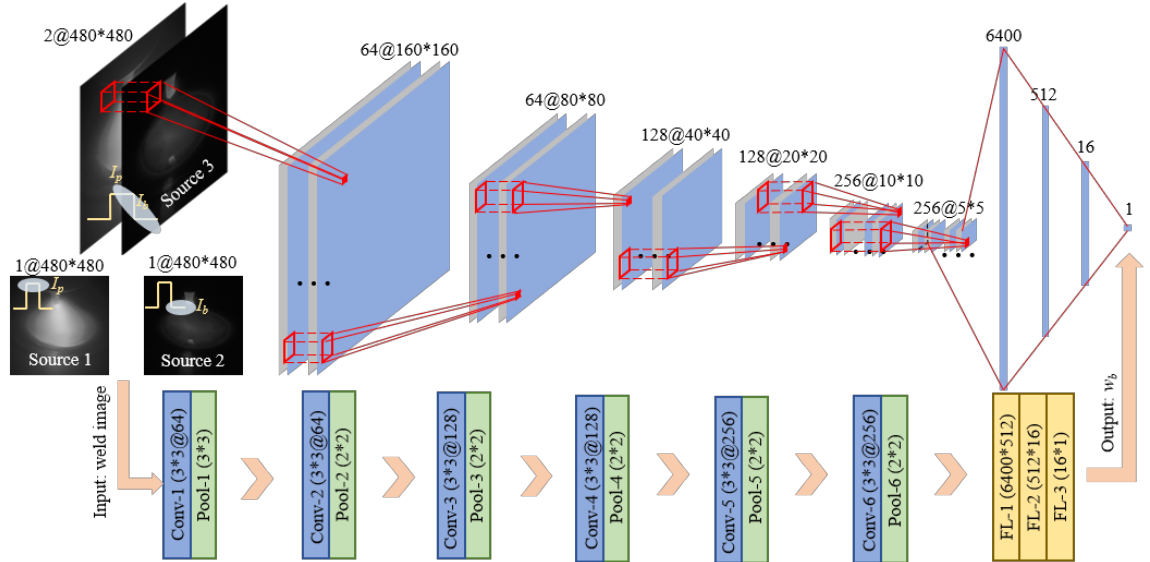


Figure 3.7 Architecture of Developed CNN for BSBW Estimation.

Then, the max pooling operation is applied to decrease model complexity and increase its robustness by compressing a region of data from last layer to its max value:

$$I_1(k, i, j) = pool_{max}(a_1(k, m, n)) = \max(a_1(k, m, n)), \forall (m, n) \in R_{ij} \quad (24)$$

where R_{ij} is the local neighborhood around location (i, j) and is a 3*3 area in first pooling layer. Therefore, the shape of output layer I_1 is compressed to 64-channel 160*160 which is also the input for next layer. In the following convolutional layers (Conv-2 to Conv-6) and pooling layers (Pool-2 to Pool-6), similar operations are done but with different kernel numbers and pooling area sizes. After the six-layer convolution and pooling, the feature map I_6 changes to 64-channel 5*5 and turned as a 6400-length column vector f_0 without changing its value. In the following fully connected layers, feature length is compressed by high-level reasoning:

$$f_1 = ReLU(W_1 * f_0 + b_1) \quad (25)$$

where W_1 is the wight matrix with size of 512*6400 and b_1 is the bias vector with length of 512. The features are compressed further to 16 and 1 finally as the prediction of BSBW w_b :

$$\hat{w}_b = f_3 = ReLU(W_3 * f_2 + b_3) \quad (26)$$

Comparing the estimation and real value of the BSBW, the loss function is defined as the mean square error (MSE) of the training dataset:

$$L = \frac{1}{N} \sum_{i=0}^{N-1} (\hat{w}_b^i - w_b^i)^2 = \frac{1}{N} \sum_{i=0}^{N-1} (f_{CNN}(I_0^i) - w_b^i)^2 \quad (27)$$

where L is the loss function, \hat{w}_b^i and w_b^i are the estimated and real value of BSBW of i th sample, f_{CNN} is the mapping function from the input image I_0^i to the estimated BSBW \hat{w}_b^i , and N is dataset size. The goal of the model training is to find the optimal parameters for kernels, weight matrices and biases denoted as θ to minimize the loss function:

$$\theta = \operatorname{argmin}(L) \quad (28)$$

Due to the high degrees of the nonlinearity in the mapping function f_{CNN} , Eq. (28) does not have the analytical solution and the gradient decent-based backpropagation (GDBP) is applied to obtain the numerical solutions:

$$\theta_{n+1} = \theta_n - lr_n \cdot \nabla_{\theta} L \quad (29)$$

where n is iteration epoch index, lr is learning rate. In the practical applications, the memory required increases linearly with the sample number. Therefore, only a portion of data are used for one iteration which is called minibatch optimization and the size of the data portion for gradient computation M is called minibatch size:

$$\begin{aligned} \theta_{n+1}^1 &= \theta_n - lr_n^1 \cdot \nabla_{\theta} \left(\frac{1}{M} \sum_{i=0}^{M-1} (\hat{w}_b^i - w_b^i)^2 \right) \\ \theta_{n+1}^2 &= \theta_{n+1}^1 - lr_n^2 \cdot \nabla_{\theta} \left(\frac{1}{M} \sum_{i=M}^{2M-1} (\hat{w}_b^i - w_b^i)^2 \right) \\ &\vdots \\ \theta_{n+1}^{N/M} &= \theta_{n+1}^{N/M-1} - lr_n^{N/M} \cdot \nabla_{\theta} \left(\frac{1}{M} \sum_{i=N-M}^{N-1} (\hat{w}_b^i - w_b^i)^2 \right) \end{aligned} \quad (30)$$

In our application, the minibatch size is selected as 10 and the learning rate is computed adaptively using the Adam method [63] with maximum training epoch as 50. Using the three kinds of input image i.e., weld pool image, arc image and composite image, the CNN models are trained and validated with PyTorch library with Python programming and the results are shown in Figure 3.8. During the training epochs, the gradient decent helps to optimize the model parameters to minimize the difference between the predicted BSBW and the real value. As such, the MSE loss both in training data and validating data decreases firstly. After several or tens of training epochs, the validating loss reaches a global minimum which means the trained models have obtained the best prediction in validating data. With the training going on, the training loss decreases continuously, but

the validating loss tends to remain constant even increasing. This indicates the trained models are tending to fit or memorize the training dataset too exactly and the essential underlying patterns are not recognized successfully. Therefore, the trained models cannot be generalized effectively to future unknown data. In order to avoid this issue, the models with best validating performance are considered as the final models for testing and onsite applications and their performance are shown in Table 3.2.

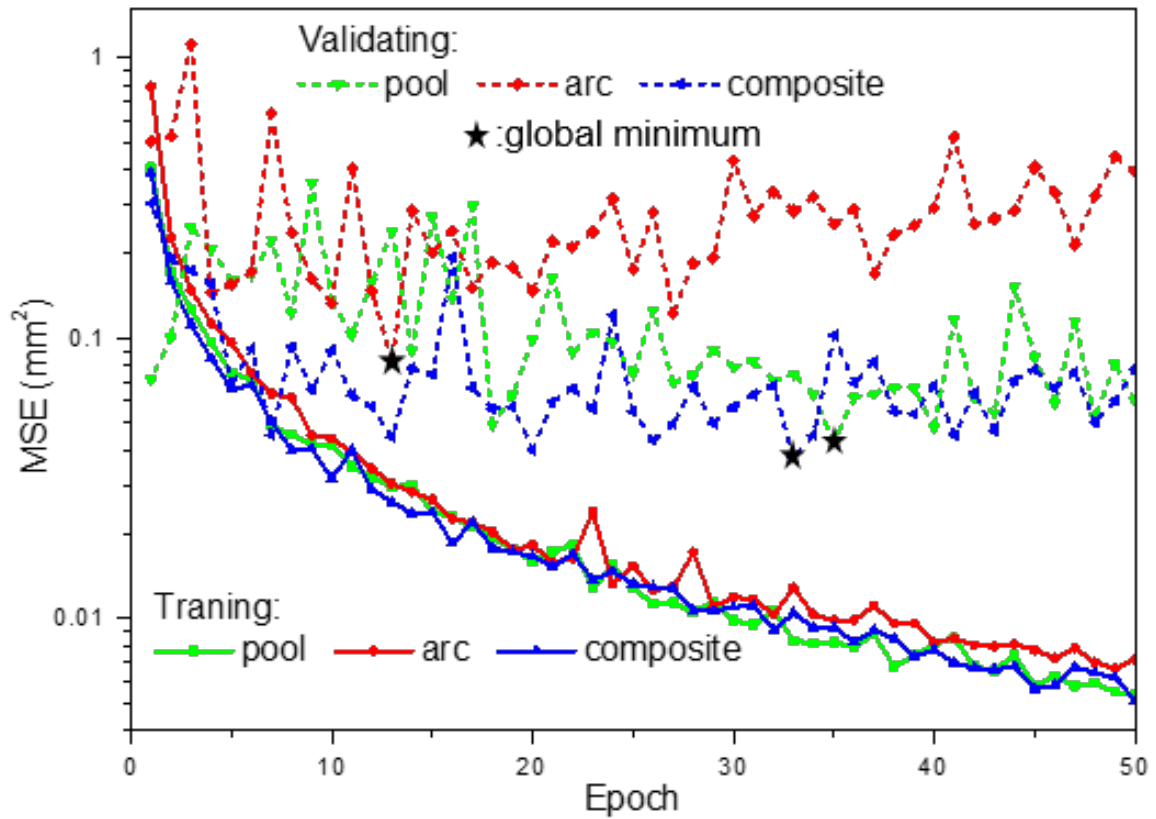


Figure 3.8 CNN Model Training and Validating from Different Information Source.

Table 3.2 The MSE in Validation Dataset and Testing Dataset from Different Input Source

Input	Validation	Testing
Pool	0.043 mm^2	0.056 mm^2
Arc	0.083 mm^2	0.380 mm^2
Composite	0.038 mm^2	0.047 mm^2

From Figure 3.8 and Table 3.2, it can be found that weld pool images are the better information sources for BSBW prediction compared with arc images and can achieve excellent performance with MSE as 0.056 mm^2 . When the information sources are the composite images, the prediction performance can be increased a little with MSE as 0.047 mm^2 . This indicates that the arc geometry can also supplement additional information where weld pool images do not contain for BSBW prediction. The BSBW growth prediction results in 2195 testing samples with different peak welding current are shown in Figure 3.9. In the beginning of welding, the heat received by workpieces is not sufficient to generated full-penetration weld joints such that their BSBWs maintain as zero. With heat accumulated, the weld joints grow gradually with their BSBWs increasing continuously and their growth speeds are dependent on the welding current. During the weld joint growing in all welding conditions, the prediction results demonstrate high similarity and the predicted BSBW can track the real value well. The comparative results between this work and previous works in BSBW prediction from top-side images are shown in Table 3.3. It indicates that the developed CNN-based method with composite weld images obtains the state-of-the-art accuracy.

Table 3.3 BSBW Prediction Performance Comparison

Model	Information	MSE (mm^2)
Linear [104]	Laser image	0.430
BPNN [105]	Laser image	0.387
ANFIS [48]	Laser image	0.185
SVR [106]	Laser image	0.177
Bagging trees [101]	Weld pool image	0.403
CNN [107]	Weld image	0.264
This work	Composite image	0.047

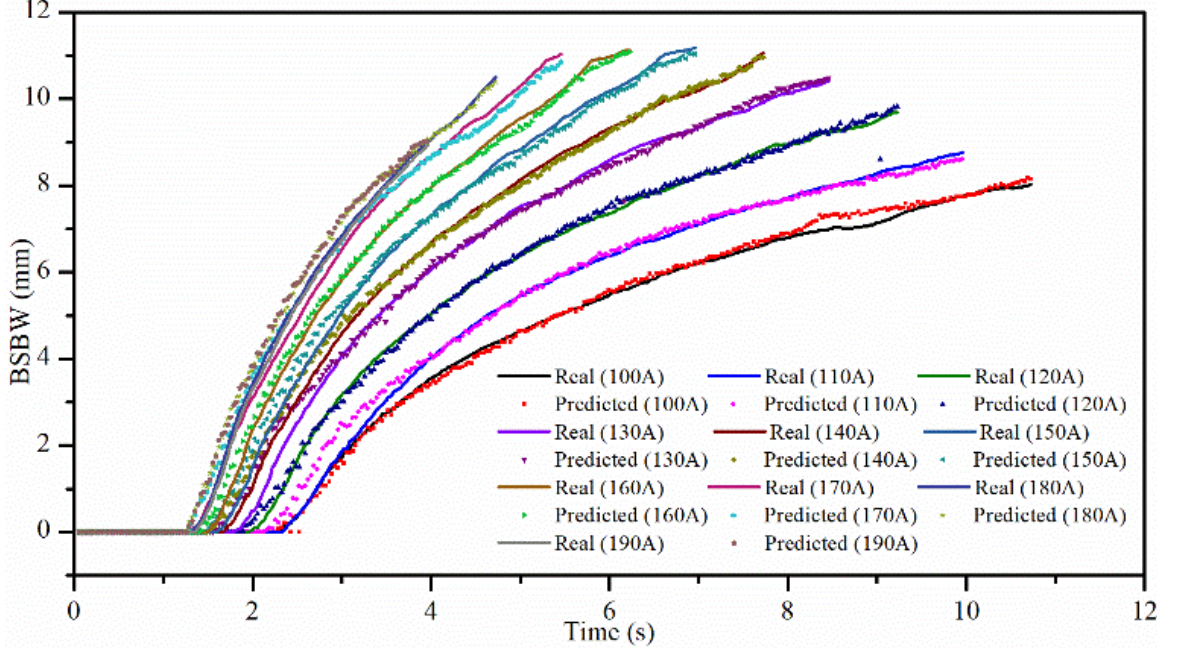


Figure 3.9 BSBW Growth Prediction from Trained CNN and Composite Images in Different Welding Conditions.

3.4 Welding Quality Control

As mentioned in Section 2, the BSBW of a good weld joint must be larger than the thickness-dependent criterion: $w_b > w_0$. In our application, we use automobile industry standard as:

$$w_0 = 4 * \sqrt{T_w} = 4\sqrt{2} = 5.66 \text{ mm} \quad (31)$$

where $T_w = 2 \text{ mm}$ is the thickness of the workpieces. The models trained in Section 3.3 are based on PyTorch in Python environment which is suitable for model design and optimization, but not suitable for model deployment in industrial manufacturing environment considering the computation efficiency and interactivity with hardware. In order to address these issues, the PyTorch CNN model are switched to OpenCV CNN model in C++ programming environment with the Open Neural Network Exchange (ONNX) as the switching interface. In C++ environment, w_b can be predicted accurately

from a composite image and the computing time for one composite image is ~ 0.288 s (~ 4.4 Hz) running in a desktop with an Intel Core I7-6700 central processing unit (CPU) and 16G RAM. After being accelerated by a NVIDIA GeForce GT 730 graphics processing unit (GPU), the computation time is reduced to ~ 0.085 s (~ 12 Hz) which cannot follow the sampling frequency of composite images (30 Hz). We solve this asynchronization problem by using multi-threads, i.e., one thread for composite image collection and another thread for predicting w_b from the composite image by CNN model as illustrated in Algorithm 1. Once the condition $w_b > w_0$ is met, this welding process stops indicating this weld joint is completed and the following welding tasks are continued.

Using the developed algorithm 1, the welding experiments for joint BSBW control are conducted using the welding parameters in Table 3.1 and the obtained weld joints are shown in Figure 3.10. In these experiments, the weld joint BSBWs are predicted from captured weld images in real time with different peak welding current from 100 A to 190 A. In order to meet the same penetration requirement i.e., $w_b > w_0 = 5.66$ mm, the welding time is applied adaptively from 7.45 s to 2.45 s that in general reduces as the peak current increases. As such, all weld joints indexed from A to J demonstrate high consistency even though the peak welding current varies greatly. For each weld joint, its BSBW is measured physically to characterize the control performance. In all weld joints, the maximum BSBW is 7.005 mm and the minimum BSBW is 5.740 mm which indicates that all weld joints meet the size requirement. The mean of all weld joint BSBWs $\bar{w}_b = 6.331$ mm is slightly larger than the penetration baseline with a difference $\Delta w_b = | \bar{w}_b - w_0 | = 0.671$ mm. This difference is the weld joint growth during the time-delay from two aspects: 1) the CNN computation time (> 0.085 s in our application) and 2) the response time of the hardware.

The existence of Δw_b offers redundancy in meeting requirement and the value, 0.671 mm, is small enough to be acceptable for welding tasks. The standard deviation of all weld joints $\sigma = 0.359$ mm which is rather small indicating the high consistency in their sizes. The welding experiments verified the effectiveness of the developed deep learning-based method for penetration control.

Algorithm 1: Joint BSBW control method

Require: w_0 : minimum requirement for w_b
Require: I_b : base current for pulsed welding
Require: I_p : peak current for pulsed welding
Require: T : period of pulsed welding current
 $w_0 \leftarrow 0$ (w_0 initialization)
 $cnn.load()$ (load the trained CNN model)
while $w_b < w_0$ **do**
 $I \leftarrow I_p$ (set welding current as peak value)
 $Img_p \leftarrow camera.capture()$ (capture the arc image)
 wait($T/2$) (wait for peak phase completing)
 $I \leftarrow I_b$ (set welding current as base value)
 $Img_b \leftarrow camera.capture()$ (capture the weld pool image)
 $Img_c \leftarrow Img_p + Img_b$ (composite image construction)
 if $w_0 \geq 0$ **then** (indicates complete w_b computation)
 $w_0 \leftarrow -1$ (flag for incomplete w_b computation)
 $thread(w_b = cnn(Img_c))$ (thread for w_b computation)
 $thread.detach()$ (ensure w_b computation can be done)
 end if
 wait($T/2$) (wait for base phase completing)
end while
 $I \leftarrow 0$ (stop welding)

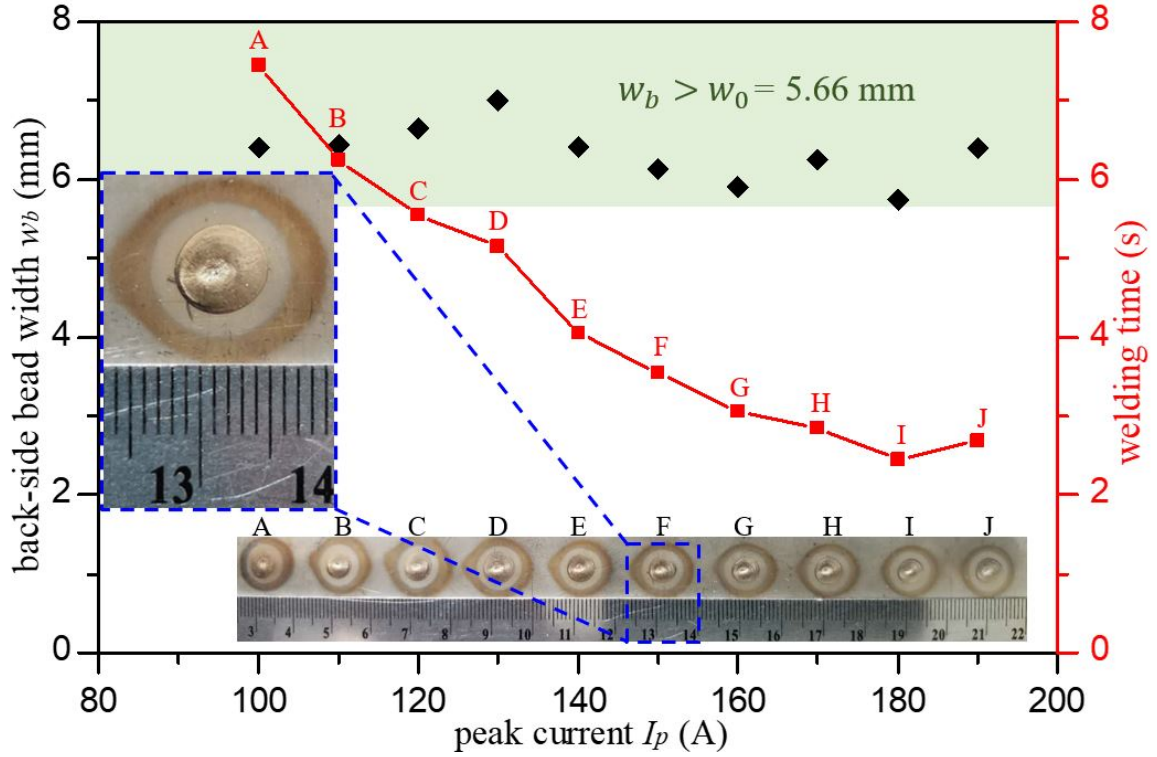


Figure 3.10 Controlled Weld Joint in Various Welding Conditions Based on CNN.

3.5 Visualization in Digital Twin

By applying the developed system, the key information characterizing the welding processes has been digitalized either by monitoring directly or predicting indirectly based on deep learning. The next task is to offer a graphical user interface (GUI) for the digital twin visualization. The Unity, an engine for video game development, is applied as the visualization platform. As shown in Figure 3.11, the GUI includes four zones, I) weld joint growth dynamics; II) weld joint geometry; III) weld images; and IV) arc information. In zone III and IV, the collected weld images and arc information (voltage and current) are shown directly except the weld pool images whose pixels are multiplied by 4 to be seen clearly. In zone II, the weld joint geometry parameters, TSBW and BSBW, are computed as described in Section 3.3 and plotted to offer a quantitative evaluation. In the meantime,

the weld joint dynamic evolution is modeled and shown in zone I from the computed TSBW and BSBW.

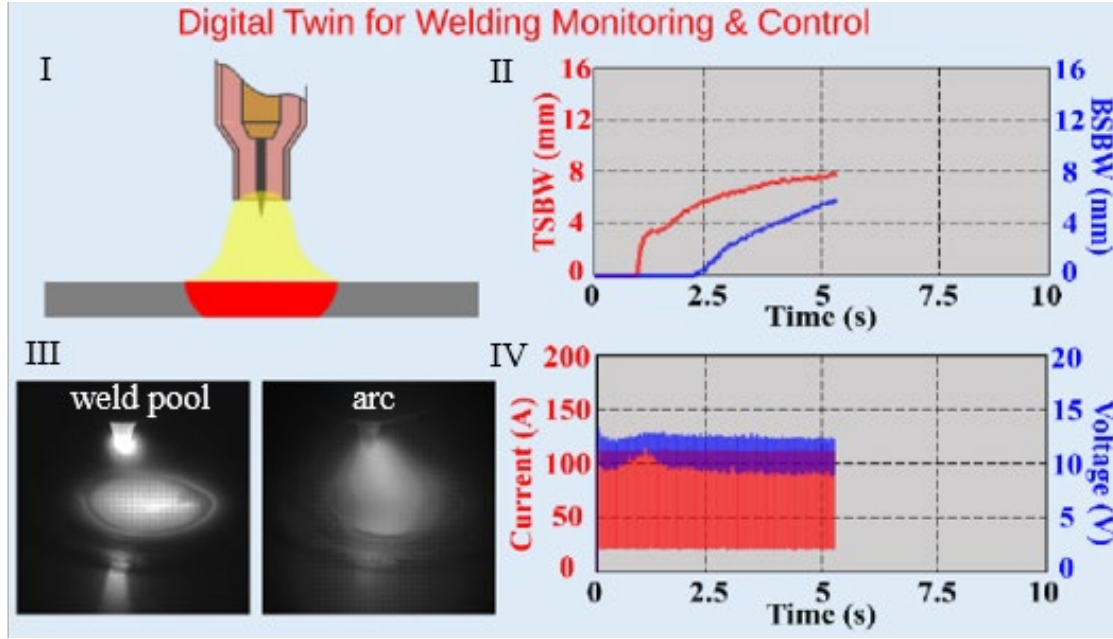


Figure 3.11 GUI for Digital Twin Visualization (I) Weld Joint Dynamic Evolution; (II) Weld Joint Geometry; (III) Weld Images; (IV) Arc Information.

We model the cross section of weld joint as an ellipse with its center as the origin as shown in Figure 3.12(a):

$$\frac{x^2}{a^2} + \frac{y^2}{b^2} = 1 \quad (32)$$

whose major axis $2a = w_t$ such that the semi-major axis can be identified as $a = w_t / 2$. The semi-minor axis b is determined differently depending on the weld penetration states: $w_b = 0$ or $w_b > 0$. When $w_b = 0$ which is the case shown in stage I in Figure 3.12(a), b is assumed to be proportional to a with a coefficient k :

$$k = \frac{b}{a} = \frac{2b}{w_t} = \frac{2T_w}{w_t'} \quad (33)$$

where T_w is workpiece thickness ($T_w = 2$ mm in our application) and w_t' is the TSBW when the joint depth $d = T_w$ as shown in stage II. The coefficient k is computed in all welding conditions which is found to be linear-dependent on the peak current I_p . Figure 3. 12(b) shows the mapping relation: $k = -0.0025 \cdot I_p + 1.1122$ and whose Pearson correlation coefficient $R = -0.9543$ verifying its effectiveness.

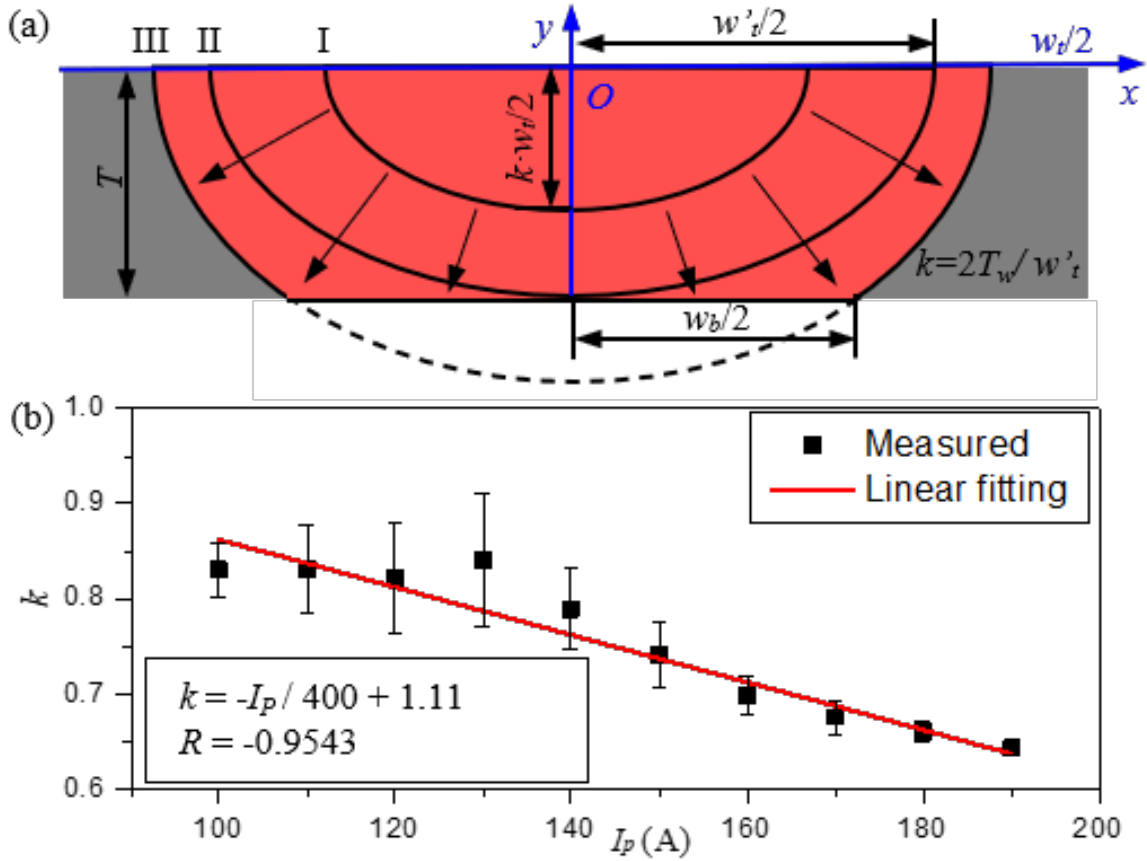


Figure 3.12 Weld Joint Cross Section Contour Modeled as an Ellipse (a) Principles; (b) Ellipse Parameter k Identification.

With BSBW increasing as such $w_b > 0$ as shown in stage III in Figure 3.12(a), both $(w_t/2, 0)$ and $(w_b/2, -T_w)$ satisfies the ellipse equation:

$$\begin{cases} \frac{(w_t/2)^2}{a^2} + \frac{0^2}{b^2} = 1 \\ \frac{(w_b/2)^2}{a^2} + \frac{(-T_w)^2}{b^2} = 1 \end{cases} \quad (34)$$

Solving Eq. (25), the solution of the unknown parameters in ellipse can be obtained:

$$\begin{cases} a = w_t/2 \\ b = w_t \cdot T_w / \sqrt{w_t^2 - w_b^2} \end{cases} \quad (35)$$

By integrating these two cases, the ellipse model of the weld joint cross section is summarized:

$$\begin{bmatrix} a \\ b \end{bmatrix} = \begin{cases} \begin{bmatrix} w_t/2 \\ (k_0 I_p + b) \cdot w_t / 2 \end{bmatrix} (w_b = 0) \\ \begin{bmatrix} w_t/2 \\ w_t \cdot T_w / \sqrt{w_t^2 - w_b^2} \end{bmatrix} (w_b > 0) \end{cases} \quad (36)$$

where $k_0 = -0.0025$ and $b = 1.1122$. By using Eq. (36) and computed w_t and w_b , the weld joint dynamic evolution is visualized in this GUI and offer the intuitive and effective perception to the users.

3.6 Summary

An innovative deep learning-empowered digital twin for welding joint growth monitoring, control and visualization is developed in this chapter to promote the development of smart welding manufacturing. In such a system, the deep learning enhances the analysis ability of the digital twin greatly and helps to obtain the state-of-the-art accuracy in BSBW prediction from the captured composite weld images. After applying the developed traditional image processing method, the TSBW can also be computed from weld pool images. As such, the weld joint growth is monitored in real time, and the penetration state is controlled accurately to meet the quality requirement. With integrating all information charactering the welding process, its digital twin is built and

run in virtual environment synchronously and visualized as a GUI for users perceiving the welding process running status intuitively and effectively.

CHAPTER 4. DIGITAL TWIN FOR HUMAN-ROBOT INTERACTIVE WELDING

4.1 Introduction

In current developed digital twins, humans are the observers of the physical systems where the information flow is unidirectional, i.e., human users receive the information from the physical systems or their digital twins. However, physical systems cannot receive feedback or actions from human users. This unidirectional working mode is only effective for those processes dominated by machines. For processes where intelligence from humans is needed like precise welding, spraying, and rescue, human-machine interaction (HMI) or human-robot interaction (HRI) [108] needs to be integrated with the digital twins such that humans' operative ability can be enhanced and the roles they play transit from observers to dominators. To facilitate HMI or HRI, we need to select an effective interface from the existing candidates such as joysticks [79], haptic gloves [80], gestures [81], speech [82] and virtual reality (VR) [109]. Among them, VR aims to build a computer-generated virtual environment and offer the immersive visualization and natural interaction to human users with cheaper cost and safer operating environment. Compared with other interfaces, it owns the following advantages such that we believe it is suitable for HMI or HRI when integrated with digital twins: (1) some customer-grade VR systems have been commercialized with available application programming interfaces (APIs) for development, e.g. HTC VIVE, Facebook Oculus and Sony PlayStation VR; (2) the immersive 3D virtual spaces in VR are perfect for visualizing elements and their dynamics in digital twins; (3) VR offers natural and direct interactions by motion-tracking handles such that human users can demonstrate their operations as usually without additional

adaptive practice. Therefore, we select VR as the interface to be integrated in digital twins for human-robot interactive welding.

4.2 System Configuration

As shown in Figure 4.1, the developed digital twin for HRI in welding manufacturing is composed of a physical HRI and its digital twin part. The whole system is developed based on HTC VIVE VR system. In the physical HRI part, a human user holds a composite torch composed of a manual welding torch and a motion-tracking handle, as shown in Figure 4.2. This handle is part of HTC VIVE, and its surface markers can be captured by infrared cameras with its inertia measured simultaneously such that it can be tracked in real-time. The tracking accuracy can reach submillimeter for static state [110] and 1-2 mm error in dynamic tracking, which is sufficient to successfully complete some precise grasp and handling tasks [99]. Also, even for the unsuccessful tasks, tracking accuracy is not the main limiting factor but the force, as the human would teleoperate the robot to reach to the desired pose with the iterative visual feedback regardless the tracking error [99]. Furthermore, compared with these application tasks in previous works, the movements in welding are relatively slow, which decrease the effect of tracking error further. Therefore, the tracking accuracy from HTC Vive can meet the welding application requirements. The attached handle endows the interactive ability to the manual welding torch such that the human user could demonstrate her/his welding operations naturally and directly offsite. Via the VR system, the demonstrated welding operations are recorded. In the physical welding environment, a robot with six degrees of freedom (6DoF), UR-5, executes the human user's operations to conduct the welding jobs by attaching a gas tungsten arc welding (GTAW) torch as its end-effector.

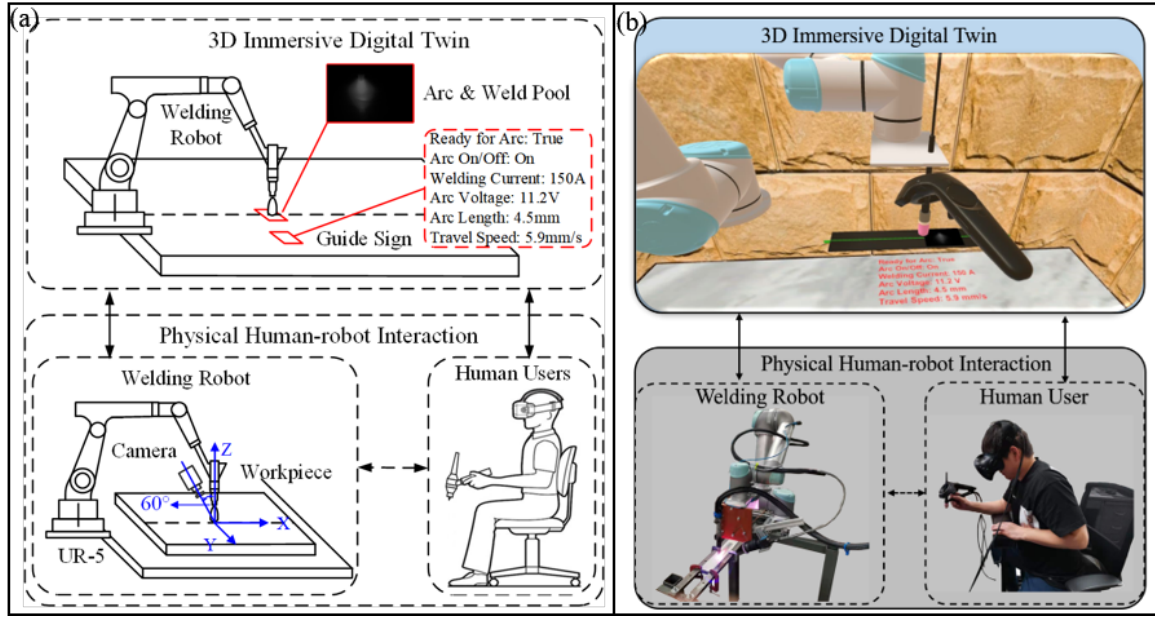


Figure 4.1 Developed Digital Twin for HRI in Welding Manufacturing (a) Schematic Diagram (b) Real Diagram.

In this digital twin, all the vital elements in physical HRI, including the robot, welding scene, and human user, have their digital replicas to precisely simulate the dynamics in the physical world. When building the essential elements in this digital twin, different strategies are applied due to their various physical properties. For the rigid elements such as the robot, welding torch, and workpiece, their geometrical shapes maintain static, and only their positions and orientations need to be updated. To decrease the data volume and computation cost, their 3D models are pre-built offline and loaded into digital twin. For the deformable elements such as the weld pool and electrical arc, their images are captured by Point Grey FL3FW03S1C, an industrial camera that is laterally mounted on the robot. The weld pool images then go through a band-pass optical filter centered at 650 nm where the arc is weak, to avoid the intensive arc overwhelming the welding scenes. Then, the filtered images are projected on the workpiece surface under

the welding torch in the digital twin system. Simultaneously, some other key information determining welding quality, including welding current, arc voltage, arc length, and welding speed, is sensed and visualized in text streaming. The digital twin is developed using C# in Unity, a game engine supporting all mainstream VR hardware.

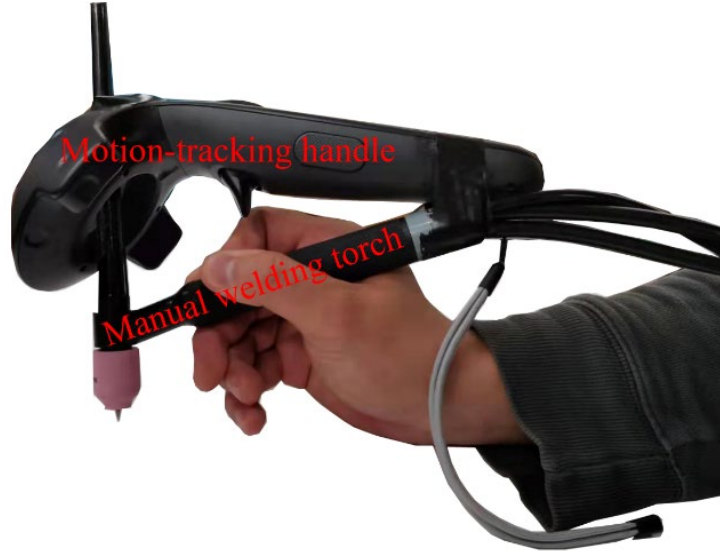


Figure 4.2 The Human User Demonstrates the Welding Operations Via a Composite Torch Which is Composed of a Manual Torch and a Motion-tracking Handle.

4.3 Working Principles

The working principles of the developed digital twin for HRI are shown in Figure 4.3, where four spaces, including human space (H), digital space (D), robot space (R), and welding space (W), coexist with a layered architecture.

In one working cycle, the human user demonstrates her/his welding operations O^H in human space while observing and analyzing the information I^H from the digital twin. This reaction model, $O^H = M_{IO}^H(I^H)$, is human user-dependent and characterizes the welding skill. The demonstrated welding operation vector O^H including welding torch movement and the applied welding current:

$$O^H = [P^H, Q^H, i^H] \quad (37)$$

where $P^H=[x^H, y^H, z^H]^T$ describes torch movement in 3D space, and $Q^H=[Q_w^H, Q_x^H, Q_y^H, Q_z^H]$ is the quaternion characterizing the orientation of the welding torch human space. i^H is the command welding current.

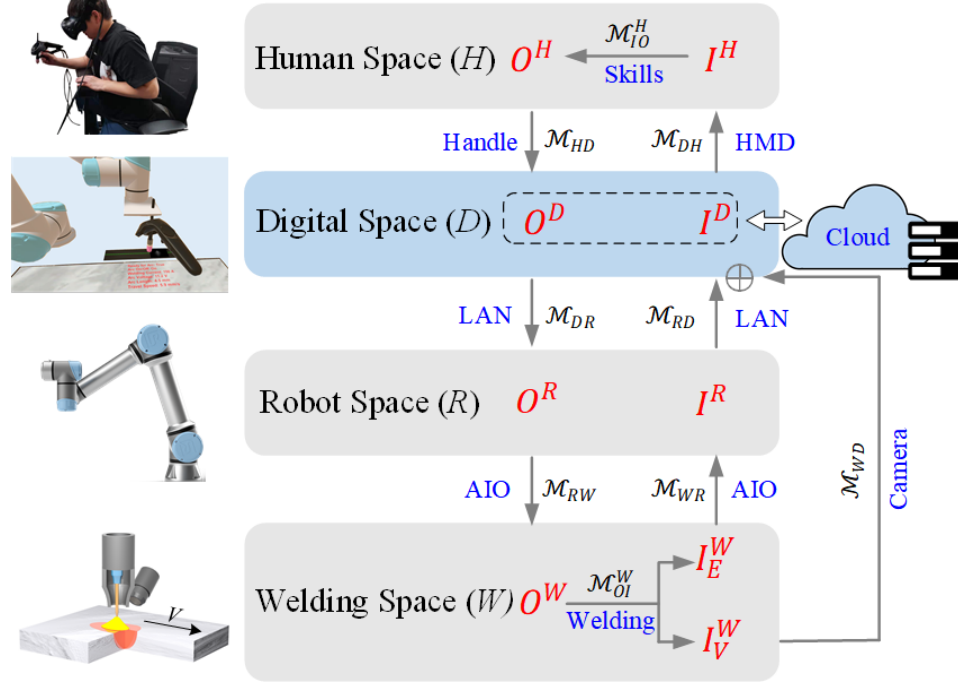


Figure 4.3 System Working Principles. Physical HRI Covers Human Space, Robot Space and Welding Space and Its Digital Twin Exists in Digital Space.

Then, the human operation is transmitted into the digital space as:

$$O^D = [P^D, Q^D, i^D] = M_{HD}(O^H) \quad (38)$$

where O^D is the mapped welding operation in digital space, including position P^D , orientation Q^D , and welding current i^D ; this transmission is completed via the motion-tracking handle and modeled as M_{HD} . More specifically, the P^H and Q^H can be sensed in real-time by the internal motion tracking function from HTC VIVE with a 3D coordinate transformation:

$$\begin{cases} P^D = R_H^D \cdot P^H + \Delta P_H^D \\ Q^D = Q_H^D \cdot Q^H \end{cases} \quad (39)$$

where R_H^D and Q_H^D are the rotation matrix and quaternion for spatial coordinate transformation and ΔP_H^D is the origin deviation between human space and digital space, which can be pre-identified based on their spatial relation. The dynamic adjustment of welding current, revealed by the relative position of human thumb in touchpad, is simultaneously transmitted to digital space, as shown in Figure 4.4.

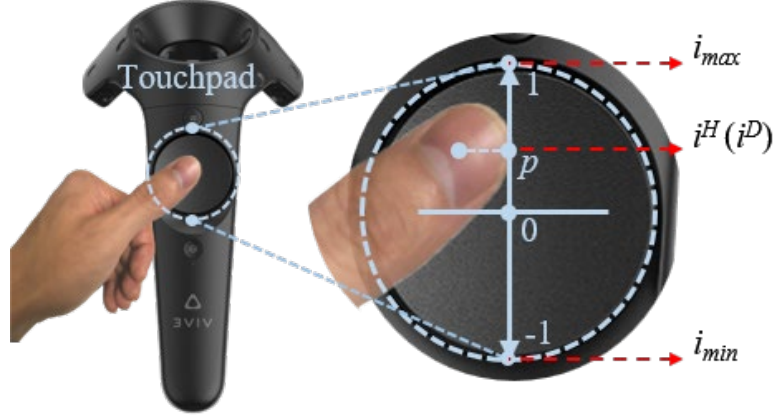


Figure 4.4 The Human User Controls the Welding Current by Sliding the Thumb Position on Touchpad.

The human user slides her/his thumb position p , which is scaled to $[-1, 1]$ and mapped further to welding current range $[i_{min}, i_{max}]$ as the applied welding current:

$$i^D = i^H = \frac{(i_{max} - i_{min})p}{2} + \frac{(i_{max} + i_{min})}{2} \quad (40)$$

A similar spatial coordinate transformation is done to transmit the welding operations from digital space to robot space:

$$O^R = M_{DR}(O^D) \rightarrow \begin{cases} P^R = R_D^R \cdot P^D + \Delta P_D^R \\ Q^R = Q_D^R \cdot Q^D \\ i^R = i^D \end{cases} \quad (41)$$

Since UR-5 robot only accepts axis-angle to characterize its orientation, the quaternion is transformed to axis-angle by:

$$r^R = [r_x^R, r_y^R, r_z^R] = \frac{2 \cdot \arccos(Q_w^R)}{\sqrt{1 - Q_w^R \cdot Q_w^R}} \cdot [Q_x^R, Q_y^R, Q_z^R] \quad (42)$$

where $r^R = [r_x^R, r_y^R, r_z^R]$ is the axis-angle representation characterizing the same orientation as Q^R .

A local area network (LAN) is built for information communication between the physical and the digital worlds using TCP/IP protocol. The robot receives the transformed operation $O^R = [P^R, r^R, i^R]$ and rotates its joints to reach the target pose $[P^R, r^R]$ such that the robot can execute the human welding operations in robot space. In the meantime, the welding current is transmitted to the welding power supply via analog input/output (AIO) interface, such that the desired welding current is applied. With the movement of welding torch attached to the robot, the welding process is conducted in the welding space with welding information generated:

$$[I_E^W, I_V^W] = M_{OI}^W(O^W) \quad (43)$$

where O^W includes welding torch movement and applied welding current; I_E^W and I_V^W are generated electrical information and visual information, respectively; M_{OI}^W is the mapping model that can characterize the welding process. $I_E^W = [i_r^W, u_r^W]$ includes the real welding current i_r^W and the arc voltage u_r^W , which are sensed by embedded arc sensors in the welding power supply. I_V^W is the geometry of the weld pool and the electric arc, which is sensed by the industrial camera. The I_E^W is transmitted to robot space via the AIO interface and integrated with the information characterizing the robot movement:

$$I^R = [J_0^R, J_1^R, J_2^R, J_3^R, J_4^R, J_5^R, v^R, i_r^R, u_r^R] \quad (44)$$

where $J_i^R \in [-2\pi, 2\pi]$ ($i = 0, 1, \dots, 5$) is the rotation degree of i^{th} joint of the robot; v^R is the robot tool center point (tungsten tip) movement speed which is key information for welding performance; i_r^R and u_r^R are the sensed welding current and voltage. With the

same LAN, the information in robot space I^R is transmitted into the digital space to build the digital twin. In this digital twin, the workpiece model is pre-loaded since it does not change during welding. The robot model is also pre-loaded, but its joint rotation degrees are from sensing data $[J_0^R, J_1^R, \dots, J_5^R]$ to reconstruct its movement in the physical space. The welding information is represented in two ways: (1) the electrical information including sensed welding current and arc voltage and the welding speed are represented by text sign; (2) the visual information including weld pool and the electrical arc is represented by the captured images. This digital twin (I^D) covers all digital replicas of the physical elements and updates itself by the information stream from physical human-robot interactive welding. Therefore, it works not only as an interface for human user perceiving information for demonstrating operations but also opens a window for further monitoring and analyzing the demonstrated operations and resulting welding performance. Simultaneously, all the data after digitalization is stored in the cloud for further storage and sharing. By the head-mounted display (HMD), the digital twin is visualized and shown to the human users as I^H . The human user can adjust her/his position to observe her/his interesting information and demonstrates the welding operations. This cycle repeats until the welding tasks are completed.

The developed digital twin system shares some similarity with the typical HRI, VR and augmented reality (AR), but some fundamental differences exist. Compared to a typical HRI system configuration, where the welding and robot scenes are captured by the sensors and then directly presented to the humans, this developed digital twin system only needs to update embedded welding workspace and robotic models with some key

parameters. As such, the burden from data collection, processing, and storage is significantly reduced without sacrificing the onsite scene reconstruction accuracy.

In VR environment, the displayed scenes are from computational simulation where no real elements are involved. This digital twin is built upon VR, but with the simulation models recursively updated by the real-time sensing data streaming. For example, in the developed digital twin system, a simulation model of the robot is preloaded to the digital twin system, which is similar as VR. Then the robotic movements are obtained from sensing data, such as the rotation angle of each joint in robots. So, the difference between VR and digital twin lies in whether real-world information is used to update the simulation models in the virtual display.

On the other hand, the AR environment is built upon the real world, with adding the virtual elements generated from computational simulations to the real-world scenes to enhance the users' perception of the real world. Instead of being separated spatially as in digital twin, the real elements and virtual elements in the AR environment are coupled and presented to the users together.

4.4 Summary

By integrating VR as an HRI interface, the developed digital twins own the interactive ability with human users and is applied to welding manufacturing successfully. In such a digital twin, all the key elements in a physical world have their digital replicas and these replicas run with the same dynamics as the physical ones by the information communicating between the physical and digital worlds.

CHAPTER 5. WELDER BEHAVIOR ANALYSIS

5.1 Introduction

Facing different welding conditions and disturbance, the welders especially the skilled welders can adjust the welding parameters rapidly adaptively. As such, the negative effect from the external disturbance can be minimized. That is the advantages of human welders compared with robots and also where the robots need to learn for next-generation intelligent robots. In order to achieve this goal, one of the pre-requirements is to collect the welder behaviors during manual welding and recognize the underly patterns from their demonstrated behaviors. In our developed digital twin system, the human welder behaviors are captured by VR and stored in cloud. Therefore, it is possible to apply the data-driven methods to complete the analysis and recognize the underlying pattern difference between skilled welders and unskilled welders. Then, the recognized patterns can help to welder training.

5.2 Principles

With the developed digital twin for human-robot interactive welding, the welder behaviors responding to welding scenes modeled as M_{IO}^H characterize human users' welding skills and can be recorded completely. The human welders with different professional levels should demonstrate different patterns and conducting their analysis will help to understand the underlying patterns from the skilled welders and benefit to novice welder training. In this section, a data-driven approach, FFT-PCA-SVM, as a combination of fast Fourier transform (FFT), principal component analysis (PCA) [111], and support vector machine (SVM) [112], for welding skill classification from the demonstrated

operation data is developed. Its overflow is shown in Figure 5.1, which includes two stages: (1) data pre-processing; and (2) model development.

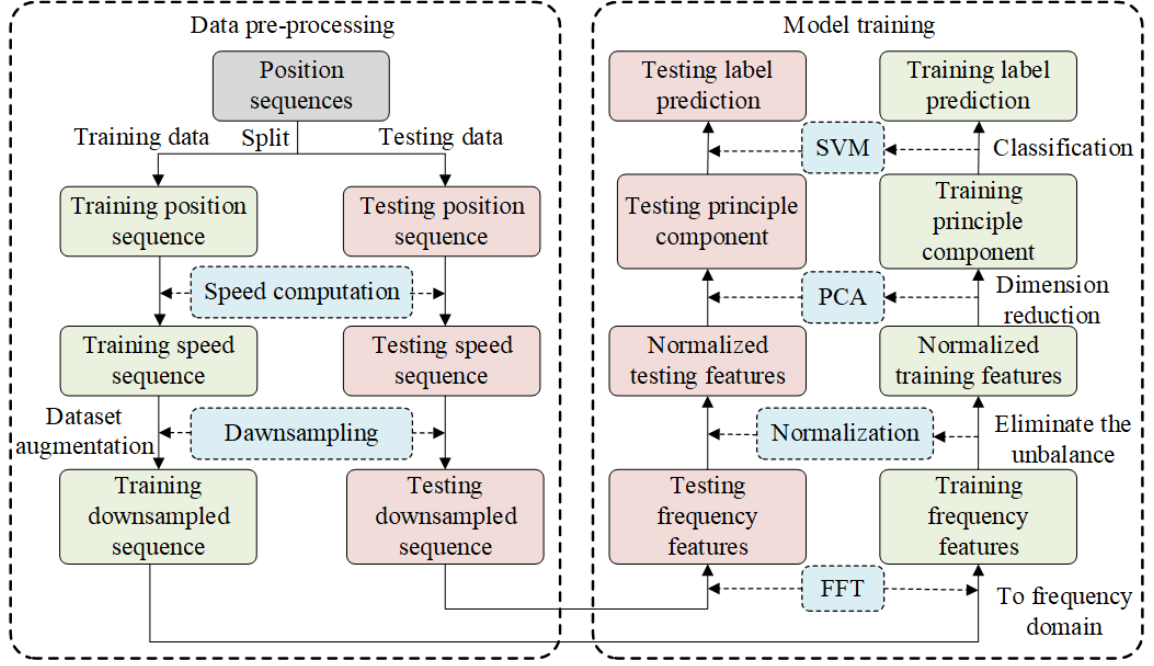


Figure 5.1 The Overflow of Proposed Welding Skill Level Classification Model from Demonstrated Operation Data.

In the data pre-processing stage, all the demonstrated operation data are downloaded from the cloud firstly. These operations are the movement position sequences $P[n] = \{P_0, P_1, \dots, P_N\}$ in 3D space where each element in the sequence $P_n = [P_n^x, P_n^y, P_n^z]$ characterizing the welding torch position at time t_n .

Then, the downloaded position sequences are split randomly for constructing a training dataset and testing dataset with a ratio of 9:1. For welding, the travel speed of welding torch is a major parameter determining the heat input to workpiece and weld quality such that it is more important than the absolute position. Therefore, we transform the position sequences to speed sequences by:

$$v[n] = \{v_0, v_1, \dots, v_{N-1}\} v_n = \frac{P_{n+1} - P_n}{t_{n+1} - t_n} \quad (45)$$

In order to augment the dataset size, downsampling is applied with the decimation factor $M = 30$:

$$vv[n]_{\downarrow M} = \begin{cases} v[Mn] \\ v[Mn + 1] \\ \dots \\ v[Mn + M - 1] \end{cases} \quad (46)$$

By downsampling, one original speed sequence with sampling frequency as 90 Hz (with N as length) can generate 30 speed sequences with a sampling frequency of 3 Hz (with $N/30$ as length), which is adequate since this process is relatively slow. Then, the size of the training dataset and the testing dataset is increased by 30 times.

The model training stage presents the principles of developed FFT-PCA-SVM. Firstly, the downsampled speed sequences $v[n]$ are transformed into the frequency domain based on FFT, which is a more efficient way to realize the discrete Fourier transform (DFT):

$$f_k = \left| \sum_{n=0}^{N-1} v_n e^{-2\pi k i \frac{n}{N}} \right| \quad k \in \{0, 1, \dots, N-1\} \quad (47)$$

where $f = [f_0, f_1, \dots, f_{N-1}]$ is the transformed frequency feature vector, and each element f_k characterizes the spectrum magnitude of travel speed at a specific frequency $(k/N) \cdot F_{ori}$; N is the length of downsampled sequence length; $F_{ori}=3$ Hz is the sampling frequency.

We apply FFT to transform the speed sequences to frequency features considering the following three reasons: (1) the welding skill difference between skilled and unskilled welders can be characterized/classified better in frequency domain compared with the original time domain, which has been verified by previous research works [113][114][115]; (2) each feature f_k in the frequency feature vector f is independent with others f_l ($l \neq k$) since the base functions $e^{-2\pi i n/N}$ in FFT are orthogonal with each other. This

independence meets the basic requirements by most machine learning models on training data. Otherwise, a more complex sequential modeling technique is needed; and (3) there is no information losing after FFT since the base function set $[e^{-2i0/N}, e^{-2i1/N}, \dots, e^{-2i(N-1)/N}]$ is a complete set. In our application, the transformed frequency features are symmetric about zero since the speed sequences are real numbers such that we only keep the positive frequency features. Furthermore, the computed frequency features in x , y and z are concentrated as the final whose length is $3N/2 + 3$:

$$F = [f_0^x, \dots, f_{N/2}^x, f_0^y, \dots, f_{N/2}^y, f_0^z, \dots, f_{N/2}^z] \quad (48)$$

In order to eliminate the unbalance among the feature vector $F = [f_0, f_1, \dots, f_{N-1}]$ ($N = 3N/2 + 3$), normalization is applied by:

$$f'_i = \frac{f_i - u_i}{\sigma_i} \quad (49)$$

where f'_i is the normalized feature; u_i and σ_i are the mean and standard deviation of the f_i in training data.

After eliminating the unbalance, PCA is applied to reduce the data dimension and computational cost. During this process, N orthonormal base vectors w_0, w_1, \dots, w_{N-1} in a R^N space are obtained, and these vectors explain the original data variance in a descending order. Then, each normalized frequency feature vector can be transformed into the new coordinate system that is spanned by w_0, w_1, \dots, w_{N-1} :

$$F^T = [f_0^T, f_1^T, \dots, f_{N-1}^T] \quad (50)$$

whose element $f_i^T = f' \cdot w_i$ is the projection of the normalized frequency feature vector f' on the w_i which is the i^{th} principal component. With i increasing, the distribution variance of f_i^T decreases, which means the whole dataset is less distinct in this principal component.

Therefore, the data dimension can be reduced to M ($M < N$) from original N if we only

keep the first M elements as $F^R = [f_0^R, f_1^R, \dots, f_{M-1}^R]$ with minimized performance sacrifice in differentiating the original data due to dimension reduction. The bases vectors w_0, w_1, \dots, w_{M-1} can be computed by singular value decomposition (SVD) and the reduced normalized frequency features $F^R = [f_0^R, f_1^R, \dots, f_{M-1}^R]$ is the liner combinations of original frequency feature but own descending largest distribution variance.

The final step is to train an SVM to classify the professional level (skilled welders or unskilled ones) from the reduced normalized frequency features F^R and its principles are shown in Figure 5.2.

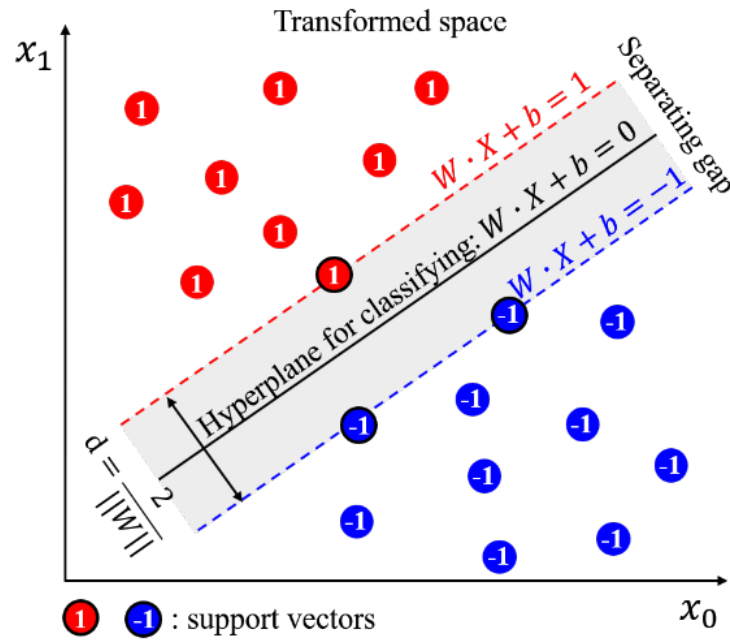


Figure 5.2 The Principles of SVM.

Firstly, the original features are transformed into feature space by a transformed function Φ :

$$X = [x_0, x_1, \dots, x_{N-1}] = \Phi(F^R) \quad (51)$$

where Φ can be a linear or non-linear function that transforms the original features F^R into a high-dimensional space as X . In model training and applying, Φ is defined implicitly, but another function characterizing the inner product of the two transformed feature vectors is defined as kernel function K by:

$$K(F_i^R, F_j^R) = \Phi(F_i^R) \cdot \Phi(F_j^R) \quad (52)$$

In this transformed feature space, we aim to find a hyperplane, $W \cdot X + b = 0$, to separate the data into two classes (labeled as Y whose value can be +1 or -1) with maximizing the separating gap width $d = 2 / \|W\|$ between the two margin hyperplanes $W \cdot X + b = \pm 1$:

$$\begin{aligned} \min_{W, \Phi, b} \frac{1}{2} \|W\|^2 \quad \text{subject to} \\ Y_i(W \cdot X_i + b) = Y_i(W \cdot \Phi(F_i^R) + b) \geq 1 \end{aligned} \quad (53)$$

In order to avoid the situation where the data cannot be separated perfectly, the “soft-margin” is used adding an ε as the penalty for imperfect separation conditions:

$$\begin{aligned} \min_{W, \Phi, b} \left(\frac{\lambda}{2} \|W\|^2 + \frac{1}{L} \sum_{i=0}^{L-1} \varepsilon_i \right) \quad \text{subject to} \\ \begin{cases} Y_i(W \cdot X_i + b) = Y_i(W \cdot \Phi(F_i^R) + b) \geq 1 - \varepsilon_i \\ \varepsilon_i \geq 0 \end{cases} \end{aligned} \quad (54)$$

where λ is the trade-off parameter for margin distance and separability; L is the training data size, and this problem can be solved using quadratic programming [116].

5.3 Experimental Verification

In order to verify the effectiveness of the developed digital twin for human-robot interactive welding and developed FFT-PCA-SVM for welder behavior analysis, six welders, three skilled with certain manual welding training and three unskilled without any training, are invited to complete a simple welding task where the parameters for welding

and workpieces are shown in Table 5.1. Each welder completes the welding job ten times, and no error occurs. During our experimental verification stage, it is found that the weld beads from the skilled welders are uniform and satisfied in both sides, but those from the unskilled welders are not satisfied as shown in Figure 5.3.

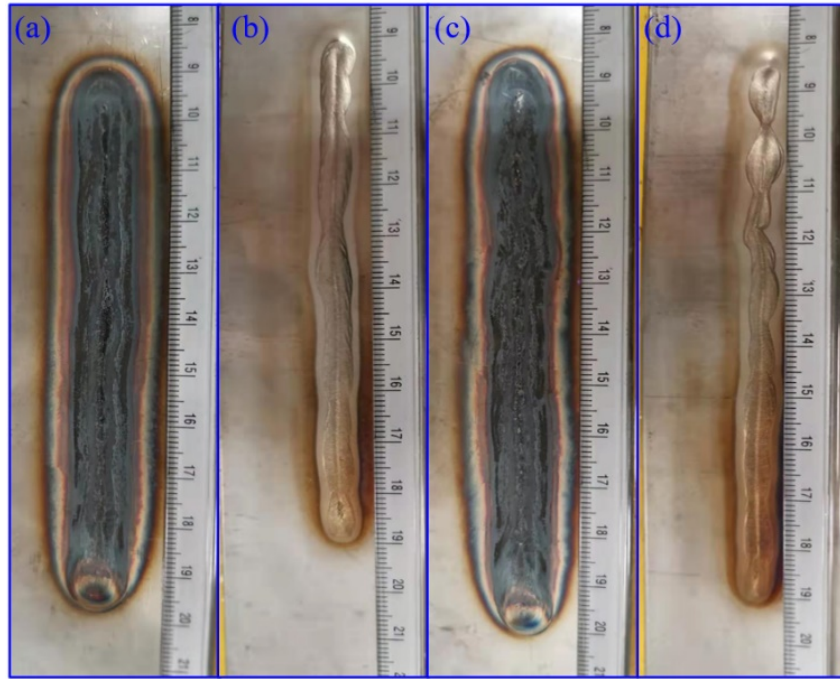


Figure 5.3 The Welded Workpieces from the Welders with Different Professional Levels. (a) and (b) Are the Front and Back Side from Skilled Welders and the Quality Is Satisfied; (c) and (d) Are the Front and Back Side from Unskilled Ones and the Quality is Unsatisfied.

Table 5.1 Welding and Workpieces Parameters

Parameters	Value
Welding method	GTAW
Welding type	DCEN
Welding current	150 A
Welding time	20 s
Tungsten diameter	2.4 mm
Tungsten grind	30 °
Shielded gas	Argon
Gas flow	5600 SCCM
Workpiece material	304L
Workpiece dimension	30×5×2 mm ³

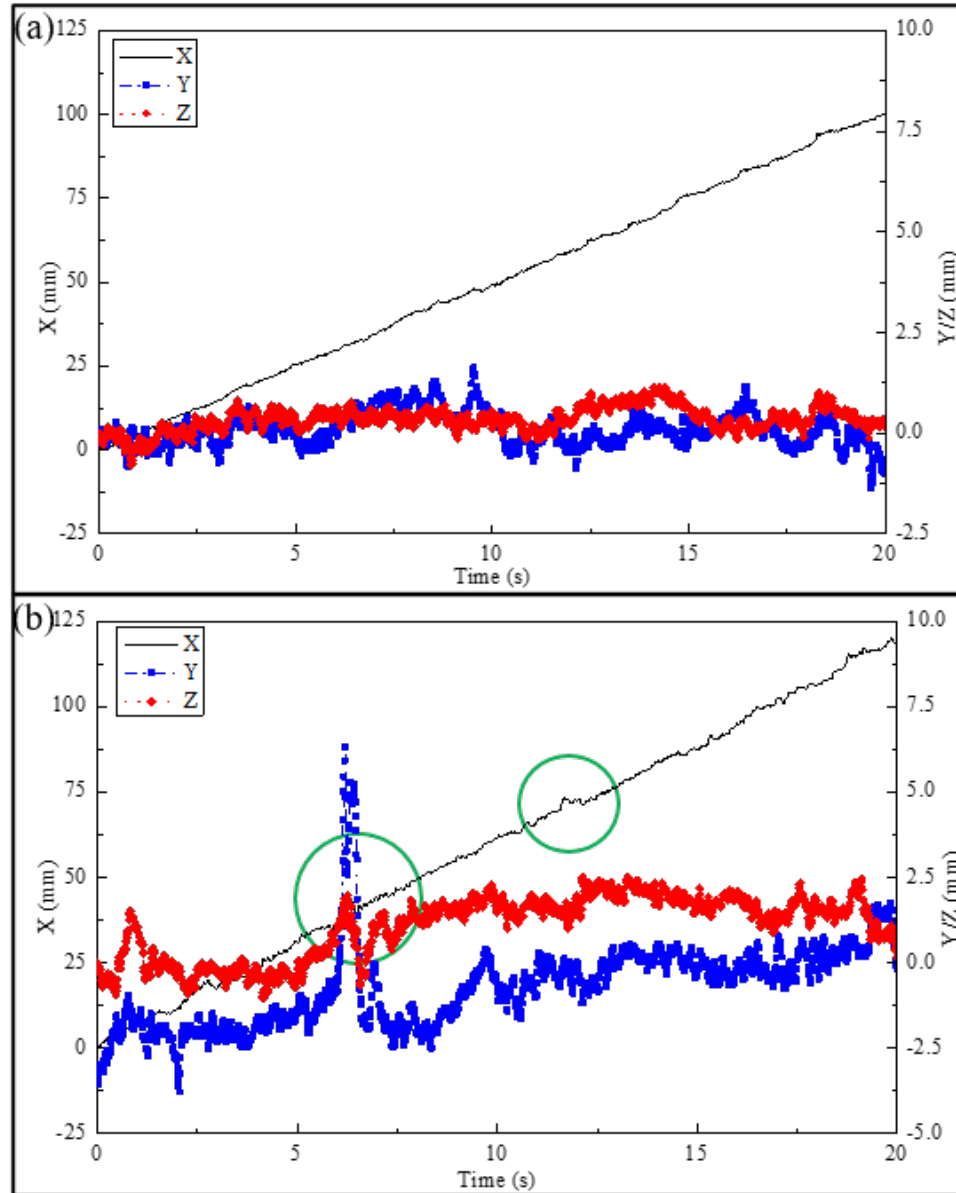


Figure 5.4 Facing the Same Welding Task, the Human Users with Different Professional Levels Demonstrate Different Welding Operations. X is the Welding Direction; Y is the Lateral Direction and Z is Vertical Direction; (a) from a Skilled Welder; (b) from an Unskilled Welder.

The difference in the resultant welding qualities comes from their demonstrated operations, which are downloaded from the cloud and shown in Figure 5.4. It can be found intuitively that welding operations demonstrated from the unskilled welders have larger fluctuation (circled in Figure 5.4) and larger instability in welding quality, compared with

the skilled welders. In order to verify the effectiveness of developed FFT-PCA-SVM in analyzing and classifying the welder behaviors from the demonstrated operations, their demonstrated operation data are processed in the next section.

5.4 Results and Discussions

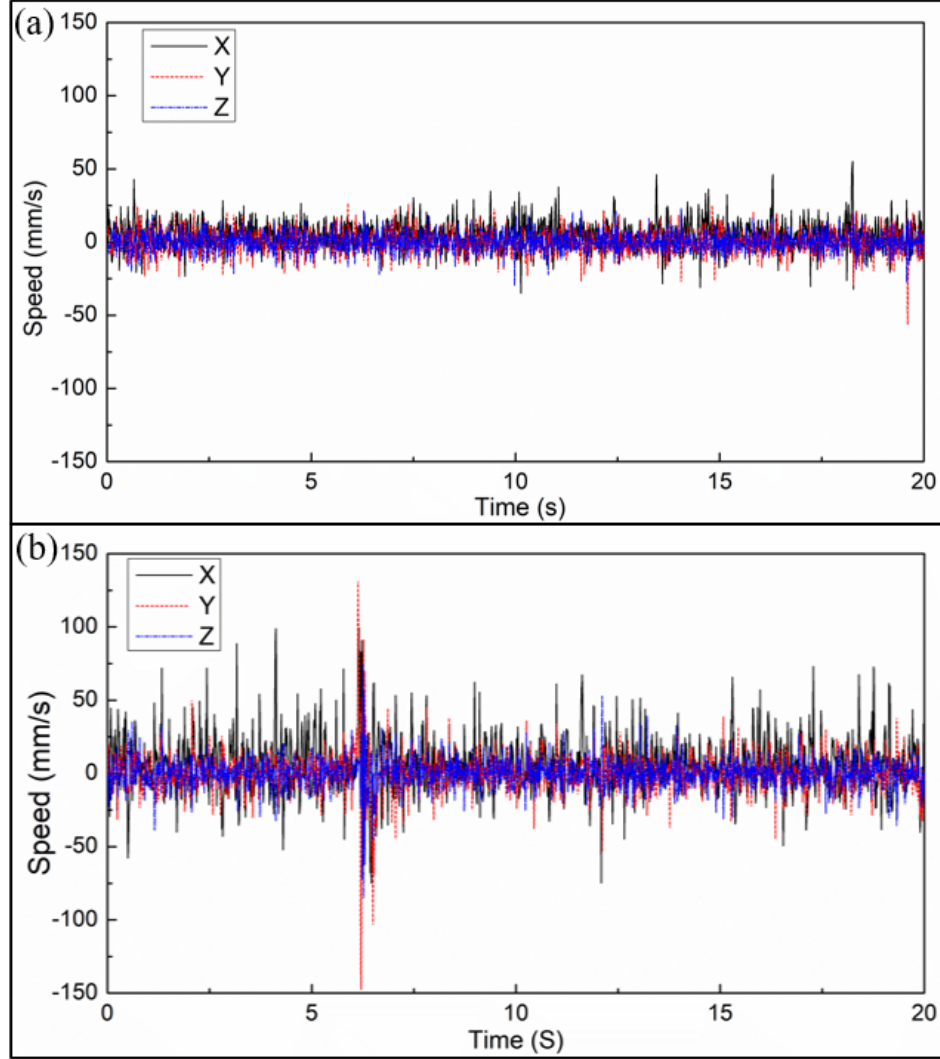


Figure 5.5 The Demonstrated Speed Sequences Computed from Position Sequences (a) from a Skilled Welder; (b) from an Unskilled Welder.

After each invited welder demonstrated 10 times for the same welding task, all the demonstrated data are downloaded from cloud. For each welder, one sequence is selected

randomly for constructing the testing dataset with other nine sequences kept for model training. The speed sequences are generated from Eq. (45). Figure 5.5 shows the generated sequences from Figure 5.4 and its length is 1800 which is the product of welding time and sampling frequency.

After downsampling, the sizes of training dataset and testing dataset are 1620 and 180, respectively. The frequency feature vector F is obtained using FFT and its unbalance is eliminated after normalization in Eq. (49). In data dimension reduction using PCA, the principal component number M is identified as $M = 24$ by the maximum-likelihood estimation method proposed by Minka [117]. Therefore, the normalized frequency feature dimension is reduced to 24 from 93.

The trade-off parameter λ is applied as 1 to train the SVMs using scikit-learn library [118] with the unskilled operations labeled as -1 and skilled ones labeled as 1. The 5-folder cross-validation is done with different kernel functions, including liner, 2-degree polynomial (poly-2), 3-degree polynomial (poly-3), 4-degree polynomial (poly-4), radial basis function (rbf) and hyperbolic tangent (tanh). By applying different kernel functions, the data is transformed into different transformed feature space and shows different linear separability, as shown Figure 5.6 and Table 5.2.

Figure 5.6 shows the distribution of the computed criterion $W \cdot \Phi(F^R) + b$. $W \cdot \Phi(F^R) + b = 0$ is the hyperplane for classification and the area $|W \cdot \Phi(F^R) + b| < 1$ is the separating gap. It can be found that there are two obvious clusters in the transformed feature space and the data shows good separability when the kernel functions are liner, rbf or tanh. Simultaneously, the validation accuracies from these models are quite satisfactory, over 90%. When the kernel functions are polynomials (poly-2, poly-3, and poly-4), there

are no obvious separate clusters, and the separability is worse though the classification accuracy is good in poly-3 case. In all these models, the SVM with rbf as kernel function gains the best cross validation performance where the prediction accuracy is 94.32%. Therefore, the rbf is applied as the kernel function to train the final SVM model and the testing performance is shown in Figure 5.7 and Table 5.3.

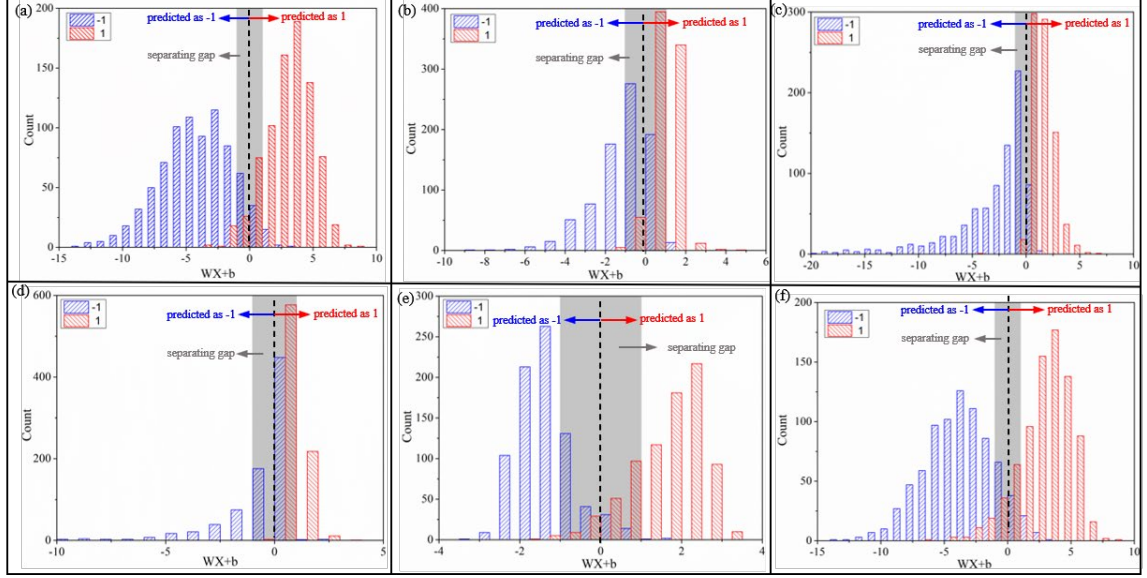


Figure 5.6 The Histogram of the Computed Criterion ($W \cdot \Phi(F^R) + b$) for Classification in 5-fold Cross Validation. (a) Liner; (b) Poly-2; (c) Poly-3; (4) Poly-4; (5) Rbf; (6) Tanh.

Table 5.2 5-Folder Cross Validation Performance with Different Kernels

Kernel function	Mathematics	Accuracy
linear	F_i^R, F_j^R	93.82%
poly-2	$(F_i^R, F_j^R)^2$	83.64%
poly-3	$(F_i^R, F_j^R)^3$	93.27%
poly-4	$(F_i^R, F_j^R)^4$	71.85%
rbf	$\exp(-\ F_i^R - F_j^R\ /(2\sigma^2))$	94.32%
tanh	$\tanh(\alpha \cdot F_i^R \cdot F_j^R)$	91.35%

From Figure 5.7, it can be found that most testing data points (150 of 180) locate beside the separating gap. They are shown as two separable clusters which is preferable for classification. Table 5.3 shows the confusion matrix of the prediction results, among

which 82 of 90 demonstrated operation sequences from the unskilled welders are predicted correctly and 88 of 90 demonstrated operation sequences from the skilled ones are predicted correctly. That makes sense since even unskilled welders can also demonstrate some good operation sequences like the skilled welders occasionally, but the probability for the skilled welders to demonstrate the non-professional operations is much lower. In total, the classification accuracy is 94.44% and verifies the effectiveness of the developed method to identify the profession level from their demonstrated operation.

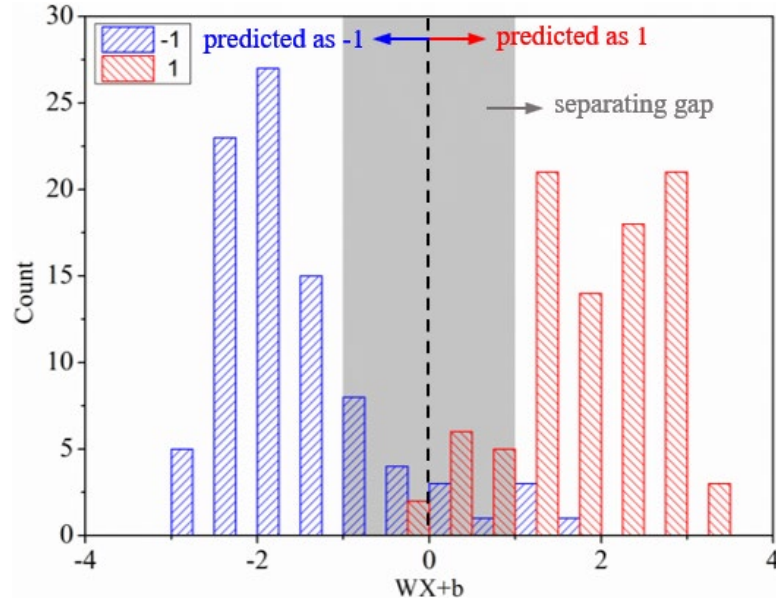


Figure 5.7 The Histogram of the Computed Criterion ($W \cdot \Phi(F^R) + b$) for Classification in Testing Data.

Table 5.3 Testing Confusion Matrix

		Actual	
		Unskilled	Skilled
Predicted	Unskilled	82	2
	Skilled	8	88

5.5 Summary

By integrating VR as an HRI interface, the developed digital twin owns the interactive ability with human users and is applied to welding manufacturing successfully. In such a digital twin, all the key elements in a physical world have their digital replicas and these replicas run with the same dynamics as the physical ones by the information communicating between the physical and digital worlds. Human welders with different professional levels (skilled and unskilled) can complete the same welding job successfully but demonstrate operations with different patterns. The FFT-PCA-SVM algorithm is developed for identifying the professional levels from the demonstrated data by transforming the speed sequences into frequency domain, reducing dimension, and classifying in transformed feature space. The final testing accuracy is 94.44% that verifies the effectiveness of developed method.

CHAPTER 6. ROBOT-ASSISTED WELDING

6.1 Introduction

Skilled welders can complete welding tasks well after several years' training and their shortage is faced all over the world. In comparison, the quantity of unskilled welders is very large. If we could develop robot-assisted welding to help unskilled welders to obtain qualified weld joints, the welder shortage problem can be released. In order to solve this problem, we modify the developed digital twin for human-robot interactive welding to complete robot-assisted manual welding by recognizing human intention.

Understanding and recognizing human intention is the foundation to correct possible operation errors from commanding human to effectively operate robots to perform for the human [119]. Linear dynamic models including state models and Kalman filtering have been proposed to model human intention and been applied to power-assisted rehabilitation robots [120]. In order to characterize the nonlinearity in human intention/action, non-linear models including neural networks (NNs) and support vector machines (SVMs) have also been proposed to recognize human intention for applications such as limb trajectory tracking for robots [121][122]. However, such deterministic models, linear or nonlinear, cannot characterize the innate randomness of human actions. To cope with this issue, some researchers have proposed to use hidden Markov models (HMMs) [123] or layered hidden Markov models (LHMMs) [124] which contain multiple levels of HMM to recognize human intention. Two kinds of ideas have been proposed: (1) when the human intention is defined as a task, each task is characterized as an HMM. Then, the human intention recognition problem is equivalent to the probability computation of certain sequences with the appropriate HMM [123]; (2) when the human

intention is defined as a subtask, it is usually taken as the hidden state and an entire human action sequence is modeled as an HMM. Then, the human intention recognition problem can be stated as the hidden state estimation [125]. Both of these problems can be solved using the forward-backward algorithm [126].

The proposed human intention recognition component in our work has some similarity to previous work but also some new aspects. In our application, human intention is defined as the intended human hand motion. In an ideal manual welding process, welding torch moves in accordance with the human intended movement. Due to natural and inevitable vibrations of human hands, it is hard or even impossible at all for human to control welding torch as intended, especially for novice welders. Human hand stability training is typically an important part of welder training. We use the HMM based concept of state occupancy probability to model instable randomness and apply an HMM-based method to recognize human intention, using human hand movement speed as observable variables. For our proposed method, the welding tasks cannot be decomposed of subtasks in advance. Thus, the hidden state number cannot be pre-identified. To address this problem, we propose to use the Bayesian information criterion (BIC) to identify the optimal number of hidden states in the HMMs. Training the HMM using the Baum-Welch algorithm, the hidden state occupancy probability distribution is then estimated using the forward algorithm. The robot executes intended actions determined from the statistical expectation of observable variables.

6.2 Principles of HMMs

HMMs are statistical models for sequential data where the latent state sequence is a Markov chain whose value determines the distribution of the corresponding observable

variables. As shown in Figure 6.1, $Z = \{z_1, z_2, z_3, \dots, z_M\}$ is the set containing all possible state values z_i and M is the total number of possible hidden states. The instantaneous latent state s transits among Z with some probability $P(s_n | s_{n-1})$ characterized as the state transition matrix $A_{M \times M}$ where $A_{ij} \equiv P(s_n = z_j | s_{n-1} = z_i)$. With each state, the observation variable o has an emission probability distribution $P(o | z_i)$ characterized as Φ . The initial state probability vector $\kappa = [\kappa_1, \kappa_2, \dots, \kappa_M]^T$, where $\kappa_i = P(s_1 = z_i)$, is HMM's initial state distribution. Then, an HMM is determined by the three-parameter set $\theta = \{\kappa, A, \Phi\}$ completely. In our HMM, human hand movement speed $v = [v_x, v_y, v_z]^T$ is observable variable and Φ is assumed to be Gaussian distribution:

$$P(o|z_i) = \frac{1}{2\pi|\Sigma_i|} \exp\left(-\frac{1}{2}(o - \mu_i)^T \Sigma_i^{-1}(o - \mu_i)\right) \quad (55)$$

where μ_i is the mean value of the speed and Σ_i is covariance matrix. With expanding in time domain, both latent state sequence S and observable variable sequence O are formed.

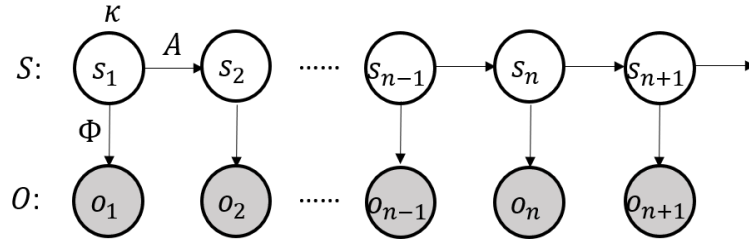


Figure 6.1 Schematic Diagram for HMM.

6.3 Model Identification

6.3.1 Principles of Baum-Welch Algorithm

As discussed previously, only the observation o is observable in our application while the latent state is unobservable. The Baum-Welch algorithm is applied to estimate

the parameters of HMMs by finding the model parameters set θ maximizing the sum of log of the likelihood function of all observance sequences:

$$\hat{\theta} = \operatorname{argmax}_{\theta} \left(\sum_O \log(O|\theta) \right) \quad (56)$$

where O is a single sequence. Then the parameters can be identified by finishing iterative expectation step (E step) and maximization step (M step) in two steps:

(1) E step: Find the Q function:

$$Q(\theta, \theta^{old}) = \sum_O \sum_S (P(S|O, \theta^{old}) \log(P(O, S|\theta))) \quad (57)$$

From the properties of HMMs, $P(O, S | \theta)$ can be computed:

$$P(O, S|\theta) = P(s_1|\kappa) \left(\prod_{n=2}^{N_T} P(s_n|s_{n-1}, A) \right) \prod_{n=1}^{N_T} P(o_n|s_n, \Phi) \quad (58)$$

where N_T is length of state sequence S and observable variable sequence O .

After substituting Eq. (58) into Eq. (57), Q is separated into three parts: initial part Q_I , transition part Q_T and emission part Q_E :

$$Q(\theta, \theta^{old}) = \sum_O (Q_I + Q_T + Q_E) \quad (59)$$

$$Q_I = \sum_{i=1}^M (\gamma(s_1^i) \log(\pi_i)) \quad (60)$$

$$Q_E = \sum_{n=1}^{N_T} \sum_{i=1}^M (\gamma(s_n^i) \log(P(o_n|\Phi_i))) \quad (61)$$

where:

$$\gamma(s_n^i) = P(s_n = z_i | O, \theta^{old}) \quad (62)$$

$$\xi(s_{n-1}^i, s_n^j) = P(s_{n-1} = z_i, s_n = z_j | O, \theta^{old}) \quad (63)$$

2) M step: Maximize the $Q(\theta, \theta^{old})$ with respect to θ :

Since Q is a continuous function of θ , its value is maximized when the partial derivative of Q with respect to θ is 0:

$$\frac{\partial Q(\theta, \theta^{old})}{\partial \theta} = 0 \Leftrightarrow \begin{cases} \frac{\partial Q(\theta, \theta^{old})}{\partial \kappa_i} = 0 \\ \frac{\partial Q(\theta, \theta^{old})}{\partial A_{ij}} = 0 \\ \frac{\partial Q(\theta, \theta^{old})}{\partial \mu_i} = 0 \\ \frac{\partial Q(\theta, \theta^{old})}{\partial \Sigma_i} = 0 \end{cases} \quad (64)$$

The iterative learning algorithm for the HMMs can be given as:

$$\theta = \begin{cases} \kappa_i = \frac{\sum_o \gamma(s_1^i)}{\sum_o \sum_{i=1}^M \gamma(s_1^i)} \\ A_{ij} = \frac{\sum_o \sum_{n=2}^{N_T} (\xi(s_{n-1}^i, s_n^j))}{\sum_o \sum_{k=1}^M \sum_{n=2}^{N_T} (\xi(s_{n-1}^i, s_n^k))} \\ \mu_i = \frac{\sum_o \sum_{n=1}^{N_T} (\gamma(s_n^i) \cdot o_n)}{\sum_o \sum_{n=1}^{N_T} \gamma(s_n^i)} \\ \Sigma_i = \frac{\sum_o \sum_{n=1}^{N_T} (\gamma(s_n^i) \cdot (o_n - \mu_i)(o_n - \mu_i)^T)}{\sum_T \sum_{n=1}^{N_T} \gamma(s_n^i)} \end{cases} \quad (65)$$

Additionally, the unknown variables γ and ξ can be computed using the forward-backward algorithm:

The forward probability α_n^i and the backward probability β_n^i are defined as

$$\alpha_n^i \equiv P(o_1, o_2, \dots, o_n, s_n = z_i) \quad (66)$$

$$\beta_n^i \equiv P(o_{n+1}, o_{n+2}, \dots, o_{N_T} | s_n = z_i) \quad (67)$$

where both α_n^i and β_n^i can be computed using the dynamic programming (DP) algorithm:

$$\begin{cases} \alpha_1^i = \kappa_i P(o_1|z_i) \\ \alpha_{n+1}^i = (\sum_{j=1}^M (\alpha_{n+1}^i A_{ji})) P(o_{n+1}|z_i) \end{cases} \quad (68)$$

$$\begin{cases} \beta_{N_T}^i = 1 \\ \beta_{n-1}^i = \sum_{j=1}^M (A_{ij} \beta_n^i P(o_n|z_j)) \end{cases} \quad (69)$$

Following this, both γ and ξ can be computed explicitly:

$$\gamma(s_n^i) = P(s_n = z_i | O, \theta^{old}) = \frac{P(s_n = z_i, O | \theta^{old})}{P(O | \theta^{old})} = \frac{\alpha_n^i \beta_n^i}{\sum_{i=1}^M \alpha_{N_T}^i} \quad (70)$$

$$\begin{aligned} \xi(s_{n-1}^i, s_n^j) &= P(s_{n-1} = z_i, s_n = z_j | O, \theta^{old}) = \\ &= \frac{P(s_{n-1} = z_i, s_n = z_j, O | \theta^{old})}{P(O | \theta^{old})} = \frac{\alpha_{n-1}^i A_{ij} P(o_n | z_i) \beta_n^j}{\sum_{i=1}^M \alpha_{N_T}^i} \end{aligned} \quad (71)$$

Together these algorithms allowing estimation of all the variables needed to identify the parameters of the HMMs have been derived explicitly.

6.3.2 Data Collection

Table 6.1 Welding Parameters Applied

Welding Parameters	Value
Peak Current (A)	160
Base Current (A)	40
Pulse Frequency (Hz)	1
Duty Cycle	50%
Initial Arc Length (mm)	5
Tungsten Diameter (mm)	2.4
Tungsten Grind Angle (°)	30
Shielded Gas	Argon
Gas Flow (SCCM)	4700
Workpiece Material	DH36

The experimental task consists of a user using motion-tracked handles to implement a pulse backing welding task 8 separate times, generating 8 training sequences. The applied welding parameters are shown in Table 6.1. The position of the human hand is sensed with a sampling frequency of 10Hz. Hand speed is determined based on the position data. In total, 8 observable variable sequences with 6585 data points are used to train models.

6.3.3 Identification of Hidden State Number

As discussed in before, unlike previous methods for modeling human actions using HMMs, the number of hidden states cannot be identified in advance. Therefore, the Bayesian information criterion (BIC) is used to identify the best number of hidden states. For HMMs, the BIC can be computed as:

$$BIC = -2 \cdot \log(L) + k \cdot \log(n) \quad (72)$$

where the L is maximized value of the likelihood of observable data with the model:

$$L = \max_{\theta} (\prod_o P(O|\theta)) = \max_{\theta} (\prod_o (\sum_{i=1}^M \alpha_{N_T}^i)) \quad (73)$$

k is the number of independent parameters learned in HMMs and n is the total number of data points, 6585 in our application.

For our application, the emission probability is assumed to have a Gaussian distribution and k is the sum of the learned number of the four independent parameters:

$$k = k_k + k_A + k_{\mu} + k_{\Sigma} \quad (74)$$

$$k_k = M - 1 \quad (75)$$

$$k_A = M \cdot (M - 1) \quad (76)$$

$$k_{\mu} = d \cdot M \quad (77)$$

$$k_{\Sigma} = d \cdot (d + 1) \cdot \frac{M}{2} \quad (78)$$

where M is the number of hidden states and d is the data feature dimension. In our application, $o = v = [v_x, v_y, v_z]^T$ which is the hand movement speed and therefore $d = 3$.

Thus:

$$k = M^2 + 9M - 1 \quad (79)$$

Using the Baum-Welch algorithm, the HMMs are trained with fully random initial model parameters. In order to decrease the effect of randomly choosing initial model parameters, models with the same number of hidden states are trained 10 times. Finally, the number of hidden states is identified as 5 by computing and comparing scores and BIC for each model. These results are shown in Figure 6.2. The score of each model is defined as the log of likelihood of observable data:

$$score = \log \left(\prod_o P(O|\theta) \right) = \sum_o \left(\log \left(\sum_{i=1}^M \alpha_{N_T}^i \right) \right) \quad (80)$$

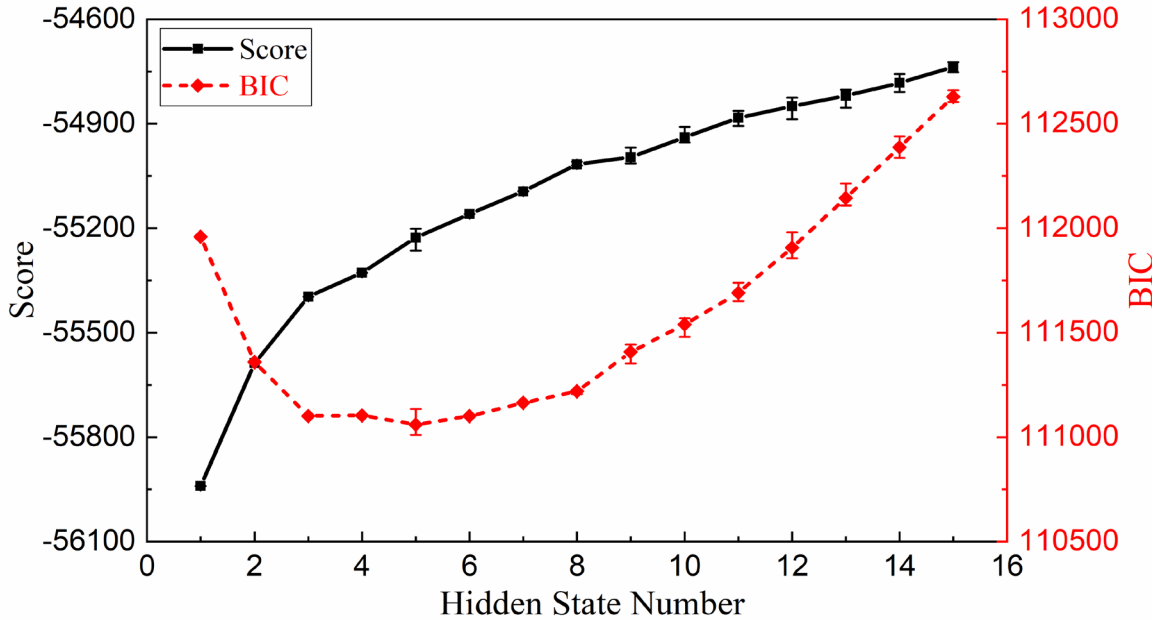


Figure 6.2 Model Evaluation with Different Number of States.

6.3.4 Model Training

Taking the number of hidden states as 5, the HMM training is repeated 10 times with initial parameters chosen randomly. The one with highest score is chosen as the final model. The iterative process is shown in Figure 6.3. The convergence rate is defined as the difference of the log likelihood of observable sequences compared with the last iteration. It can be found that model converges after ~ 100 iterations.

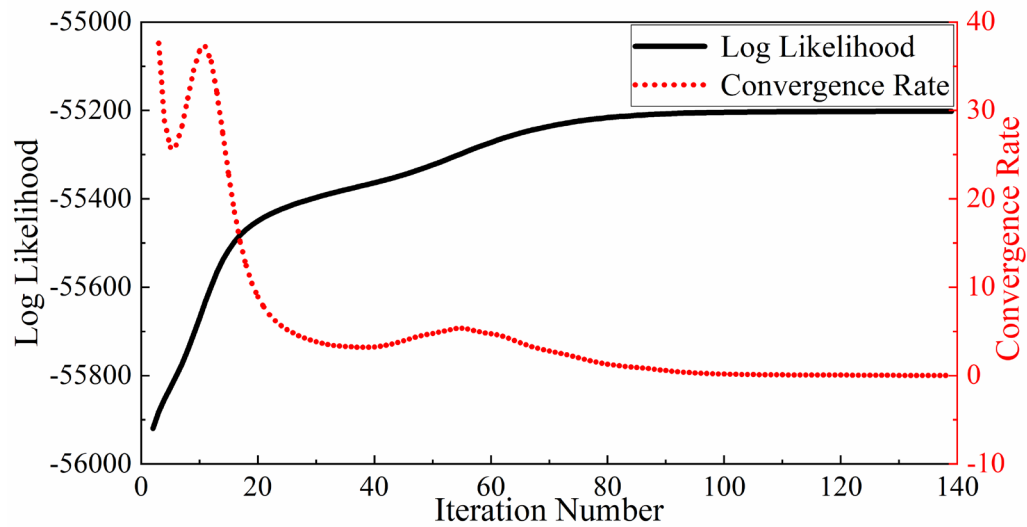


Figure 6.3 Convergence in Model Training.

6.4 Human Intention Recognition

6.4.1 Principles

Unintentional actions exist in the operation/demonstration of commanding humans because of physical limitation that reduces the controllability and the lack of the needed degree of skills. The robot should thus execute the intended operations recognized. The waveform of the welding current is not easy to adjust in real-time by human as the

tool/torch. Hence, in our case, the former is pre-determined and fixed, and the latter is real-time adjusted as in manually operated welding process.

We define human intention as the intended hand speed \bar{v} . The problem can thus be stated as that of estimating the current/present intended movement speed \bar{v}_n from the raw moving speed sequence. This problem can be addressed in two steps:

(1) State occupancy probability computation:

The state occupancy probability vector ζ_n characterizes the probability of occurrence of each hidden state z_i at given time:

$$\zeta_n = [\zeta_n^1, \zeta_n^2, \dots, \zeta_n^M]^T \quad (81)$$

$$\zeta_n^i \equiv P(s_n = z_i | o_1, o_2, \dots, o_n) \quad (82)$$

Here, each hidden state z_i is considered as a “base state” and the state at any time s_n is estimated as the probability weighted mixture of base state z_i . The probability vector ζ_n can be computed based on the forward algorithm:

$$\zeta_n^i = \frac{P(s_n = z_i, z_1, z_2, \dots, z_n)}{P(o_1, o_2, \dots, o_n)} = \frac{\alpha_n^i}{\sum_{i=1}^M \alpha_n^i} \quad (83)$$

(2) Intended movement estimation:

For each hidden state z_i , the u_i is considered as its intended movement. The intended movement at each time is estimated as the statistical expectation of current observable variable based on state occupancy probability vector ζ_n :

$$\bar{v}_n = \sum_{i=1}^M (\zeta_n^i \cdot \mu_i) \quad (84)$$

6.4.2 Testing Verification

Another movement sequence is generated by the same person with the same experimental configuration, to test the effectiveness of the proposed human intention

algorithm. The recognized intended speed results and its statistical information are shown in Figure 6.4 and Table 6.2. From Figure 6.4 and Table 6.2, it can be found that the intended movement estimated using the HMM approach is much smoother, with significantly lower standard deviation and near-zero means in the y and z directions. Smoother movement is more preferred for welding: with consistent motion in the direction of travel and little or no motion in lateral and vertical directions. As can be seen, in the primary direction of travel along the x-axis, the recognized intended travel speed achieves a mean close to the true one and a decreased standard deviation. In the lateral y-axis and vertical z-axis direction, a near-zero mean and decreased standard deviation are also achieved.

Table 6.2 Statistical Information for Testing Experiments

Speed		Statistical Information (mm/s)	
		Mean	Standard Deviation
X	Raw	2.53	5.03
	Intended	2.54	1.51
Y	Raw	0.022	3.17
	Intended	-0.001	0.92
Z	Raw	0.061	5.08
	Intended	0.010	0.30

An interesting phenomenon happens in the z-direction. The raw speed data has the largest variance, but the intended speed data has the smallest variance. This indicates that the z-direction movement has the highest degree of randomness, i.e., there is no obvious intention transition for human in z-direction movement compared with other two directions. That makes sense since the x-direction is the primary welding direction, for which the human operator has a clear intended travel speed, and the y-direction is the weld seam position where the operator intends to track. The z-direction is the vertical direction

where there is no strict regulation for the operator as long as the continuity of the welding process is maintained. Furthermore, the vertical movement is much harder to control than horizontal movement for human due to internal muscle structure.

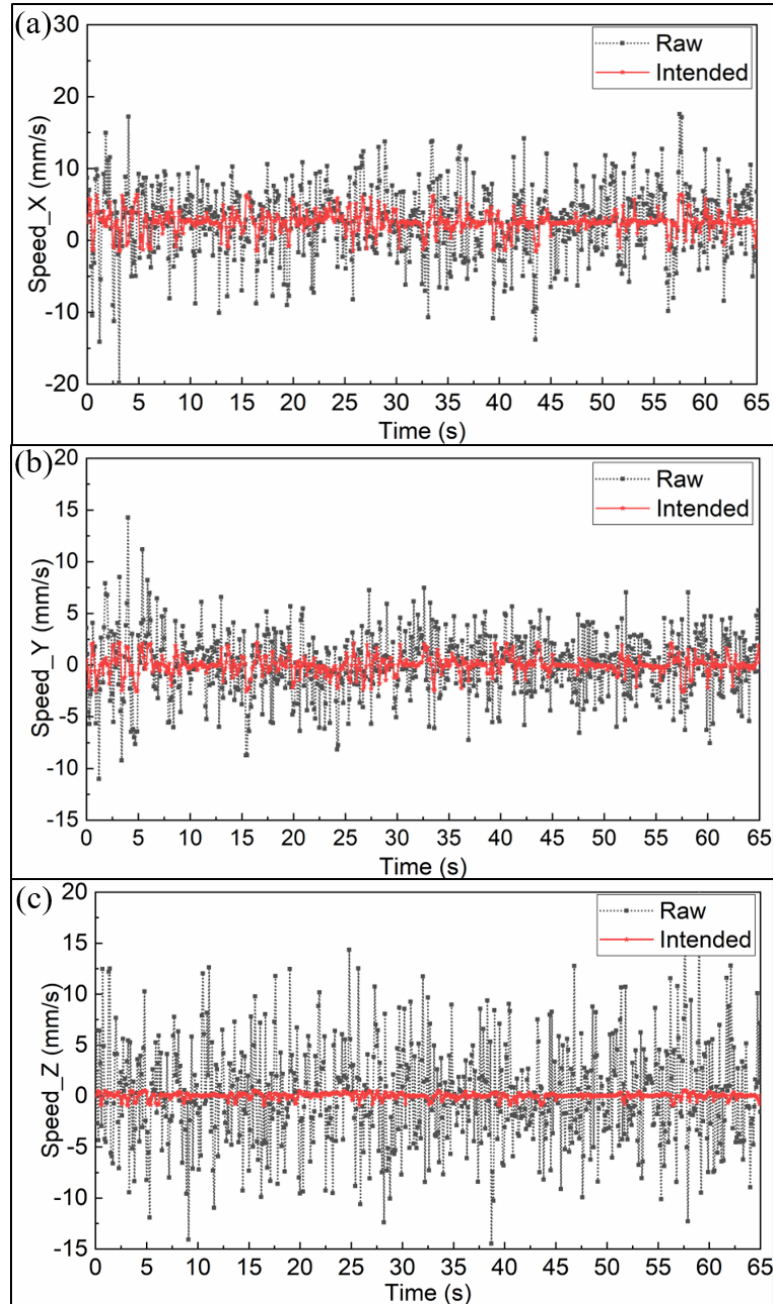


Figure 6.4 Human Intention Recognition Result (a) x-direction Which the Welding Torch Moves Along; (b) y-direction Where Welding Torch Deviates from Weld Seam; (c) z-direction Which is Vertical.

6.5 Robot-Assisted Welding Experiment

The trajectories of the robot with and without using proposed human intention recognition algorithm are shown in Figure 6.5. The corresponding welded workpieces using the same welding parameters in Table 6.1 are shown in Figure 6.6. Based on the human operator movement and weld bead appearance, the welding operation can be separated into 5 stages: I (0-20s); II (20-40s); III (40-48s); IV (48-57.5s) and V (57.5-65s).

In stage I, the welding process is relative steady, there is not a big difference between the raw movement and the intended movement such that the corresponding weld bead appearances are similar. In stage II, the position of the tungsten electrode deviates from and returns to the weld seam, with a maximum seam deviation of ~8 mm. This causes the heat from the arc to the workpiece to deviate from weld seam. This deviation results in a critical welding failure (incomplete weld). The seam deviation comes from the accumulation of the negative speed in the lateral y-axis at 21-27 s. This can be considered as an unintended operation fault by the operator. When the operator realizes this problem via the HMD, he/she tries to correct by adjusting the position of the welding torch to track the weld seam again (27-40 s). When using the intended operation recognized from the proposed HMM-based human intention recognition algorithm, the sharp change of operation speed in the y-axis during stage II is suppressed. The maximum seam deviation is reduced to ~2.5 mm which still results in the incomplete penetration defect, but the degree of harm has been decreased and the incomplete penetration is often acceptable except for critical cases.

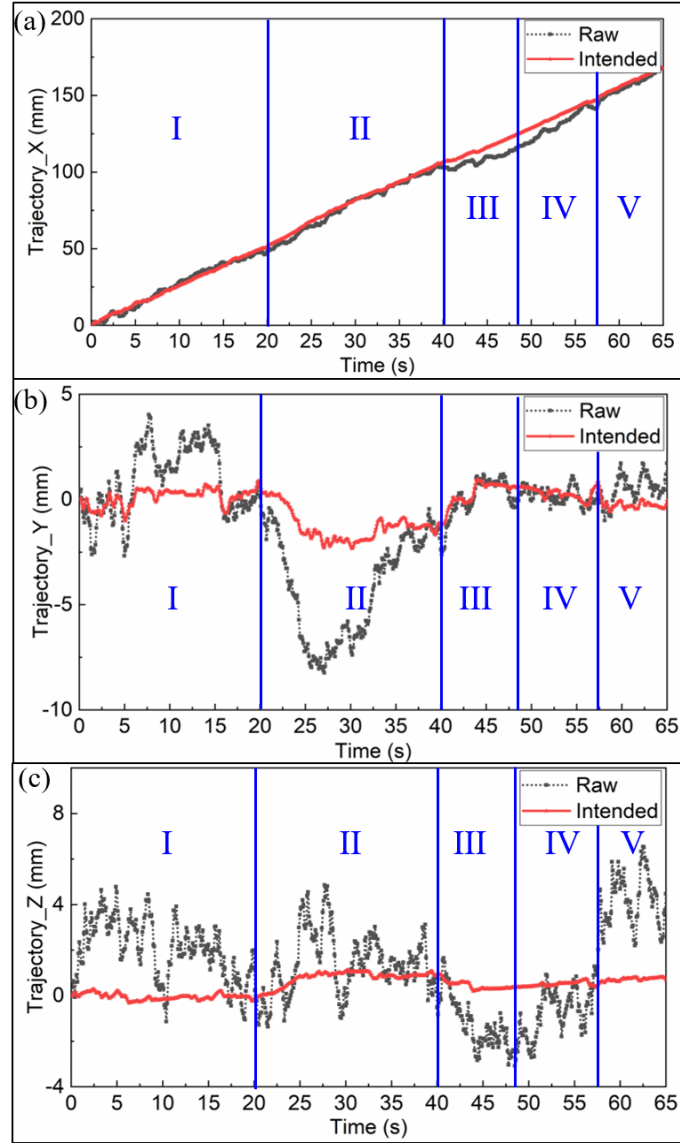


Figure 6.5 Robot Trajectory (a) x-direction; (b) y-direction; (c) z-direction.

In stage III, the travel speed along the x-axis is too low resulting in high total energy input and eventual burn-through welding failure. The opposite problem occurs in stage IV, with high travel speed resulting in low total energy input and incomplete penetration. Using the proposed algorithm, the variance in travel speed is much lower and both the stage III low-speed and stage IV high-speed welding faults are eliminated.

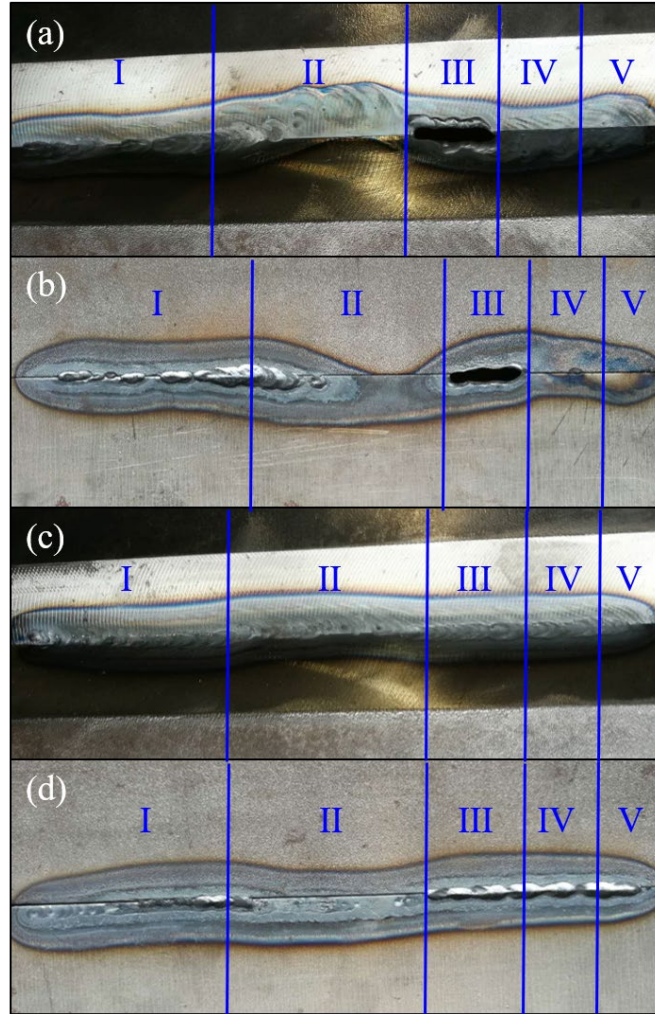


Figure 6.6 Welded Workpieces (a) Front Side without Human Intention Recognition; (b) Back Side without Human Intention Recognition; (c) Front Side with Human Intention Recognition; (d) Back Side with Human Intention Recognition.

In stage V, the trajectory of the tungsten electrode along the vertical z-axis vibrates above the desired center position resulting in a longer arc than desired, with a maximum arc length of ~12 mm compared with initial arc length of 5 mm. As shown in Figure 6.7, this causes a strong divergence of the arc in the workpiece. The arc heat to workpiece spreads so much that the energy density is insufficient for full fusion of base metal, causing an incomplete penetration defect. After using the proposed algorithm, the variation above

the desired z-axis position is suppressed and the maximum arc length is maintained at ~6 mm and not creating a welding fault.

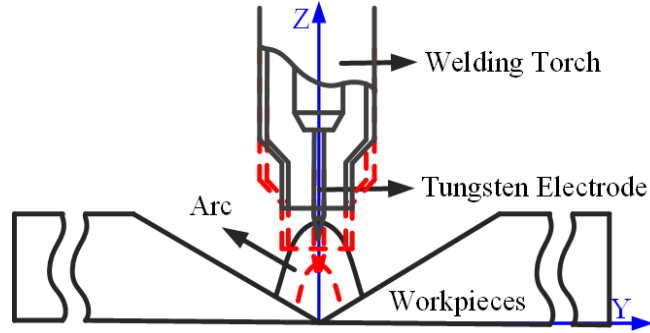


Figure 6.7 Schematic Diagram of Arc Shape with the Vertical Movement of Welding Torch. Red Dash: Original Shape. Black Solid: Arc Diverges with Arc Lengthening.

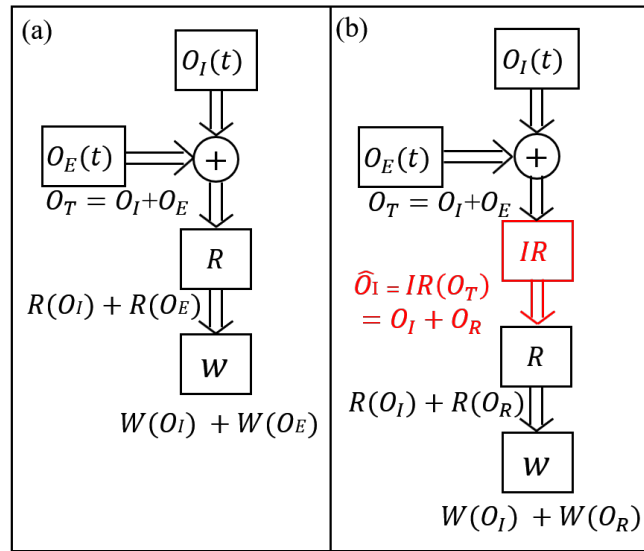


Figure 6.8 Principle of Robot-assisted Manual Welding (a) Without Human Intention Recognition; (2) With Human Intention Recognition.

Figure 6.8 illustrates how the human intention recognition (IR) helps improve the performance. The raw human operation O_T includes the intended operation O_I and erroneous one O_E . Without the intention recognition, the robot (modeled as R) manipulates the movement of the welding torch by copying O_T . Both O_I and O_E effect the welding

(modeled as W) to produce $W(O_I)$ and $W(O_E)$ where the former is desired, but the latter is not. After adding the human intention recognition component IR as shown in Figure 6.12(b), the recognized intended operation \hat{O}_I contains O_I and residual part O_R :

$$\hat{O}_I = O_I + O_R \quad (85)$$

Via the same robot and welding system as modeled by R and W , the final welding results are now controlled by O_I and O_R . The goal of this work for human intention recognition is to minimize O_R such that $O_R \ll O_E$. In our welding experiments without human intention recognition, the generated weld faults (such as incomplete weld and burn-through) can be considered as $W(O_E)$ due to human erroneous operations. After using the proposed human intention recognition algorithm, the remaining weld defects (such as incomplete penetration) are due to O_R . For an effective human intention recognition algorithm such that $O_R \ll O_E$, $W(O_R)$ must be much smaller than $W(O_E)$ as R and W are unchanged.

6.6 Summary

This chapter endows the human intention recognition abilities to the robots in developed digital twin for human-robot interactive welding based on HMM. As such, the role of the robots transits from the puppets i.e. copying the human welder operations to the assistants who are with a certain intelligence. Then, the intended movement with untended operations eliminated. This approach helps to improve the weld quality generated from welders and verified by experiments.

CHAPTER 7. HUMAN-ROBOT COLLABORATIVE WELDING

7.1 Introduction

As talked before, current welding robots have their limitations in adaptive decision-making when faced environment disturbance. However, welding robots have higher movement precision, stability, and fewer physical limitations due to the environmental hazards of vacuum, pressure, temperature, radiation, poison, and fatigue compared with humans. Several welding methods including spot welding, stud welding, arc welding, and laser welding, have been successfully robotized to increase production efficiency [127]. In this chapter, we modify the developed digital twin for human-robot interactive welding further and aims to combine the advantages from humans and robots by human-robot collaborative welding. The weaving gas tungsten arc welding is investigated as a case study where V-gaped workpieces whose geometrical cross profile is shown in Figure 7.1 are welded using the parameters in Table 7.1.

Table 7.1 Welding and Camera Parameters Applied

Welding Parameters	Value	Configuration	Value
Welding Type	DCEN	Filter Center (nm)	650±2
Welding Current (A)	140-180	Filter FWHM (nm)	10±2
Tungsten Diameter (mm)	2.4	Image Size (Pixel)	640×480
Tungsten Grind Angle (°)	30	Format	Mono8
Shielded Gas	Argon	Frame Rates (FPS)	30
Gas Flow (SCCM)	5600	Shutter Time (s)	0.03
Workpiece Material	DH36	Sharpness	3000
Swing Type	Sinusoid	Gain	0
Swing Amplitude (mm)	2	Gamma	2.5
Swing Period (s)	2	-	-

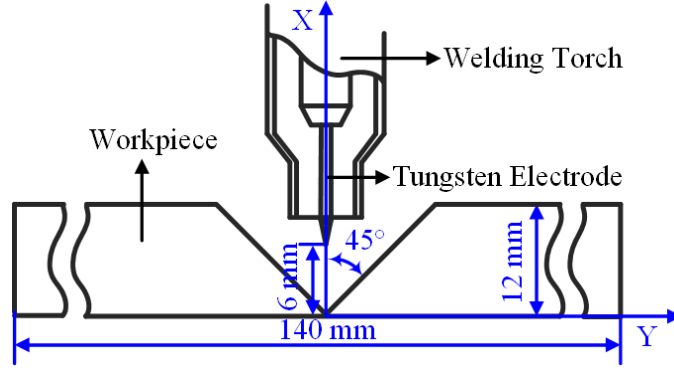


Figure 7.1 Geometrical Cross Profile of Welded Workpiece.

7.2 Principles

7.2.1 Cyber-Physical Model

Compared with the general digital twin model shown in Figure 4.3, a local close-loop circuit is added aiming for automatic weaving and seam tracking. In such a close-loop circuit, the electrical information I_E^W includes arc voltage and welding current is sensed by the arc sensor. The position difference between the tungsten electrode and weld seam Δd is computed and the robot adjusts the swing center to track the weld seam. By doing this, the robot is responsible for the automatic seam weaving and seam tracking. The human welders are responsible for intelligent welding parameter adjustment. By using this framework, the advantages from humans (intelligence) and robots (accurate movement and rapid response) are combined and the labor burden for humans is also reduced.

operator observes the augmented welding scene and adjusts the movement along the weld seam.

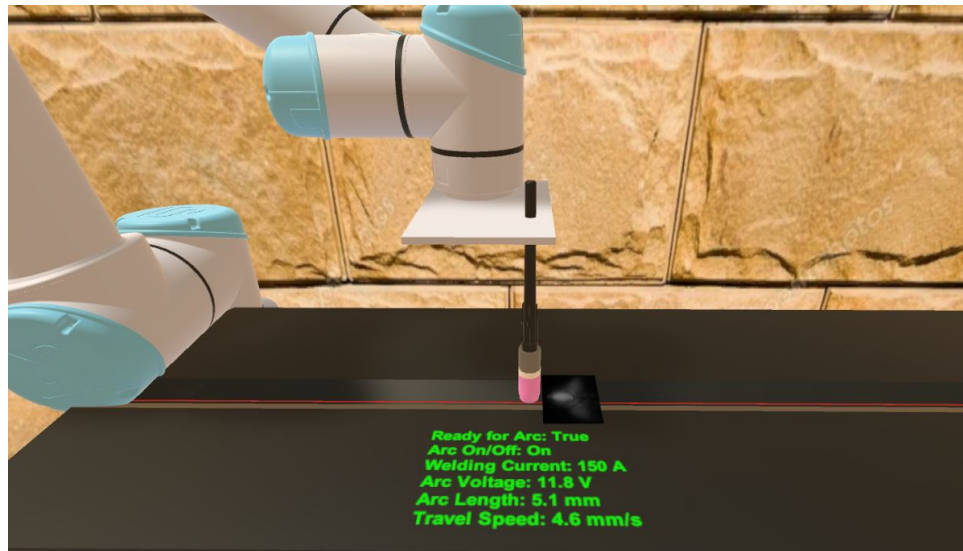


Figure 7.3 A typical Working Scene Shown to Human by HMD.

7.2.3 Robotic Weaving and Seam tracking

The welding torch weaving and automatic seam tracking are done by the robots. The weaving movement has sinusoid trajectory with pre-defined weaving center and amplitude and is done with robot pre-programmed. The automatic seam tracking is developed based on the principle that arc voltage depends on arc length and welding current. Therefore, the first task is to model the mapping function $U = U(L, I)$ where U is arc voltage, I is the welding current and L is the arc length. Using the welding parameter in Table 7.1, weaving welding is conducted and welding current, arc length and arc voltage data is collected. The diagrams of arc voltage varying with welding current and arc length are shown in Figure 7.4 and Figure 7.5, respectively. It can be inferred that both welding current and arc length affect arc voltage linearly with the other factor fixed. Therefore, we have:

$$\frac{\partial U(L, I)}{\partial L} = f(I) \quad (86)$$

$$\frac{\partial U(L, I)}{\partial I} = g(L) \quad (87)$$

From (86) and (87), it can be derived:

$$\frac{\partial^2 U(L, I)}{\partial L \partial I} = \frac{df(I)}{dI} = \frac{dg(L)}{dL} = \text{Contant} \quad (88)$$

The general solution for Eq. (88) is:

$$U(I, L) = k_0 IL + k_1 I + k_2 L + k_3 \quad (89)$$

The unknown parameters in Eq. (89) are identified using least squares whose fitting results and curve are shown in Table 7.2 and Figure 7.6. From the fitting results, the $R^2 = 0.9265$ which is close to 1 and p -value is 0 which is much smaller than the default significance level of 0.05 used commonly in engineering. Therefore, the proposed model has statistical significance which verifies the validity of hypothesis among arc voltage, welding current and arc length.

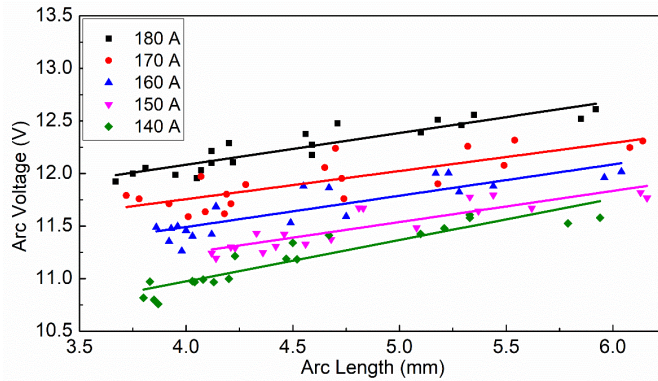


Figure 7.4 Arc Length Determines Arc Voltage Linearly.

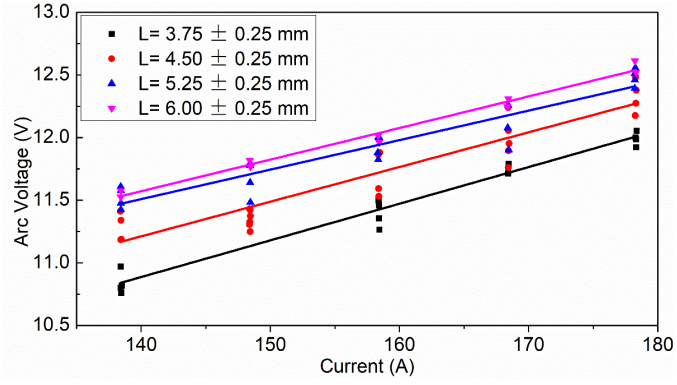


Figure 7.5 Welding Current Determines Arc Voltage Linearly.

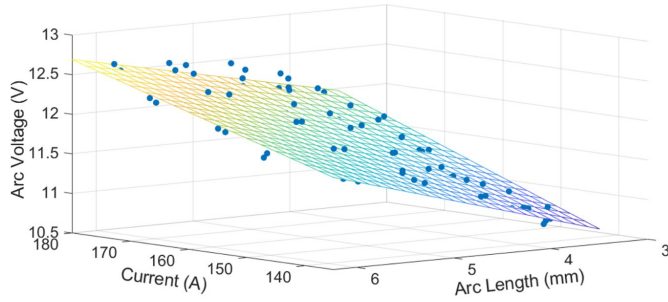


Figure 7.6 Fitting Curve of $U = U(L, I)$.

Table 7.2 Fitting Result of $U = U(L, I)$

Parameters	Value
k_0	-0.002 Ω/mm
k_1	0.0359 Ω
k_2	0.641 V/mm
k_3	4.591 V
R^2	0.9265
F-statistic	403.2865
p -value	0

As shown in Figure 7.7, the relative position of weaving center to weld seam determines the arc length distribution during swing welding, and the relative deviation between them Δd can be computed by the arc length difference ΔL at swing boundary position and further computed by arc voltage difference ΔU :

$$\Delta d = \frac{1}{2\tan\theta} \Delta L = \frac{1}{2\tan\theta} \cdot \frac{\Delta U}{k_0 I + k_2} \quad (90)$$

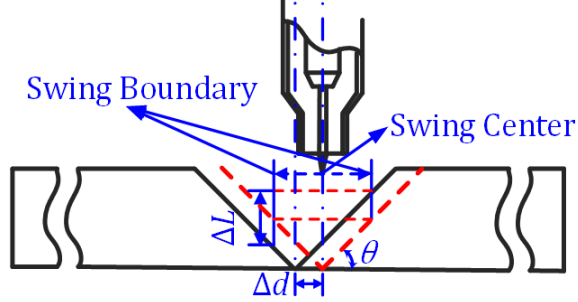


Figure 7.7 Swing Center Deviation from Weld Seam Results in Asymmetric Arc Length Distribution.

By Eq. (90), the tungsten electrode deviation Δd can be identified by arc voltage and welding current directly which are both available from arc sensors. Then, the automatic seam tracking algorithm is developed whose working flowchart is shown in Figure 7.8. In each swing cycle, the boundary position in weaving direction (y-axis in our application), Y_{max} and Y_{min} are found and the corresponding arc voltage, U_{left} and U_{right} are measured. Then the seam deviation Δd is identified using Eq. (90). The robot adjusts the weaving center by Δd to track the weld seam again if the deviation exists.

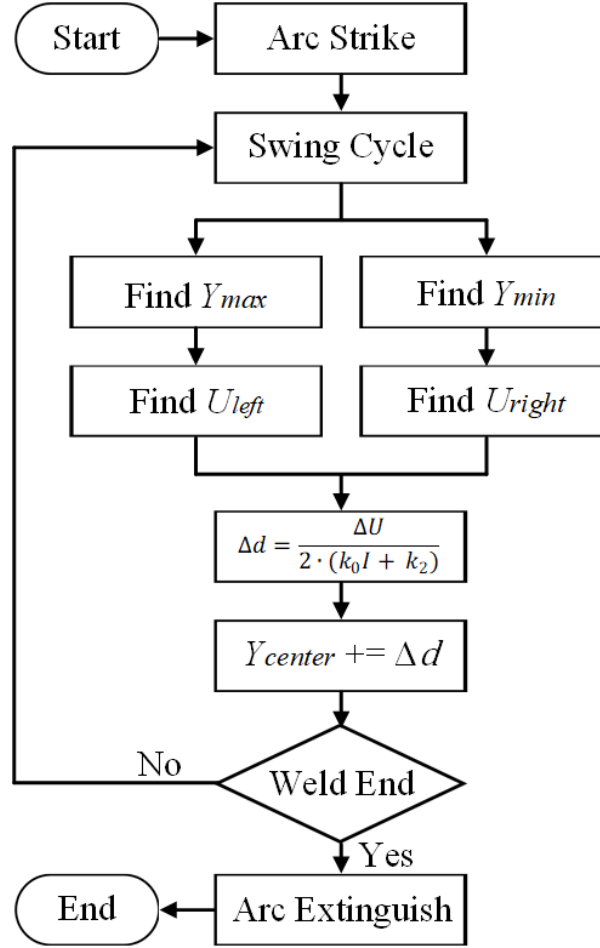


Figure 7.8 Working Flowchart of Proposed Automatic Seam Tracking Algorithm.

7.3 Welding Experiments and Analysis

Three experiments including manual welding, robotic welding and human-robot collaborative welding are conducted using the parameters in Table 7.1 to verify the effectiveness of the proposed human-robot collaborative welding system.

7.3.1 Manual Welding

In the manual welding, human observes the working scene and undertakes weaving welding. All the jobs in weaving welding including weaving welding torch, seam tracking and intelligent speed adjustment are done by human and the robot just copies the horizontal

trajectories of human with the vertical position and orientation fixed. Welding current is generated randomly and applied as the artificial disturbance to mimic the unpredicted disturbance appearing in practical welding. The weaving trajectory of manual welding, travel speed and welded workpiece are shown in Figure 7.9-11 respectively. The raw data of travel speed in Figure 7.10 has large fluctuation which increases the difficulty to recognize the intended travel speed. Therefore, the time-averaged data is presented for a clearer demonstration. The time averaged speed is computed as the mean travel speed in the interval before and after 1s:

$$\bar{v}_t = \frac{\sum_{i=-10}^{10} v_{t+0.1i}}{21} \quad (100)$$

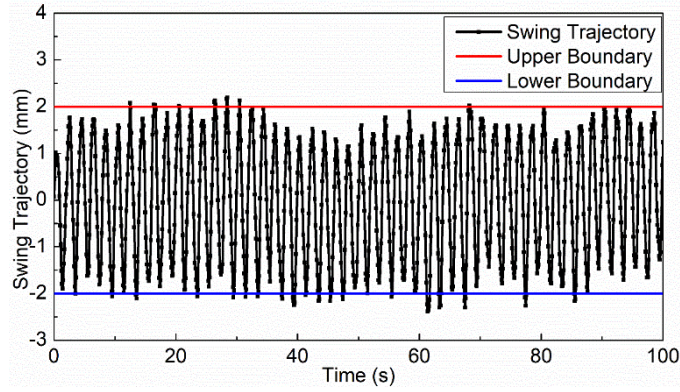


Figure 7.9 Swing Trajectory of Manual Welding.

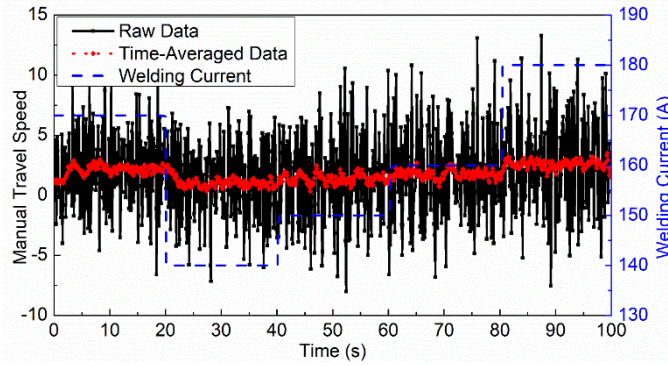


Figure 7.10 Manual Travel Speed Adjustment Facing Variable Welding Current.

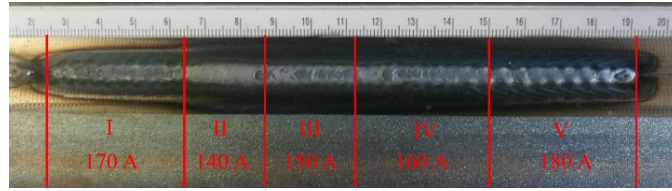


Figure 7.11 Welded Workpiece from Manual Welding.

7.3.2 Robotic Welding

Fully robotic swing welding is done using the same welding parameters without human involved. As shown in Figure 7.12, an artificial deviation degree θ between welding torch travel direction and weld seam is configured to mimic the practical seam deviation. The same random welding current is applied, and the travel speed of robot is fixed as 1.8 mm/s. The weaving trajectory with automatic seam tracking is shown in Figure 7.13 and the welded workpiece is shown in Figure 7.14.

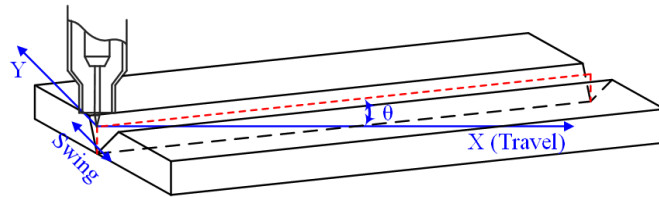


Figure 7.12 Welding Torch Travel Direction Deviates the Weld Seam with Degree θ .

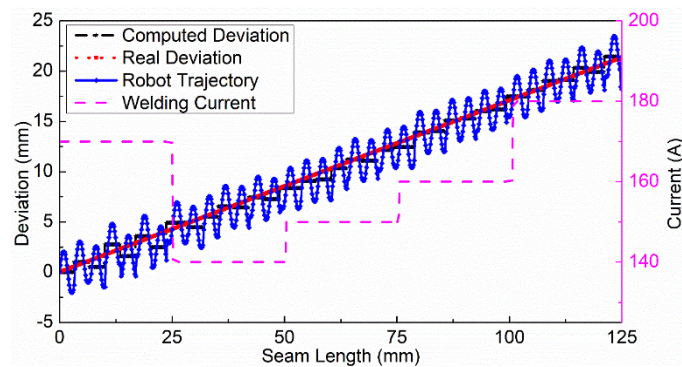


Figure 7.13 Welding Torch Weaving Trajectory with Automatic Seam Tracking.

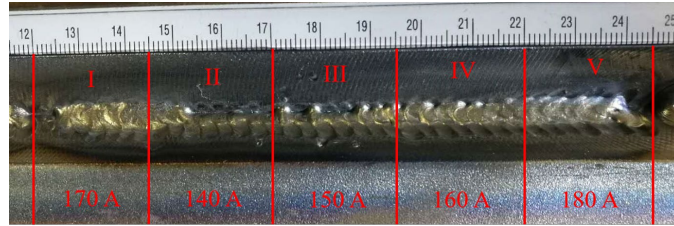


Figure 7.14 Welded Workpiece from Robotic Weaving Welding with Automatic Seam Tracking.

7.3.3 Human-robot Collaborative Welding

Using the same experiment configuration in robotic swing welding, human-robot collaborative welding is done. As talked before, robot carrying the welding torch weaves and tracks the weld seam automatically. Human observes the working scene and adjusts the travel speed. The robotic weaving trajectory with automatic seam tracking is shown in Figure 7.15. The travel speed applied from human is shown in Figure 7.16 and welded workpiece from human-robot collaborative welding is shown in Figure 7.17.

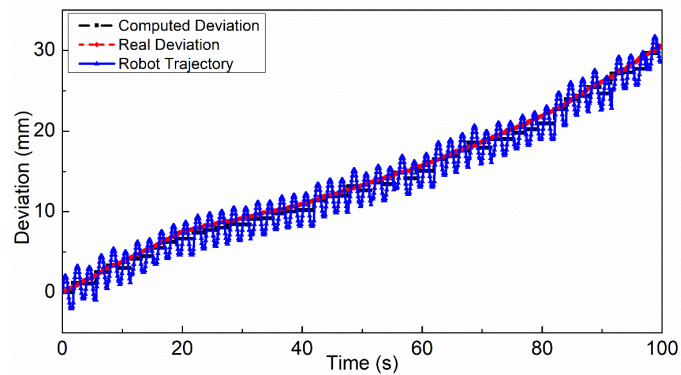


Figure 7.15 Robotic Weaving Trajectory in Human-robot Collaborative Welding.

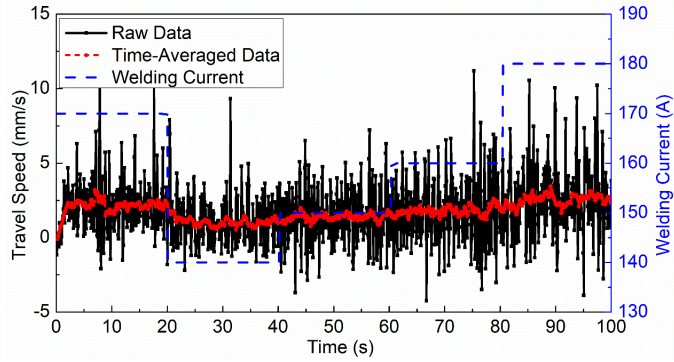


Figure 7.16 Travel Speed Applied from Human in Human-robot Collaborative Welding.

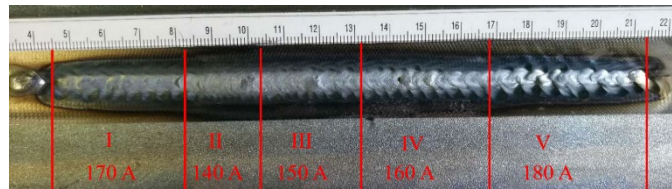


Figure 7.17 Welded Workpiece from Human-robot Collaborative Welding.

7.3.4 Result Analysis

In robotic welding experiment, the computed deviation can track the real deviation well such that the weaving welding can track the weld seam well in large deviation working environment (up to 20 mm deviation with 125 mm seam length) as shown in Figure 7.13. However, the robot cannot adjust the travel speed facing the working environment disturbance due to the lack of intelligence needed which results the inconsistent welding quality in Figure 7.14 where the manual welding does a better job. As shown in Figure 7.10, the human can adjust travel speed adaptively by observing the working scenes. The human increases the travel speed when welding current increases such that the heat input to workpiece is relative constant and the weld bead has consistent appearance. That is the advantages of human welders in practical welding. However, the human is not good at repeated and accurate movement. As shown in Figure 7.9, the

amplitude of manual swing trajectory is not constant. This results the width of weld bead is not consistent which should be avoided. The human-robot collaborative welding overcomes the disadvantages of human and robots. By using robotic swing with automatic seam tracking, the human-robot collaborative welding inherits all the advantages from robot welding and abandons the disadvantages from manual welding i.e., inaccurate swing and working fatigue to human. As shown in Figure 7.18, the weld bead width from human-robot collaborative welding is more consistent than manual welding. In the meantime, human-robot collaborative welding owes the needed intelligence from human facing working disturbance. The travel speed is adjusted by human such that the consistent weld bead is obtained as shown in Figure 7.17 and Figure 7.18. Therefore, the human-robot collaborative welding system combines the advantages of manual welding and robotic welding and the welded workpiece has the best performance than that done by human and robots individually.

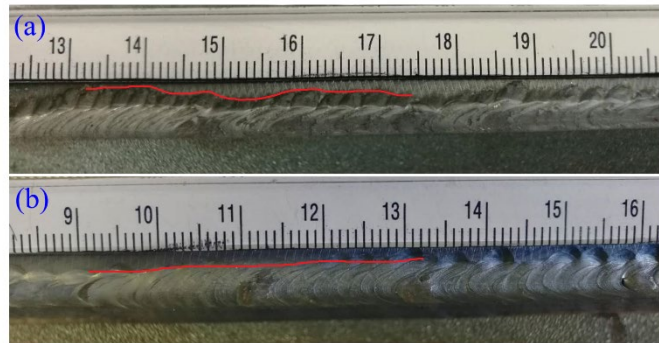


Figure 7.18 Solid Red Line Draws the Outline of Weld Bead (a) from Manual Welding (b) from Human-robot Collaborative Welding.

7.4 Summary

This chapter develops a digital twin framework for human-robot collaborative welding and applies this system in weaving gas tungsten arc welding as a case study. In

this framework, the advantages of human and robots i.e., the intelligence from human and the accurate movement from robots are combined which is verified by welding experiments. In addition, the labor burden for humans is minimized with the robot collaboration.

CHAPTER 8. CONCLUSIONS AND FUTURE WORKS

8.1 Conclusions

In order to accelerate the transition of current automatic welding manufacturing to intelligent welding manufacturing. A digital twin framework is developed in this work such that the welding manufacturing can be digitalized for further storage, analysis and sharing. In addition, the digital format makes it easy to integrate with other information technology advancements such as machine/deep learning, industrial big data, industrial Internet of Things etc. The main contributions of this work are in three aspects: 1) developing deep learning-empowered digital twin framework to offer the strong analyzing/reasoning ability; 2) integrating the natural HRI interface i.e., VR with digital twins to offer the strong operative ability from humans to physical manufacturing processes; and 3) investigating the roles robots can play in such a digital twin for human-robot interactive welding, from puppets, assistants, and collaborators. The detailed contributions and achievements are summarized following:

1. By integrating deep learning, the prediction of BSBW of weld joints reaches the state-of-the-art accuracy with MSE as 0.047 mm^2 . As such, the developed digital twin owns the better ability in charactering welding processes. Based on that, weld joint geometry can be control accurately to meet the quality requirement in various welding conditions. The visualized GUI offers the users intuitive and natural perception on the physical welding manufacturing in real time.

2. By integrating VR as the HRI interface, the human users own a better operative ability to the physical welding processes via the digital twin. The human users demonstrate welding operations remotely and the operations are captured by VR. The robots receive

the welding operations and conduct the welding onsite. The developed digital twin offers onsite scenes to the human users as the visual feedback in real time.

3. A data-driven machine learning method, FFT-PCA-SVM, is developed to identify the human welder skill level from their demonstrated operation sequences. This will help to novice welder training.

4. By recognizing human intention based on HMM, the robot can eliminate the unintended operations from humans and execute the intended welding operations. By doing that, the role of the robot changes to an assistant and it helps to improve the welding quality from novice welders.

5. By decomposing the welding task as several subtasks, its complexity is reduced. Humans and robots execute the portion where they are good at. As such, the humans and robots can collaborate with each other and their advantages are combined. This strategy has been applied in weaving GTAW as case study where its effectiveness has been verified.

8.2 Future Works

More works can be done in following several aspects:

1. More information charactering welding processes can be added in the developed digital twin such as temperature dynamic, fluid flow, microstructure evolution etc. with advanced sensing methods and computational intelligence. As such, welding manufacturing processes can be more transparent, and the process parameters can be optimized better.

2. More complex welding processes such as double-electrode gas metal arc welding (DE-GMAW) and laser-arc hybrid welding and other similar manufacturing processes

such as painting, spraying and additive manufacturing can be implemented in this digital twin framework. As such, the applicability can be increased further.

3. The imitation learning from human demonstration can be done to develop the decision-making policy for robots. As such, the robots can deal with the disturbance with human-level intelligence. Some human welders can be released from their labor burden and the welder shortage can be also relieved.

BIBLIOGRAPHY

- [1] H. S. Kang *et al.*, “Smart manufacturing: Past research, present findings, and future directions,” *Int. J. Precis. Eng. Manuf. - Green Technol.*, vol. 3, no. 1, pp. 111–128, Jan. 2016.
- [2] J. Lee, B. Bagheri, and H. A. Kao, “A Cyber-Physical Systems architecture for Industry 4.0-based manufacturing systems,” *Manuf. Lett.*, vol. 3, pp. 18–23, Jan. 2015.
- [3] Z. Bi, L. Da Xu, and C. Wang, “Internet of things for enterprise systems of modern manufacturing,” *IEEE Trans. Ind. Informatics*, vol. 10, no. 2, pp. 1537–1546, 2014.
- [4] A. Kusiak, “Smart manufacturing must embrace big data,” *Nature*, vol. 544, no. 7648, pp. 23–25, Apr. 2017.
- [5] J. Lee, H. Davari, J. Singh, and V. Pandhare, “Industrial Artificial Intelligence for industry 4.0-based manufacturing systems,” *Manuf. Lett.*, vol. 18, pp. 20–23, Oct. 2018.
- [6] G. Shao and M. Helu, “Framework for a digital twin in manufacturing: Scope and requirements,” *Manuf. Lett.*, vol. 24, pp. 105–107, 2020.
- [7] F. Tao, H. Zhang, A. Liu, and A. Y. C. Nee, “Digital twin in industry: state-of-the-art,” *IEEE Trans. Ind. Informatics*, vol. 15, no. 4, pp. 2405–2415, Apr. 2019.
- [8] J. N. Pires, A. Loureiro, T. Godinho, P. Ferreira, B. Fernando, and J. Morgado, “Welding robots,” *IEEE Robot. Autom. Mag.*, vol. 10, no. 2, pp. 45–55, Jul. 2003.
- [9] J. Dallos, “Combating the welder shortage,” *Fabtech Blog*, 2017. [Online]. Available: <https://www.fabtechexpo.com/blog/2017/12/04/combating-the-welder-shortage>.
- [10] O. Popović, R. Prokić-Cvetković, M. Burzić, U. Lukić, and B. Beljić, “Fume and gas emission during arc welding: Hazards and recommendation,” *Renew. Sustain. Energy Rev.*, vol. 37, pp. 509–516, 2014.
- [11] D. Guo, R. Y. Zhong, P. Lin, Z. Lyu, Y. Rong, and G. Q. Huang, “Digital twin-enabled Graduation Intelligent Manufacturing System for fixed-position assembly islands,” *Robot. Comput. Integr. Manuf.*, vol. 63, p. 101917, Jun. 2020.
- [12] R. Söderberg, K. Wärmefjord, J. S. Carlson, and L. Lindkvist, “Toward a Digital Twin for real-time geometry assurance in individualized production,” *CIRP Ann.*, vol. 66, no. 1, pp. 137–140, 2017.
- [13] X. Sun, J. Bao, J. Li, Y. Zhang, S. Liu, and B. Zhou, “A digital twin-driven approach for the assembly-commissioning of high precision products,” *Robot. Comput. Integr. Manuf.*, vol. 61, p. 101839, Feb. 2020.
- [14] A. Bilberg and A. A. Malik, “Digital twin driven human–robot collaborative

- assembly,” *CIRP Ann.*, vol. 68, no. 1, pp. 499–502, Jan. 2019.
- [15] K. Zhang *et al.*, “Digital twin-based opti-state control method for a synchronized production operation system,” *Robot. Comput. Integr. Manuf.*, vol. 63, p. 101892, Jun. 2020.
 - [16] A. Murphy *et al.*, “Representing financial data streams in digital simulations to support data flow design for a future Digital Twin,” *Robot. Comput. Integr. Manuf.*, vol. 61, p. 101853, Feb. 2020.
 - [17] G. L. Knapp *et al.*, “Building blocks for a digital twin of additive manufacturing,” *Acta Mater.*, vol. 135, pp. 390–399, Aug. 2017.
 - [18] T. DebRoy, W. Zhang, J. Turner, and S. S. Babu, “Building digital twins of 3D printing machines,” *Scr. Mater.*, vol. 135, pp. 119–124, Jul. 2017.
 - [19] T. Mukherjee and T. DebRoy, “A digital twin for rapid qualification of 3D printed metallic components,” *Appl. Mater. Today*, vol. 14, pp. 59–65, Mar. 2019.
 - [20] R. Cupek, M. Drewniak, A. Ziebinski, and M. Fojcik, “‘Digital twins’ for highly customized electronic devices – case study on a rework operation,” *IEEE Access*, vol. 7, pp. 164127–164143, 2019.
 - [21] H. Zhang, Q. Liu, X. Chen, D. Zhang, and J. Leng, “A Digital Twin-Based Approach for Designing and Multi-Objective Optimization of Hollow Glass Production Line,” *IEEE Access*, vol. 5, pp. 26901–26911, 2017.
 - [22] R. Dong, C. She, W. Hardjawana, Y. Li, and B. Vucetic, “Deep learning for hybrid 5G services in mobile edge computing systems: Learn from a digital twin,” *IEEE Trans. Wirel. Commun.*, vol. 18, no. 10, pp. 4692–4707, Jul. 2019.
 - [23] R. H. Guerra, R. Quiza, A. Villalonga, J. Arenas, and F. Castano, “Digital twin-based optimization for ultraprecision motion systems with backlash and friction,” *IEEE Access*, vol. 7, pp. 93462–93472, 2019.
 - [24] R. Zhao *et al.*, “Digital twin-driven cyber-physical system for autonomously controlling of micro punching system,” *IEEE Access*, vol. 7, pp. 9459–9469, 2019.
 - [25] Y. Fang, C. Peng, P. Lou, Z. Zhou, J. Hu, and J. Yan, “Digital-twin based job shop scheduling towards smart manufacturing,” *IEEE Trans. Ind. Informatics*, vol. 15, no. 12, pp. 6425–6435, Aug. 2019.
 - [26] C.-P. Wang, K. Erkorkmaz, J. McPhee, and S. Engin, “In-process digital twin estimation for high-performance machine tools with coupled multibody dynamics,” *CIRP Ann.*, May 2020.
 - [27] F. Tao, M. Zhang, Y. Liu, and A. Y. C. Nee, “Digital twin driven prognostics and health management for complex equipment,” *CIRP Ann.*, vol. 67, no. 1, pp. 169–172, Jan. 2018.
 - [28] W. Luo, T. Hu, Y. Ye, C. Zhang, and Y. Wei, “A hybrid predictive maintenance approach for CNC machine tool driven by Digital Twin,” *Robot. Comput. Integr.*

Manuf., vol. 65, p. 101974, Oct. 2020.

- [29] P. Zheng and A. S. Sivabalan, "A generic tri-model-based approach for product-level digital twin development in a smart manufacturing environment," *Robot. Comput. Integr. Manuf.*, vol. 64, p. 101958, Aug. 2020.
- [30] C. Liu, P. Jiang, and W. Jiang, "Web-based digital twin modeling and remote control of cyber-physical production systems," *Robot. Comput. Integr. Manuf.*, vol. 64, p. 101956, Aug. 2020.
- [31] P. Jain, J. Poon, J. P. Singh, C. Spanos, S. R. Sanders, and S. K. Panda, "A digital twin approach for fault diagnosis in distributed photovoltaic systems," *IEEE Trans. Power Electron.*, vol. 35, no. 1, pp. 940–956, Jan. 2020.
- [32] Y. Liu *et al.*, "A novel cloud-based framework for the elderly healthcare services using digital twin," *IEEE Access*, vol. 7, pp. 49088–49101, 2019.
- [33] R. S. Huang, L. M. Liu, and G. Song, "Infrared temperature measurement and interference analysis of magnesium alloys in hybrid laser-TIG welding process," *Mater. Sci. Eng. A*, vol. 447, no. 1–2, pp. 239–243, Feb. 2007.
- [34] D. Yang, G. Wang, and G. Zhang, "Thermal analysis for single-pass multi-layer GMAW based additive manufacturing using infrared thermography," *J. Mater. Process. Technol.*, vol. 244, pp. 215–224, Jun. 2017.
- [35] R. Kafieh, T. Lotfi, and R. Amirfattahi, "Automatic detection of defects on polyethylene pipe welding using thermal infrared imaging," *Infrared Phys. Technol.*, vol. 54, no. 4, pp. 317–325, Jul. 2011.
- [36] C. Doumanidis and Y. M. Kwak, "Multivariable adaptive control of the bead profile geometry in gas metal arc welding with thermal scanning," *Int. J. Press. Vessel. Pip.*, vol. 79, no. 4, pp. 251–262, May 2002.
- [37] N. M. Carlson and J. A. Johnson, "Ultrasonic sensing of weld pool penetration," *Weld. J.*, vol. 67, no. 11, pp. 239s–246s, 1988.
- [38] B. Mi and C. Ume, "Real-time weld penetration depth monitoring with laser ultrasonic sensing system," *J. Manuf. Sci. Eng.*, vol. 128, no. 1, pp. 280–286, Feb. 2006.
- [39] C. Fan, F. Lv, and S. Chen, "Visual sensing and penetration control in aluminum alloy pulsed GTA welding," *Int. J. Adv. Manuf. Technol.*, vol. 42, no. 1–2, pp. 126–137, May 2009.
- [40] W. J. Zhang, Y. K. Liu, X. Wang, and Y. M. Zhang, "Characterization of three-dimensional weld pool surface in gas tungsten arc welding," *Weld. J.*, vol. 91, no. 7, pp. 195s–203s, 2012.
- [41] A. J. R. Aendenrooier and G. Den Ouden, "Weld pool oscillation as a tool for penetration sensing during pulsed GTA welding," *Weld. J.*, vol. 77, no. 5, pp. 181s–187s, 1998.

- [42] Y. Shi, C. Li, L. Du, Y. Gu, and M. Zhu, "Frequency characteristics of weld pool oscillation in pulsed gas tungsten arc welding," *J. Manuf. Process.*, vol. 24, pp. 145–151, Oct. 2016.
- [43] U. Sreedhar, C. V. Krishnamurthy, K. Balasubramaniam, V. D. Raghupathy, and S. Ravisankar, "Automatic defect identification using thermal image analysis for online weld quality monitoring," *J. Mater. Process. Technol.*, vol. 212, no. 7, pp. 1557–1566, Jul. 2012.
- [44] N. Chandrasekhar, M. Vasudevan, A. K. Bhaduri, and T. Jayakumar, "Intelligent modeling for estimating weld bead width and depth of penetration from infra-red thermal images of the weld pool," *J. Intell. Manuf.*, vol. 26, no. 1, pp. 59–71, Apr. 2015.
- [45] S. Chokkalingham, N. Chandrasekhar, and M. Vasudevan, "Predicting the depth of penetration and weld bead width from the infra red thermal image of the weld pool using artificial neural network modeling," *J. Intell. Manuf.*, vol. 23, no. 5, pp. 1995–2001, Oct. 2012.
- [46] H. Chen, F. Lv, T. Lin, and S. Chen, "Closed-loop control of robotic arc welding system with full-penetration monitoring," *J. Intell. Robot. Syst.*, vol. 56, no. 5, pp. 565–578, 2009.
- [47] C. Wu and J. Gao, "Vision-based neuro-fuzzy control of weld penetration in gas tungsten arc welding of thin sheets," *Int. J. Model. Identif. Control*, vol. 1, no. 2, pp. 126–132, 2006.
- [48] Y. Liu, W. Zhang, and Y. Zhang, "Estimation of weld joint penetration under varying GTA pools," *Weld. J.*, vol. 92, no. 11, pp. 313s–321s, 2013.
- [49] K. Andersen and G. E. Cook, "Synchronous weld pool oscillation for monitoring and control," *IEEE Trans. Ind. Appl.*, vol. 33, no. 2, pp. 464–471, 1997.
- [50] K. He, X. Zhang, S. Ren, and J. Sun, "Deep residual learning for image recognition," in *Proc. IEEE-CVPR*, 2016, pp. 770–778.
- [51] V. Sze, Y. H. Chen, T. J. Yang, and J. S. Emer, "Efficient processing of deep neural networks: A tutorial and survey," *Proc. IEEE*, vol. 105, no. 12, pp. 2295–2329, Dec. 2017.
- [52] W. Liu, Z. Wang, X. Liu, N. Zeng, Y. Liu, and F. E. Alsaadi, "A survey of deep neural network architectures and their applications," *Neurocomputing*, vol. 234, pp. 11–26, Apr. 2017.
- [53] W. Chan, N. Jaitly, Q. Le, and O. Vinyals, "Listen, attend and spell: A neural network for large vocabulary conversational speech recognition," in *Proc. IEEE-ICASSP*, 2016, pp. 4960–4964.
- [54] J. Hirschberg and C. D. Manning, "Advances in natural language processing," *Science (80-.)*, vol. 349, no. 6245, pp. 261–266, Jul. 2015.
- [55] K. Fukushima, "Neocognitron: A self-organizing neural network model for a

- mechanism of pattern recognition unaffected by shift in position,” *Biol. Cybern.*, vol. 36, no. 4, pp. 193–202, Apr. 1980.
- [56] Y. LeCun, L. Bottou, Y. Bengio, and P. Haffner, “Gradient-based learning applied to document recognition,” *Proc. IEEE*, vol. 86, no. 11, pp. 2278–2324, 1998.
 - [57] A. Krizhevsky, I. Sutskever, and G. E. Hinton, “ImageNet classification with deep convolutional neural networks,” *Adv. Neural Inf. Process. Syst.*, pp. 1097–1105, 2012.
 - [58] K. Simonyan and A. Zisserman, “Very deep convolutional networks for large-scale image recognition,” in *Proc. ICLR*, 2015.
 - [59] C. Szegedy *et al.*, “Going deeper with convolutions,” in *Proc. IEEE-CVPR*, 2015, pp. 1–9.
 - [60] I. J. Goodfellow *et al.*, “Generative Adversarial Nets,” in *Proc. NIPS*, p. 2014.
 - [61] J. Duchi, E. Hazan, and Y. Singer, “Adaptive subgradient methods for online learning and stochastic optimization,” *J. Mach. Learn. Res.*, vol. 12, p. 2121–2159, 2011.
 - [62] M. D. Zeiler, “ADADELTA: An adaptive learning rate method,” *arXiv Prepr. arXiv1212.5701*, Dec. 2012.
 - [63] D. P. Kingma and J. Ba, “Adam: A method for stochastic optimization,” in *Proc. ICLR*, 2015.
 - [64] D. E. Rumelhart, G. E. Hinton, and R. J. Williams, “Learning representations by back-propagating errors,” *Nature*, vol. 323, no. 6088, pp. 533–536, 1986.
 - [65] B. Kosko, “Bidirectional Associative Memories,” *IEEE Trans. Syst. Man Cybern.*, vol. 18, no. 1, pp. 49–60, 1988.
 - [66] H. Jaeger and H. Haas, “Harnessing Nonlinearity: Predicting Chaotic Systems and Saving Energy in Wireless Communication,” *Science (80-.)*, vol. 304, no. 5667, pp. 78–80, Apr. 2004.
 - [67] F. A. Gers, “Learning to forget: continual prediction with LSTM,” in *Proc. ICANN*, 1999, pp. 850–855.
 - [68] I. Goodfellow, Y. Bengio, and A. Courville, *Deep learning*. MIT press, 2016.
 - [69] J. Sprovieri, “New Technology for Robotic Welding,” *Assembly*, 2016. [Online]. Available: <https://www.assemblymag.com/articles/93555-new-technology-for-robotic-welding>.
 - [70] G. Bekey and J. Yuh, “The status of robotics,” *IEEE Robot. Autom. Mag.*, vol. 14, no. 4, pp. 76–81, 2007.
 - [71] Z. Pan, J. Polden, N. Larkin, S. Van Duin, and J. Norrish, “Recent progress on programming methods for industrial robots,” *Robotics and Computer-Integrated Manufacturing*. 2012.

- [72] M. S. Erden and B. Marić, “Assisting manual welding with robot,” *Robot. Comput. Integr. Manuf.*, vol. 27, no. 4, pp. 818–828, Aug. 2011.
- [73] A. Hariri, A. M. Leman, M. Z. M. Yusof, N. A. Paiman, and N. M. Noor, “Preliminary Measurement of Welding Fumes in Automotive Plants,” *Int. J. Environ. Sci. Dev.*, 2012.
- [74] H. C. Li, H. M. Gao, and L. Wu, “Teleteaching approach for sensor-based arc welding telerobotic system,” *Ind. Rob.*, vol. 34, no. 5, pp. 423–429, 2007.
- [75] Z. Liang, H. Gao, L. Nie, and L. Wu, “3D reconstruction for telerobotic welding,” in *Proceedings of the 2007 IEEE International Conference on Mechatronics and Automation, ICMA 2007*, 2007, pp. 475–479.
- [76] M. S. Erden and A. Billard, “Robotic Assistance by Impedance Compensation for Hand Movements while Manual Welding,” *IEEE Trans. Cybern.*, 2016.
- [77] T. Zhang *et al.*, “Deep Imitation Learning for Complex Manipulation Tasks from Virtual Reality Teleoperation,” in *Proc. IEEE-ICRA*, 2018, pp. 5628–5635.
- [78] B. D. Argall, S. Chernova, M. Veloso, and B. Browning, “A survey of robot learning from demonstration,” *Rob. Auton. Syst.*, vol. 57, no. 5, pp. 469–483, May 2009.
- [79] H. Zhang and S. K. Agrawal, “An active neck brace controlled by a joystick to assist head motion,” *IEEE Robot. Autom. Lett.*, vol. 3, no. 1, pp. 37–43, Jan. 2018.
- [80] Z. Ma and P. Ben-Tzvi, “RML glove-an exoskeleton glove mechanism with haptics feedback,” *IEEE/ASME Trans. Mechatronics*, vol. 20, no. 2, pp. 641–652, Apr. 2015.
- [81] G. Du, P. Zhang, and X. Liu, “Markerless human-manipulator interface using leap motion with interval Kalman filter and improved particle filter,” *IEEE Trans. Ind. Informatics*, vol. 12, no. 2, pp. 694–704, Apr. 2016.
- [82] K. Zinchenko, C. Y. Wu, and K. T. Song, “A study on speech recognition control for a surgical robot,” *IEEE Trans. Ind. Informatics*, vol. 13, no. 2, pp. 607–615, Apr. 2017.
- [83] C. Yang, X. Wang, Z. Li, Y. Li, and C. Y. Su, “Teleoperation Control Based on Combination of Wave Variable and Neural Networks,” *IEEE Trans. Syst. Man, Cybern. Syst.*, vol. 47, no. 8, pp. 2125–2136, Aug. 2017.
- [84] H. Hedayati, M. Walker, and D. Szafir, “Improving Collocated Robot Teleoperation with Augmented Reality,” in *ACM/IEEE International Conference on Human-Robot Interaction*, 2018, pp. 78–86.
- [85] L. P. Berg and J. M. Vance, “Industry use of virtual reality in product design and manufacturing: a survey,” *Virtual Real.*, vol. 21, no. 1, pp. 1–17, Mar. 2017.
- [86] L. P. Berg and J. M. Vance, “An Industry Case Study: Investigating Early Design Decision Making in Virtual Reality,” *J. Comput. Inf. Sci. Eng.*, vol. 17, no. 1, Mar.

2017.

- [87] C. J. Turner, W. Hutabarat, J. Oyekan, and A. Tiwari, "Discrete Event Simulation and Virtual Reality Use in Industry: New Opportunities and Future Trends," *IEEE Trans. Human-Machine Syst.*, vol. 46, no. 6, pp. 882–894, Dec. 2016.
- [88] R. B. Hasan, F. B. A. Aziz, H. A. A. Mutaleb, and Z. Umar, "Virtual reality as an industrial training tool: A review," *J. Adv. Rev. Sci. Res.*, vol. 29, no. 1, pp. 20–26, 2017.
- [89] C. Noon, R. Zhang, E. Winer, J. Oliver, B. Gilmore, and J. Duncan, "A system for rapid creation and assessment of conceptual large vehicle designs using immersive virtual reality," *Comput. Ind.*, vol. 63, no. 5, pp. 500–512, Jun. 2012.
- [90] G. Lawson, P. Herriotts, L. Malcolm, K. Gabrecht, and S. Hermawati, "The use of virtual reality and physical tools in the development and validation of ease of entry and exit in passenger vehicles," *Appl. Ergon.*, 2015.
- [91] A. Seth, J. M. Vance, and J. H. Oliver, "Virtual reality for assembly methods prototyping: A review," *Virtual Real.*, 2011.
- [92] A. Chellali, F. Jourdan, and C. Dumas, "VR4D: An immersive and collaborative experience to improve the interior design process," in *5th Joint Virtual Reality Conference of EGVE and EuroVR, JVRC*, 2013.
- [93] J. Whyte, N. Bouchlaghem, A. Thorpe, and R. McCaffer, "From CAD to virtual reality: Modelling approaches, data exchange and interactive 3D building design tools," *Autom. Constr.*, 2000.
- [94] R. T. Stone, K. P. Watts, and P. Zhong, "Virtual reality integrated welder training," *Weld. J.*, vol. 90, no. 7, pp. 136s–141s, Jul. 2011.
- [95] V. G. Bharath and R. Patil, "Solid Modelling Interaction with Sensors in Virtual Environment for the Application of Virtual Reality Welding," in *International Conference on Current Trends in Computer, Electrical, Electronics and Communication, CTCEEC 2017*, 2018, pp. 645–647.
- [96] G. A. Lee *et al.*, "Virtual reality content-based training for spray painting tasks in the shipbuilding industry," *ETRI J.*, 2010.
- [97] H. Zhang, "Head-mounted display-based intuitive virtual reality training system for the mining industry," *Int. J. Min. Sci. Technol.*, 2017.
- [98] E. Matsas and G. C. Vosniakos, "Design of a virtual reality training system for human–robot collaboration in manufacturing tasks," *Int. J. Interact. Des. Manuf.*, vol. 11, no. 2, pp. 139–153, May 2017.
- [99] D. Whitney, E. Rosen, D. Ullman, E. Phillips, and S. Tellex, "ROS Reality: A Virtual Reality Framework Using Consumer-Grade Hardware for ROS-Enabled Robots," in *Proc. IEEE-IROS*, 2018, pp. 5018–5025.
- [100] N. Lv, Y. Xu, S. Li, X. Yu, and S. Chen, "Automated control of welding

- penetration based on audio sensing technology,” *J. Mater. Process. Technol.*, vol. 250, pp. 81–98, Dec. 2017.
- [101] Z. Chen, J. Chen, and Z. Feng, “Welding penetration prediction with passive vision system,” *J. Manuf. Process.*, vol. 36, pp. 224–230, Dec. 2018.
 - [102] Y. Cui, Y. Shi, and X. Hong, “Analysis of the frequency features of arc voltage and its application to the recognition of welding penetration in K-TIG welding,” *J. Manuf. Process.*, vol. 46, pp. 225–233, Oct. 2019.
 - [103] Z. Zhang and S. Chen, “Real-time seam penetration identification in arc welding based on fusion of sound, voltage and spectrum signals,” *J. Intell. Manuf.*, vol. 28, no. 1, pp. 207–218, Jan. 2017.
 - [104] W. Zhang, Y. Liu, X. Wang, and Y. Zhang, “Characterization of three-dimensional weld pool surface in GTAW,” *Weld. J.*, vol. 91, no. 7, pp. 195s–203s, 2012.
 - [105] X. W. Wang and R. R. Li, “Intelligent modelling of back-side weld bead geometry using weld pool surface characteristic parameters,” *J. Intell. Manuf.*, vol. 25, no. 6, pp. 1301–1313, Nov. 2014.
 - [106] R. Liang, R. Yu, Y. Luo, and Y. M. Zhang, “Machine learning of weld joint penetration from weld pool surface using support vector regression,” *J. Manuf. Process.*, vol. 41, pp. 23–28, May 2019.
 - [107] Q. Wang, W. Jiao, P. Wang, and Y. M. Zhang, “A tutorial on deep learning-based data analytics in manufacturing through a welding case study,” *J. Manuf. Process.*, May 2020.
 - [108] S. M. M. Rahman, “Cyber-physical-social system between a humanoid robot and a virtual human through a shared platform for adaptive agent ecology,” *IEEE/CAA J. Autom. Sin.*, vol. 5, no. 1, pp. 190–203, Jan. 2018.
 - [109] J. I. Lipton, A. J. Fay, and D. Rus, “Baxter’s homunculus: Virtual reality spaces for teleoperation in manufacturing,” *IEEE Robot. Autom. Lett.*, vol. 3, no. 1, pp. 179–186, Jan. 2018.
 - [110] M. Borges, A. Symington, B. Coltin, T. Smith, and R. Ventura, “HTC Vive: Analysis and Accuracy Improvement,” in *Proc. IEEE-ICRA*, 2018, pp. 2610–2615.
 - [111] L. Shi, C. Tong, T. Lan, and X. Shi, “Statistical process monitoring based on ensemble structure analysis,” *IEEE/CAA J. Autom. Sin.*, Feb. 2018.
 - [112] P. Zhang, S. Shu, and M. Zhou, “An online fault detection model and strategies based on SVM-grid in clouds,” *IEEE/CAA J. Autom. Sin.*, vol. 5, no. 2, pp. 445–456, Mar. 2018.
 - [113] M. S. Erden and T. Tomiyama, “Identifying welding skills for training and assistance with robot,” *Sci. Technol. Weld. Join.*, vol. 14, no. 6, pp. 523–532, 2009.
 - [114] Y. K. Liu, Y. M. Zhang, and L. Kvidahl, “Skilled human welder intelligence modeling and control: Part I - Modeling,” *Weld. J.*, vol. 93, no. 2, pp. 46–52, 2014.

- [115] Y. K. Liu, Y. M. Zhang, and L. Kvidahl, "Skilled human welder intelligence modeling and control: Part II - analysis and control applications," *Weld. J.*, vol. 93, no. 5, pp. 162–170, 2014.
- [116] A. J. Smola and B. Schölkopf, "A tutorial on support vector regression," *Statistics and Computing*, vol. 14, no. 3, pp. 199–222, Aug-2004.
- [117] T. P. Minka, "Automatic choice of dimensionality for PCA," in *Proc. NIPS*, 2000, pp. 577–583.
- [118] F. Pedregosa *et al.*, "Scikit-learn: Machine learning in Python," *J. Mach. Learn. Res.*, vol. 12, no. 85, pp. 2825–2830, 2011.
- [119] A. Kleinsmith and N. Bianchi-Berthouze, "Affective body expression perception and recognition: A survey," *IEEE Trans. Affect. Comput.*, vol. 4, no. 1, pp. 15–33, 2013.
- [120] J. Huang, W. Huo, W. Xu, S. Mohammed, and Y. Amirat, "Control of Upper-Limb Power-Assist Exoskeleton Using a Human-Robot Interface Based on Motion Intention Recognition," *IEEE Trans. Autom. Sci. Eng.*, vol. 12, no. 4, pp. 1257–1270, Oct. 2015.
- [121] T. Mei, X. S. Hua, H. Q. Zhou, and S. Li, "Modeling and mining of users' capture intention for home videos," *IEEE Trans. Multimed.*, vol. 9, no. 1, pp. 66–76, Jan. 2007.
- [122] Y. Li and S. S. Ge, "Human-robot collaboration based on motion intention estimation," *IEEE/ASME Trans. Mechatronics*, vol. 19, no. 3, pp. 1007–1014, 2014.
- [123] K. Khokar, R. Alqasemi, S. Sarkar, K. Reed, and R. Dubey, "A novel telerobotic method for human-in-The-loop assisted grasping based on intention recognition," in *Proceedings - IEEE International Conference on Robotics and Automation*, 2014, pp. 4762–4769.
- [124] D. Aarno and D. Kragic, "Layered HMM for motion intention recognition," in *IEEE International Conference on Intelligent Robots and Systems*, 2006, pp. 5130–5135.
- [125] N. Stefanov, A. Peer, and M. Buss, "Online intention recognition for computer-assisted teleoperation," in *Proceedings - IEEE International Conference on Robotics and Automation*, 2010, pp. 5334–5339.
- [126] L. R. Rabiner, "A Tutorial on Hidden Markov Models and Selected Applications in Speech Recognition," *Proc. IEEE*, vol. 77, no. 2, pp. 257–286, 1989.
- [127] J. Ogbemhe and K. Mpofu, "Towards achieving a fully intelligent robotic arc welding: A review," *Ind. Rob.*, 2015.

VITA

QIYUE WANG

Education:

B.E. in Welding Engineering at Harbin Institute of Technology, Harbin, China, 08/2012 – 07/2016

Publications in pursuing Ph.D.:

1. **Qiyue Wang**, Wenhua Jiao, YuMing Zhang*, “Deep learning-empowered digital twin for visualized weld joint growth monitoring and penetration control” *J. of Manuf. Syst.* vol. 57, pp, 429-439, 2020.
2. **Qiyue Wang**, Qiyue Wang, Wenhua Jiao, Peng Wang*, YuMing Zhang. “A tutorial on deep learning-based data analytics in manufacturing through a welding case study.” *J. Manuf. Process.*
3. **Qiyue Wang**, Wenhua Jiao, Peng Wang, YuMing Zhang*. “Digital twin for human-robot interactive welding and welder behavior analysis.” *IEEE/CAA J. Autom. Sin.* Vol. 8, No. 2, pp. 334-343, 2021.
4. **Qiyue Wang**, Wenhua Jiao, Rui Yu, Michael T. Johnson, and YuMing Zhang*. “Modeling of human welders’ operations in virtual reality human-robot interaction.” *IEEE Robot. Autom. Lett.* vol. 4, no. 3, pp. 2958-2964, 2019.
5. **Qiyue Wang**, Wenhua Jiao, Rui Yu, Michael T. Johnson, and YuMing Zhang*. “Virtual reality robot-assisted welding based on human intention recognition.” *IEEE Trans. Autom. Sci. Eng.* vol. 17, no. 2, pp. 799-808, 2020.
6. **Qiyue Wang**, Yongchao Cheng, Wenhua Jiao, Michael T. Johnson, and YuMing Zhang*. “Virtual reality human-robot collaborative welding: A case study of weaving gas tungsten arc welding.” *J. Manuf. Process.* vol. 48, pp. 210-217, 2019.
7. Wenhua Jiao, **Qiyue Wang**, Yongchao Cheng, and YuMing Zhang*, “End-to-end prediction of weld penetration: A deep learning and transfer learning-based method,” *J. Manuf. Process.* 2020.
8. Yongchao Cheng, **Qiyue Wang**, Wenhua. Jiao, Rui Yu, Shujun Chen, YuMing Zhang, Jun Xiao*, Detecting dynamic development of weld pool using machine learning from innovative composite images for adaptive welding, *J. Manuf. Process.* 2020.

9. Zhimin Liang, Hexi Chang, **Qiyue Wang**, Dianlong Wang, and YuMing Zhang*, “3D reconstruction of weld pool surface in pulsed GMAW by passive biprism stereo vision,” *IEEE Robot. Autom. Lett.* vol. 4, no. 3, pp. 3091-3097, 2019.
10. Wenhua Jiao, **Qiyue Wang**, Yongchao Cheng, Rui Yu, YuMing Zhang*, “Prediction of weld penetration from dynamic weld pool-arc Images” , *Weld J.* (Accepted).
11. Chao Li, **Qiyue Wang**, Wenhua Jiao, Michael T. Johnson, YuMing. Zhang*, “Deep learning-based detection of penetration from pool reflection images” , *Weld J.* (Accepted).
12. YuMing Zhang*, **Qiyue Wang**, Yukang Liu, “ Adaptive intelligent welding manufacturing – classical sensing/modeling/control and modern machine learning and human-robot collaborative approaches” , *Weld J.* (Accepted).